Finanziato dall'Unione europea NextGenerationEU
Ministero dell'Università e della Ricerca
Italiadomani PIANO NAZIONALE DI RIPRESA E RESILIENZA
Consiglio Nazionale delle Ricerche

UNIVERSITY OF NAPLES FEDERICO II

DOTTORATO DI RICERCA IN BIOLOGIA

XXXVIII Cycle - PNRR

NANOBIOMATERIALS TARGETING THE TUMOR MICROENVIRONMENT FOR ENHANCED GENE THERAPY

PhD Coordinator
Prof. Sergio Esposito

Tutors
Prof. Angelo Fontana
Dr. Maria Grazia Raucci

PhD candidate
Francesca Liguori

2024-2025

RNA &GENETHERAPY NATIONAL RESEARCH CENTER
CNR iPCB Istituto per i Polimeri, Compositi e Biomateriali

Table of contents

List of Figures

List of Tables

Abbreviations

2D- Two-dimensional

3D – Three-dimensional

AKT – Protein kinase B

AuNPs – Gold nanoparticles

BCA – Bicinchoninic acid

BSA – Bovine serum albumin

bPEI – Branched polyethylenimine

CerS – Ceramide synthases

CNTs – Carbon nanotubes

COPI – Coat Protein Complex I

DCF – Dichlorofluorescein

DCFH-DA – 2′,7′-Dichlorodihydrofluorescein diacetate

DLS – Dynamic Light Scattering

DMEM – Dulbecco's Modified Eagle's Medium

DNA-PK – DNA-dependent protein kinase

DU145 – Prostate cancer cell line

EDC – 1-Ethyl-3-(3-dimethylaminopropyl)carbodiimide

EVs – Extracellular vesicles

F-actin – Filamentous actin

FITC – Fluorescein isothiocyanate

FTIR-ATR – Fourier-transform infrared spectroscopy with attenuated total reflectance

GlcCer – Glucosylceramide

GOLPH3 – Golgi phosphoprotein 3

GMx33 – Golgi membrane protein 33

GPP34 – Golgi phosphoprotein 34

GSLs – Glycosphingolipids

H&E – Hematoxylin and eosin

HPRT1 – Hypoxanthine-guanine phosphoribosyltransferase 1

HUVECs – Human umbilical vein endothelial cells

ILs – Ionic liquids

LacCer – Lactosylceramide

LDH – Lactate dehydrogenase

LGIP – PLGA–PEI hybrid nanoparticles

lPEI – Linear polyethylenimine

MIDAS – Metal ion-dependent adhesion site

miRNA – MicroRNA

MSNs – Mesoporous silica nanoparticles

mTOR – Mechanistic target of rapamycin

mTORC1 – Mechanistic target of rapamycin complex 1

mTORC2 – Mechanistic target of rapamycin complex 2

MYO18A – Myosin XVIIIA

NDs – Nanodiamonds

NHS – N-Hydroxysuccinimide

NMR – Nuclear magnetic resonance

N/P ratio – Nitrogen/phosphate ratio

NSCLC – Non-small cell lung cancer

PCL – Polycaprolactone

PEI – Polyethylenimine

PEG – Polyethylene glycol

PI – Propidium iodide

PI3K – Phosphatidylinositol 3-kinase

PI4P – Phosphatidylinositol 4-phosphate

PLA – Polylactic acid

PLGA – Poly(lactic-co-glycolic acid)

PGA – Polyglycolic acid

PNT2 – Prostatic epithelial cell line

qPCR – Quantitative polymerase chain reaction

RISC – RNA-induced silencing complex

RNAi – RNA interference

ROS – Reactive oxygen species

RPMI – Roswell Park Memorial Institute medium

siRNA – Small interfering RNA

SPIONs – Superparamagnetic iron oxide nanoparticles

TEM – Transmission Electron Microscopy

VEGF – Vascular endothelial growth factor

WHO – World Health Organization

Abstract

Golgi phosphoprotein 3 (GOLPH3), also known as GPP34, GMx33, or MIDAS, is a Golgi apparatus-associated protein involved in regulating fundamental cellular processes, including tumor cell proliferation, migration, and metabolism. Numerous studies have highlighted its overexpression in various solid tumors, including lung, breast, prostate, and colon cancer, identifying GOLPH3 as a promising therapeutic target. In this context, suppression of GOLPH3 by RNA interference (RNAi) represents an effective therapeutic strategy. In this context, the development of efficient, biocompatible, and tunable delivery systems is therefore essential to fully exploit the therapeutic potential of RNAi.

To this end, this thesis focused on the development and characterization of polymeric nanosystems for the targeted delivery of anti-GOLPH3 siRNA in prostate cancer. Two nanoparticle platforms were investigated. The first consists of poly(lactic-co-glycolic acid) (PLGA) nanoparticles functionalized with imidazolium-based ionic liquids (ILs), selected for their tunable amphiphilicity, cationic character, and ability to modulate nanoparticle–cell interactions. Following a comprehensive screening, formulations containing 1-hexadecyl-3-methylimidazolium chloride (C16ImCl) and 1-decylecyl-3-methylimidazolium chloride (C10ImCl) were selected, obtaining PLGA-C16 and PLGA-C10 nanoparticles. The second platform developed in this work consisted of hybrid nanoparticles obtained by conjugating PLGA with linear polyethylenimine (PEI), termed LGIP, formulated at two different polymer/siRNA ratios (LGIP-1 and LGIP-10), in order to evaluate the influence of the PEI content on the system properties and biological efficacy. All nanosystems were thoroughly characterized in terms of size, morphology, surface charge, colloidal stability, siRNA loading and release profiles.

In vitro studies demonstrated that all formulations exhibited a good biocompatibility profile in both DU145 prostate cancer cells, and in healthy PNT2 prostatic epithelial cells. Cellular uptake and intracellular trafficking analyses revealed that nanoparticle surface chemistry strongly influences internalization kinetics and endocytic pathways. In particular, PLGA-C16 nanoparticles exhibited rapid and efficient uptake, predominantly via clathrin-mediated endocytosis at low concentrations, while PLGA-C10 nanoparticles showed slower internalization and a greater reliance on micropinocytosis at higher doses. LGIP nanoparticles displayed delayed but sustained cellular uptake involving multiple endocytic routes. Functional wound healing assays confirmed that effective silencing of GOLPH3, mediated primarily by PLGA-C16 nanoparticles and to a lesser extent by LGIP-1, results in significant inhibition of tumor cell migration. Finally, in three-dimensional (3D) models of tumor spheroids highlighted, the differential effect of PLGA-C16 and PLGA-C10 suggested that the alkyl chain length of ionic liquids influences spheroid morphogenesis and

interaction with nanoparticles, underscoring the importance of nanosystem composition in more physiologically relevant contexts. Overall, this work demonstrates that rational modulation of nanoparticle surface chemistry through ionic liquid functionalization or polymer conjugation critically determines cellular uptake mechanisms, intracellular fate, and gene silencing efficacy. These findings support the potential of PLGA-ILs and LGIP nanoparticles as versatile and effective non-viral platforms for siRNA delivery and provide valuable design principles for the development of advanced RNAi-based therapeutic strategies targeting oncogenic pathways in cancer.

1. Introduction

1.1 Cancer: A complex and multifactorial disease

Cancer is a major cause of morbidity and mortality globally and poses one of the most significant challenges for modern healthcare systems. According to data from the World Health Organization (WHO), approximately 10 million deaths attributable to cancer were recorded in cases of cancer diagnosed in the same year worldwide [1].Epidemiological projections indicate a further and worrying increase in a global incidence, with an estimated 35.5 million new cases per year by 2050, equal to an increase of over 70% compared to current data [2]. This increase is attributable to several factors, including population aging, changes in lifestyle, exposure to environmental factors and the increased prevalence of oncogenic risk factors [3]. From biological point of view, cancer is a complex disease characterized by uncontrolled cell growth and abnormal proliferation of cells that escape the normal regulatory mechanism of the cell cycle, apoptosis and DNA repair [4].

Under physiological conditions, these mechanisms ensure the maintenance of tissue homeostasis and prevent the accumulation of genetically damaged cells. Their alteration instead leads to a disordered proliferation, which culminates in the formation of tumors with the ability to invade surrounding tissues and spread to distant organs through the process of metastasis, significantly complicating treatment and worsening the prognosis of patients. The development and progression of cancer are driven by the accumulation of genetic and molecular alterations that compromise the balance between proliferative and antiproliferative signals [5] .In particular, activating mutations in oncogenes, such as RAS, MYC and PI3K, determine the constitutive activation of signaling pathways involved in growth, survival and cell division, allowing tumor cells to proliferate even in the absence of extracellular stimuli. In parallel, inactivating mutations in tumor suppressor genes, such as TP53, RB1 and PTEN, lead to the loss of key mechanisms controlling the cell cycle, apoptosis induction and genomic surveillance, allowing the survival and clonal expansion of damaged cells [6]. A further fundamental contribution to tumorigenesis comes from defects in DNA repair systems. Mutations in key genes involved in these processes, including BRCA1, BRCA2, MSH2 and MLH1, determine an increase in genomic instability, favoring the progressive accumulation of further mutations and chromosomal rearrangements that accelerate tumor evolution. These alterations can be hereditary, transmitted at the germinal level, or acquired during life following exposure to environmental and behavioral factors, such as ionizing radiation, carcinogenic chemicals, cigarette smoking, oncogenic viral infections and oxidative stress [7].The combination of these genetic and molecular events determined the acquisition of a neoplastic phenotype characterized by autonomous proliferation, resistance to cell death, uncontrolled angiogenesis by the high intra-and iter tumor heterogeneity,

which translates into highly variable therapeutic response and represents one of the main obstacles to the effectiveness of conventional oncological therapies [1].Consequently, the need to the develop personalized therapeutic approaches, able to take into account the molecular specificities of each tumor, emerges. For these reasons, contemporary oncology research is increasingly oriented towards the identification and understanding of the molecular mechanism that regulate tumor growth and progression, with the aim of developing targeted and precision therapeutic strategies [8].In this context, the identification of new molecular targets and the development of innovative approaches, such as gene silencing by RNA interference and the use of advances gene delivery systems, represent promising prospects for improving therapeutic efficacy and reducing systematic toxicity associates with antitumor treatments [9].

1.2 GOLPH3: An emerging oncogene

Large-scale genomic analyses of multiple human tumors have identified GOLPH3, along with its interaction partners MYO18A and Phosphatidylinositol Transfer Protein, Cytoplasmic1 (PITPNC1), as key components involved in oncogenic transformation. In particular, GOLPH3 has emerged as one of the most frequently amplified genes in solid tumors. Genome mapping studies have identified a minimal amplification region on chromosome 5p13 containing four genes, of which only GOLPH3 showed a clear correlation between copy number and expression levels. Furthermore, its silencing caused a marked reversion of the transformed phenotype in cultured cells, confirming its direct oncogenic function [10].GOLPH3 amplification has been reported in several cancer types, including lung (56%), prostate (37%), breast (32%), pancreatic (33%), colon (24%), and ovarian (37%) cancer, underscoring its broad trans tumor relevance. In addition to promoting tumor growth, GOLPH3 also contributes to cell migration and invasion, two critical processes involved in the formation of metastases [11].The functional GOLPH3–MYO18A–PITPNC1 complex orchestrates multiple aspects of neoplastic behavior. MYO18A is a key determinant of tumor cell motility and invasion, particularly in breast and prostate cancer. PITPNC1, a Golgi-localized phosphoinositide transfer protein, increases metastatic potential in breast, colon, and melanoma cancers, while its silencing results in Golgi compaction and functional disruption of the GOLPH3 complex [12]. Collectively, these findings indicate that GOLPH3 constitutes the functional core of a Golgi-localized oncogenic complex whose altered activity promotes cell growth, migration, and dissemination. In recent years, altered GOLPH3 expression has been reported in a wide variety of tumors, supporting its conserved oncogenic role across all malignancies. Amplification or overexpression of GOLPH3 is associated with increased tumor aggressiveness, therapeutic resistance, and a poor prognosis [13].**Figure 1** illustrates GOLPH3 mRNA expression in different tumor types, revealing low tumor specificity but

consistently elevated expression in several malignancies, including lung, breast, and prostate cancer, consistent with its widespread oncogenic activity. Among the tumors in which GOLPH3 is dysregulated, prostate cancer and non-small cell lung cancer (NSCLC) deserve particular attention due to their high incidence and clinical impact. In prostate cancer, GOLPH3 overexpression has been linked to increased tumor aggressiveness through modulation of the AKT/mTOR pathway, a central signaling cascade that regulates cell growth and survival. This activation promotes cell proliferation, reduces apoptosis, and contributes to resistance to chemotherapy and hormonal therapy in advanced disease. Furthermore, GOLPH3 controls the structure of the Golgi apparatus and vesicular trafficking, facilitating the secretion of growth factors involved in tumor migration and invasion, key characteristics of metastatic prostate cancer. Similarly, in NSCLC, GOLPH3 overexpression drives tumor progression through activation of the AKT/mTOR axis, promoting proliferation, invasion, and angiogenesis. High GOLPH3 expression is associated with poor prognosis, advanced disease stage, and increased VEGF-mediated angiogenic activity, likely resulting from secretory alterations dependent on Golgi apparatus rearrangement[14]. Overall, these data establish GOLPH3 as a crucial molecular player in cancer progression, acting both as a structural regulator of the Golgi apparatus and as a signaling modulator that enhances tumor survival, invasion, and therapeutic resistance.

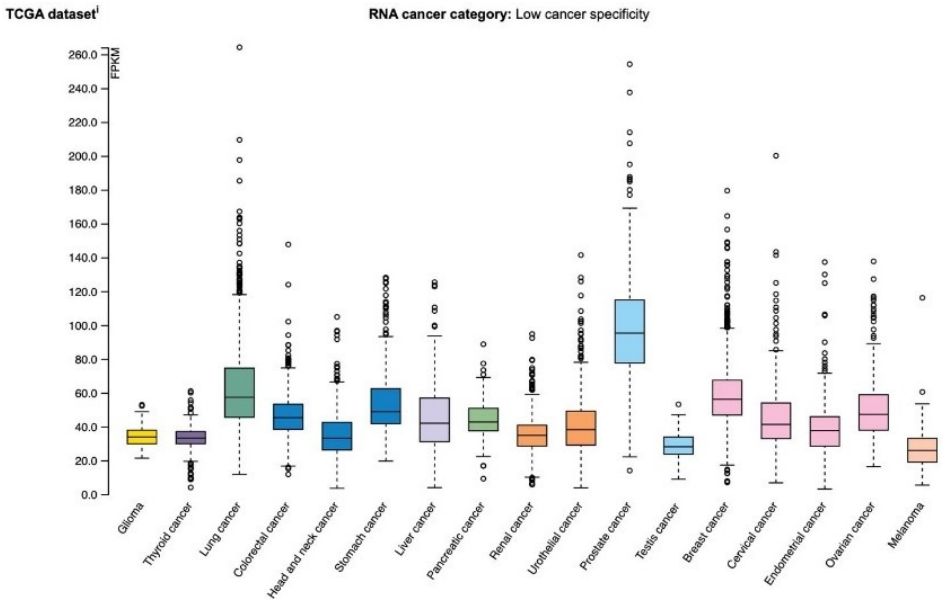

Figure 1. GOLPH3 RNA expression levels across a range of tumor types. A box plot showing GOLPH3 RNA expression levels across a range of tumor types, indicating low tumor specificity but consistently high expression in several malignancies, including lung, breast, and prostate cancer. These data support a widespread oncogenic role for GOLPH3.

1.3 The Golgi apparatus and GOLPH3 in cancer biology

The Golgi apparatus is a central organelle responsible for the post-translational modification, sorting, and trafficking of proteins and lipids within the cell [15]. By coordinating processes such as glycosylation and vesicle-mediated transport, the Golgi plays a fundamental role in maintaining cellular homeostasis and regulating signal transduction pathways [16]. Vesicular trafficking from the Golgi is essential for the correct localization of receptors, signaling molecules, and secreted factors. Through tightly regulated anterograde and retrograde transport, the Golgi controls the spatial and temporal activation of signaling cascades involved in cell growth, migration, and survival. Disruption of these processes can lead to aberrant signal amplification and sustained oncogenic signaling [6].

In recent years, increasing evidence has linked Golgi dysfunction to cancer development and progression. Alterations in Golgi structure, trafficking dynamics, and lipid composition have been associated with enhanced proliferation, invasiveness, and metastatic potential [15]. Collectively, these findings support a revised view of the Golgi apparatus as an active contributor to oncogenic signaling networks rather than merely a passive trafficking station. Golgi phosphoprotein 3 (GOLPH3), also known as GPP34, GMx33, or MIDAS, is a ubiquitously expressed protein predominantly localized to the Golgi apparatus. It was initially characterized for its role in maintaining Golgi structure and regulating vesicle trafficking, functions that are essential for normal cellular physiology [11].

GOLPH3 has recently gained increasing attention for its involvement in oncogenic processes. The discovery of the role of GOLPH3 in cancer dates back to studies that have highlighted its gene amplification and overexpression in several types of solid tumors, including lung cancer, breast cancer, hepatocellular carcinoma, gastric carcinoma and prostate cancer[17]. Overexpression of GOLPH3 is frequently associated with an unfavorable clinical prognosis, related to increased tumor aggressiveness, resistance to chemotherapy and increased metastatic capacity [10]. Overall, these findings identify GOLPH3 as an important oncogenic driver and a promising therapeutic target, whose modulation could represent an effective strategy to counter tumor progression and cancer aggressiveness.

1.3.1 The role of GOLPH3 in the Golgi apparatus

The localization of GOLPH3 to the Golgi membrane is mediated by its ability to bind to phosphatidylinositol 4-phosphate (PI4P), a highly enriched phospholipid at the Golgi transmembrane [10].The production of PI4P at the trans-Golgi membrane relies on the activity of a

phosphatidylinositol 4-Kinase (PI-4-kinase), which require the delivery of phosphatidylinositol 4-phosphate by phosphatidylinositol transfer proteins (PITPs).

By recognizing PI4P, GOLPH3 is selectively recruited to Golgi cisternae, where it functions as a lipid effector protein that translates membrane lipid composition into downstream mechanical and trafficking events [18]. This interaction is essential for the maintenance of Golgi structure and for the regulation of vesicle formation, maturation, and directional trafficking toward the plasma membrane and other intracellular compartments. In addition to binding PI4P, GOLPH3 interacts closely with the unconventional myosin, myosin XVIIIA (MYO18A), a motor protein that associates with filamentous actin (F-actin). Through this interaction, GOLPH3 establishes a physical and functional link between the Golgi membrane and the actin cytoskeleton [19] **(Figure 2**).

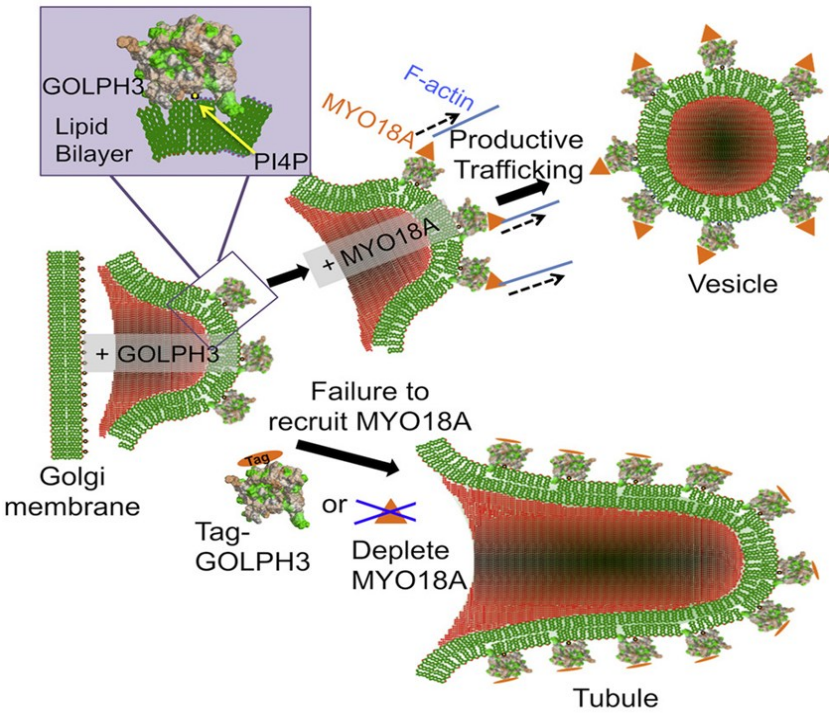

Figure 2. Role of GOLPH3 in the Golgi apparatus and tumorigenesis. GOLPH3 interacts with PI4P and MYO18A, linking the Golgi apparatus to the actin cytoskeleton (F-actin) and generating the tensile forces required for vesicle trafficking and maintenance of the Golgi ribbon structure [18].

The formation of the PI4P/GOLPH3/MYO18A/F-actin complex enables the transmission of actin-generated mechanical forces to the Golgi apparatus, generating tensile stress along Golgi membranes. This mechanical tension is critical for efficient vesicle budding, membrane tubulation, and vesicle fission processes, which collectively support dynamic Golgi trafficking [18].

The coordinated action of PI4P binding and actomyosin coupling allows GOLPH3 to regulate Golgi ribbon architecture and cisternal morphology. In addition, the PI4P/GOLPH3/MYO18A axis ensures proper protein processing, post-translational modification, secretion, and intracellular transport, thereby maintaining cellular homeostasis and supporting normal signaling dynamics [18]. Disruption of any component of this complex (*e.g.*, PI4P availability, GOLPH3 expression, MYO18A function, or actin integrity results in Golgi compaction, altered cisternal curvature, and impaired vesicular trafficking.

Indeed, exposure of mammalian cells to agents that induce DNA double-strand breaks, such as ionizing radiation, camptothecin, or doxorubicin, has been shown to activate a DNA damage-dependent signaling pathway involving DNA-dependent protein kinases (DNA-PK). DNA-PK-mediated phosphorylation of GOLPH3 enhances its interaction with MYO18A and the actin cytoskeleton, thereby increasing the tensile force applied to the Golgi apparatus. This process causes a marked alteration in the morphology of the Golgi, from the typical perinuclear ribbon to a fragmented, punctuated structure dispersed throughout the cytoplasm (**Figure 3**)**.** These data suggest that the activation of the DNA-PK–dependent signaling cascade represents a critical link between DNA damage and Golgi apparatus remodeling. Phosphorylation of GOLPH3 and its enhanced interaction with MYO18A and the actin cytoskeleton translate genotoxic stress into mechanical forces that disrupt Golgi architecture, leading to its fragmentation and cytoplasmic dispersion. This Golgi remodeling response is increasingly recognized as an adaptive mechanism that supports cell survival under stress conditions, while also contributing to tumor progression and resistance to therapy, highlighting the central role played by GOLPH3 as a relevant target for therapeutic strategies [20].

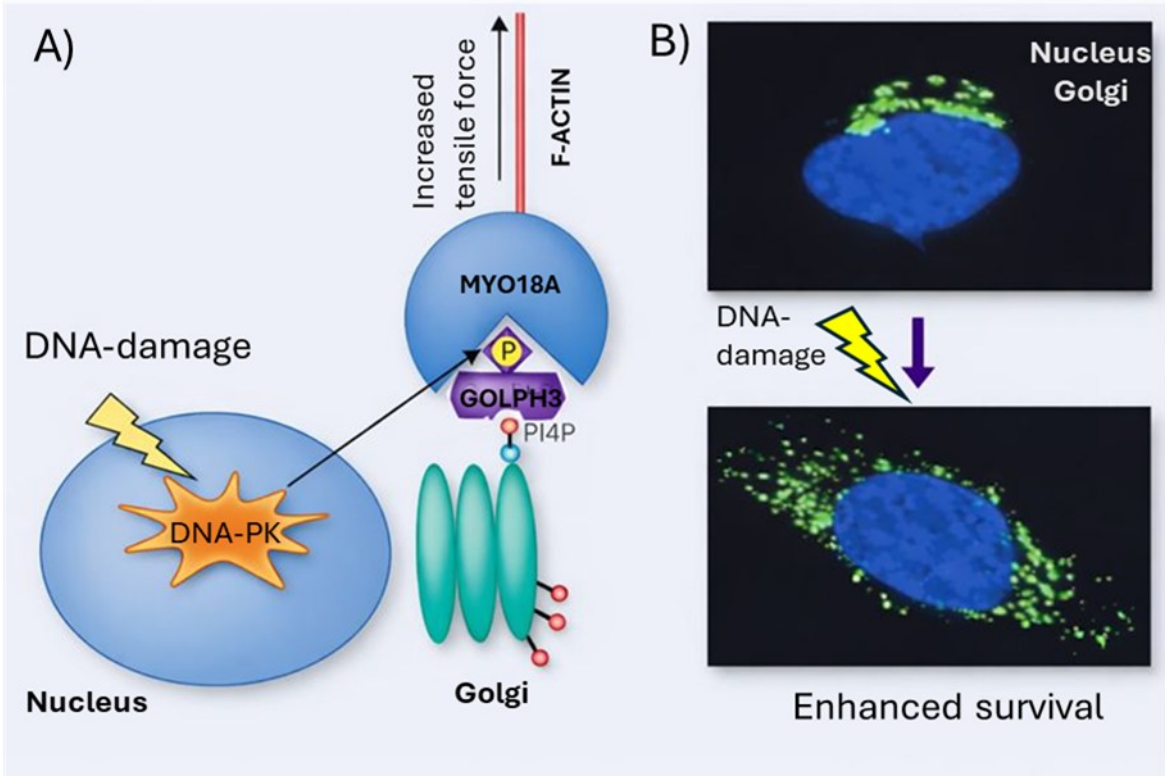

Figure 3. Role of GOLPH3 in the DNA damage response. A) Upon DNA damage, the nuclear kinase DNA-PK is activated and promotes the phosphorylation of the effector protein GOLPH3. GOLPH3, anchored to the trans-Golgi membrane via the phosphoinositide PI4P, acts as a molecular adaptor by recruiting the unconventional myosin MYO18A. The interaction between phosphorylated GOLPH3 and MYO18A increases the tensile force exerted by F-actin filaments on Golgi membranes. **B)** Immunofluorescence images show the reorganization of the Golgi compartment (green) relative to the nucleus (blue, DAPI). Under basal conditions, the Golgi exhibits a compact perinuclear morphology. DNA damage induction triggers Golgi dispersion and fragmentation throughout the cytoplasm. This structural remodeling is associated with an enhanced survival phenotype, suggesting a critical role for this pathway in the mechanisms of chemoresistance and tumor progression [20].

Glycosylation is one of the most critical post-translational modifications for maintaining proper cellular function, influencing the stability, localization, and biological activity of both proteins and lipids. This process occurs primarily in the endoplasmic reticulum (ER) and the Golgi apparatus, where resident glycosyltransferases and glycosidases catalyze the sequential addition and removal of sugar groups in N-linked and O-linked glycosylation reactions. Through its interaction with PI4P, GOLPH3 also facilitates the incorporation of glycosyltransferases into Coat Protein Complex I (COPI) vesicles, intracellular transport vesicle that mediate protein trafficking within the Golgi apparatus and from the Golgi back to the endoplasmic reticulum, ensuring their continuous recycling between Golgi cisternae and the maintenance of proper enzyme compartmentalization [21]. In

addition, by coupling Golgi membranes to the actin cytoskeleton via MYO18A, GOLPH3 provides the mechanical forces required for efficient vesicle budding and fission. This coordinated mechanism preserves Golgi architecture, sustains glycosylation fidelity, and supports normal protein processing and signaling.

Furthermore, this function is essential for the biosynthesis of glycosphingolipids (GSLs), crucial plasma membrane components that modulate receptor signaling and membrane dynamics [22].

GSL synthesis begins in the ER, where ceramide synthases (CerS1–6) produce ceramide, which is subsequently transferred to the Golgi by lipid transfer proteins such as CERT and FAPP2. In the Golgi, ceramide is converted to glucosylceramide (GlcCer) and lactosylceramide (LacCer), which serve as precursors for complex GSLs such as GM3 and Gb3. The spatial distribution of these enzymes along the cis-trans axis of the Golgi determines the final composition of GSLs. Under physiological conditions, GOLPH3 ensures the balanced recycling of these enzymes, maintaining Golgi homeostasis and supporting the normal glycosylation of receptors involved in the PI3K/AKT/mTOR pathway. Properly glycosylated receptors display regulated ligand binding and controlled signal transduction, supporting cell proliferation and survival. Relevantly, GOLPH3 depletion alters Golgi architecture, enzyme trafficking, and causes incomplete receptor glycosylation, resulting in impaired PI3K/AKT/mTOR signaling activation and reduced proliferative capacity. Conversely, GOLPH3 overexpression increases COPI vesicle formation and causes glycosyltransferase accumulation in the Golgi, promoting receptor hyperglycosylation. These hyperglycosylated receptors exhibit increased affinity for growth factors and support the aberrant activation of oncogenic pathways, particularly mTORC1 and mTORC2, which drive uncontrolled cell growth and survival as discussed below in paragraph 1.5 [23](**Figure 4**).

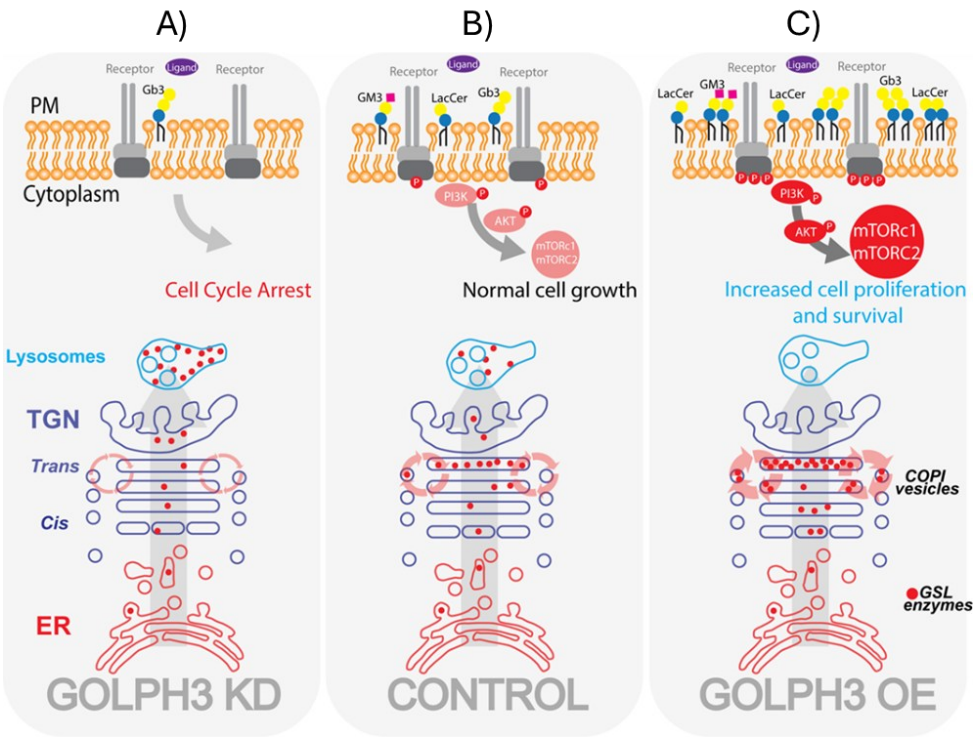

Figure 4. Model of the oncogenic role of GOLPH3 in regulating GSL enzyme trafficking and activating membrane signaling. A) In the absence of GOLPH3, the COPI vesicle-mediated retrograde recycling mechanism is compromised. The enzymes responsible for GSL biosynthesis, no longer effectively retained in the Golgi cisternae, are transported to the lysosomal compartment for degradation. The resulting depletion of GSL at the plasma membrane prevents the correct assembly of receptor complexes, inhibiting the PI3K/AKT/mTOR signaling cascade and causing cell cycle arrest. **B)** Under basal expression conditions, GOLPH3 ensures a dynamic balance between the anterograde transport and retrograde recycling of GSL enzymes. This allows for an optimal plasma membrane lipid composition for physiological signal transduction, supporting normal cell proliferation. **C)** Upregulation of GOLPH3 enhances the sequestration of GSL enzymes within the trans-Golgi and the Trans-Golgi Network (TGN) via increased COPI-dependent retrograde trafficking. This leads to an enrichment of specific GSLs (such as LacCer and Gb3) on the plasma membrane. The excess of these lipid species promotes the clustering of surface receptors and their hyperactivation, which translates into a constitutive mitogenic signaling mediated by AKT and mTORC1/2. This mechanism promotes evasion of apoptosis and accelerated tumor growth [23].

1.4 GOLPH 3-mediated signaling pathways

At the molecular level, GOLPH3 contributes to tumor progression by modulating key oncogenic signaling pathways, most notably the mechanistic target of rapamycin (mTOR) pathway. mTOR is a central regulator of cell growth, proliferation, metabolism, and survival, and its aberrant activation is a hallmark of many cancers. The mTOR pathway mTORC1 and mTORC2 [17]. GOLPH3 facilitates mTOR pathway activation through its interaction with PI4P and its role in Golgi-derived vesicle trafficking. By influencing the localization and activation of Rag GTPases, GOLPH3 contributes to the recruitment of mechanistic target of rapamycin complex 1 (mTORC1) to the lysosomal surface,

a critical site for its activation. mTORC1 is a multiprotein complex composed of mTOR, Raptor, mLST8, PRAS40 and DEPTOR, and acts as a central regulator of cell growth by controlling protein synthesis, lipid biosynthesis and autophagy in response to nutrient availability and growth factors. Through this mechanism, GOLPH3 enhances mTORC1 signaling, thereby promoting protein synthesis, cell growth and resistance to rapamycin [17].

In contrast, mechanistic target of rapamycin complex 2 (mTORC2), which includes mTOR, Rictor, mSIN1, Protor, mLST8 and DEPTOR, primarily regulates cell survival, metabolism and cytoskeletal organization by phosphorylating downstream targets such as AKT, SGK1 and PKC. Although mTORC2 is generally considered rapamycin-insensitive and is not directly regulated by Rag GTPases, aberrant activation of the mTOR pathway contributes to tumor progression and therapy resistance [24].This mechanism contributes to increased tumor cell growth and resistance to therapeutic stress. In addition to mTOR signaling, GOLPH3 supports the PI3K/AKT signaling cascade, which acts upstream of mTOR and is frequently overactivated in cancer, contributing to increased cell proliferation and inhibition of apoptosis. In addition to its role in growth signaling, GOLPH3 also promotes the secretion of pro-tumorigenic factors, including vascular endothelial growth factor (VEGF), thereby promoting angiogenesis. Through its combined effects on Golgi organization, trafficking, and signaling integration, GOLPH3 acts as a central driver of oncogenic signaling cascades that support tumor survival, progression, and dissemination [12] (**Figure 5**).

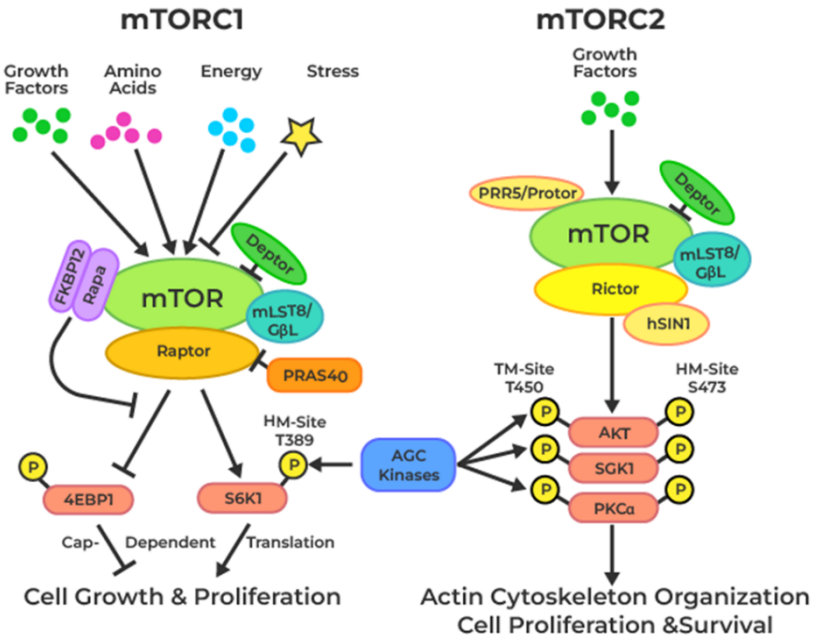

Figure 5. GOLPH3 activation of the mTOR pathway. The mTOR kinase functions as a key regulatory center of cellular homeostasis through the formation of two functionally and structurally distinct multiprotein complexes. mTORC1,

defined by the presence of the adaptor protein Raptor. This complex integrates heterogeneous stimuli, including growth factors, amino acid availability, energy status (ATP), and cellular stress. Activation of mTORC1 promotes cellular anabolism and cell cycle progression through the phosphorylation of its main downstream targets: the kinase S6K1 (at site T389) and the translation initiation binding protein 4EBP1. These events stimulate cap-dependent protein synthesis, driving cell growth and proliferation. The complex is negatively modulated by Deptor and PRAS40 and is sensitive to inhibition by Rapamycin via the FKBP12 complex. mTORC2, characterized by the presence of the protein Rictor and the mSIN1 component. Unlike mTORC1, mTORC2 responds predominantly to growth factors and is considered the master regulator of actin cytoskeleton organization. Its enzymatic function is crucial for the full activation of AKT via phosphorylation of the hydrophobic site (HM-Site S473) [23].

1.5 Current cancer therapies

Conventional cancer treatments primarily include surgery, radiotherapy, and chemotherapy, often complemented by targeted therapies and immunotherapy. While these approaches have substantially improved patient survival and quality of life, they continue to present significant limitations that restrict their effectiveness and broader application in clinical practice [4].Surgery is often the first therapeutic intervention, aimed at physically removing the tumor and surrounding tissue. However, it is not always applicable in cases of metastatic disease or tumors located in inaccessible areas [25]. Chemotherapy, on the other hand, acts on rapidly proliferating cells but lacks specificity, causing systemic side effects that can be severe. Furthermore, the emergence of drug resistance mechanisms represents a relevant clinical problem, reducing the efficacy of treatment. Radiation therapy uses ionizing radiation to damage the DNA of tumor cells, causing apoptosis and slowing tumor growth. Despite its effectiveness, it can cause side effects in surrounding healthy tissue, and in some cases, tumors may develop resistance to radiation-induced damage. Targeted therapies, including tyrosine kinase inhibitors, monoclonal antibodies, and inhibitors of specific molecular pathways, have improved therapeutic precision by acting on specific targets involved in tumor growth and survival. However, these strategies can also be limited by secondary mutations, tumor variability, and difficulties in targeting some key oncogenes. In addition to these main approaches, other traditional therapies exist specifically for certain tumor types. Hormone therapy is indicated for hormone-dependent tumors, such as breast and prostate cancer, and works by blocking the production or action of hormones that stimulate tumor growth. This strategy is relatively well tolerated and can prevent recurrence, but is not effective in hormone-insensitive tumors and can induce resistance or systemic side effects [25]. Hyperthermia involves localized heating of tumor cells, often in combination with radiation or chemotherapy, with the goal of increasing the tumor's sensitivity to treatment. Despite its potential benefits, this technique is technically complex, poorly available, and can cause local side

effects such as burning or pain. Cryotherapy, or cryoablation, on the other hand, induces tumor tissue necrosis through freezing and represents a minimally invasive alternative for inoperable patients; however, it is not indicated for large or deep tumors and carries the risk of damaging surrounding tissue [26]. Finally, photodynamic therapy (PDT), based on the administration of a photosensitizer followed by illumination of tumor cells, is particularly suitable for superficial skin, lung, esophageal, or bladder tumors. Although selective and minimally invasive, PDT is limited by poor light penetration into deep-seated tumors and can induce cutaneous photosensitivity. In summary, although traditional therapies have been and remain the backbone of cancer treatment, they present significant limitations related to specificity, systemic toxicity, resistance, and applicability, underscoring the need to develop more innovative and personalized approaches [7]. To overcome these limitations, gene therapy strategies have emerged as potential innovative and more specific approaches. Among these, RNA interference (RNAi), mediated by small interfering RNAs (siRNA), offers the possibility of silencing the expression of oncogenic genes in a targeted manner, acting directly on the messenger (mRNA) before it is translated into proteins (**Table1**).

Conventional Therapy	Application / Cancer Stage	Advantages	Disadvantages / Limitations
Surgery	Localized tumors; early stage	Direct removal of tumor and surrounding tissue; potentially curative; can be combined with adjuvant therapy	Not applicable in metastatic disease or inaccessible tumors; surgical risks; possible residual tumor
Chemotherapy	Localized or advanced/metastatic tumors; systemic disease	Effective against rapidly dividing cells; can target metastatic sites	Non-specific; systemic toxicity (myelosuppression, nausea, alopecia, immunosuppression); development of drug resistance
Radiotherapy	Localized or locally advanced tumors; adjuvant/neoadjuvant	Induces DNA damage leading to tumor cell death; can shrink tumors before surgery; combinable with other therapies	Can damage surrounding healthy tissue; tumors may develop radioresistance; limited to accessible sites
Hormone Therapy	Hormone-dependent tumors (breast, prostate); various stages	Specific for hormone-sensitive tumors; can prevent recurrence; generally well-tolerated	Ineffective in hormone-insensitive tumors; endocrine-related side effects; resistance may occur
Hyperthermia / Thermal Ablation	Selected solid tumors; often combined with chemo/radiotherapy	Minimally invasive; can enhance effectiveness of other treatments	Limited availability; technically complex; local effects (burns, pain)
Cryotherapy / Cryoablation	Localized tumors (kidney, prostate, lung); selected patients	Minimally invasive; alternative for non-surgical candidates	Not suitable for large or deep tumors; risk of damage to surrounding tissue

Photodynamic Therapy (PDT)	Superficial tumors (skin, lung, esophagus, bladder)	Selective for treated cells; minimally invasive	Limited penetration of light; ineffective for deep tumors; photosensitivity reactions

Table 1. Comparative summary of the characteristics, benefits, and limitations of the main therapeutic strategies against cancer. The table outlines the main traditional therapeutic strategies against cancer, with their application and cancer stage, advantages and disadvantages.

1.6 siRNA-mediated gene silencing

RNA interference is a highly conserved natural mechanism of post-transcriptional gene regulation, present in nearly all eukaryotic organisms [27] This biological process allows cells to fine-tune gene expression and serves as a defense mechanism against exogenous genetic elements, including RNA viruses and transposable elements. At the molecular level, RNAi is mediated by small, double-stranded RNA molecules, such as short interfering RNA or microRNAs (miRNA), which are typically 21–23 nucleotides long. These molecules guide the RNA-induced silencing complex (RISC) to complementary target mRNAs, thereby controlling the stability and translation of these transcripts. Once introduced into a cell, through methods such as chemical transfection, nanoparticle-mediated delivery, viral vectors, or plasmid expression, siRNA sequences are incorporated into the RISC, a multiprotein effector complex essential for RNAi activity. Within the RISC, the passenger strand of the siRNA duplex is selectively removed, allowing the guide strand to direct the complex to complementary sequences on the target mRNA. This results in sequence-specific cleavage and degradation of the mRNA, ultimately leading to robust and highly specific knockdown of the corresponding gene [28]. This precise mechanism of action makes RNAi a powerful tool for functional genomics, allowing researchers to systematically study the role of individual genes in cellular processes, development, and disease [9]. The potential of RNAi has been widely explored in the development of targeted therapeutic strategies, particularly in the fields of oncology, antiviral therapy, and the treatment of inherited genetic diseases [27]. In principle, siRNA-mediated gene silencing can be employed to selectively downregulate oncogenes, inhibit viral replication, or correct disease-causing genetic aberrations, thereby offering a level of specificity that is largely unattainable with conventional small-molecule drugs or protein-based therapies. Furthermore, RNAi-based approaches are extremely versatile and can be designed to target virtually any gene of interest, including those traditionally considered "non-druggables, whose protein products cannot be easily inhibited with conventional small molecules or antibodies, such as transcription factors, scaffolding proteins, or other regulatory molecules [29].

Despite these promising properties, the clinical translation of RNAi-based therapies faces several significant challenges. Naked siRNAs are intrinsically unstable in biological fluids and are rapidly degraded by nucleases, limiting their bioavailability [30]Furthermore, their cellular uptake is inefficient, often requiring sophisticated delivery systems to reach target tissues and cells in vivo. Other challenges include immune activation, off-target gene silencing, and the potential risk of unwanted side effects. Consequently, much of the current research on RNAi-based therapies focuses on developing biocompatible, efficient, and targeted delivery systems, such as lipid nanoparticles, polymeric carriers, and conjugated molecules, to overcome these obstacles and enable safe and effective clinical applications. Overall, RNAi represents a revolutionary molecular tool that not only advances our understanding of gene function but also offers enormous therapeutic potential. Its precise, sequence-specific action and adaptability make it an invaluable platform for modern biomedical research and a promising avenue for future targeted therapies [31].

1.6.1 Molecular mechanism of siRNA-mediated gene silencing

siRNA-mediated gene silencing exploits the natural mechanism of RNA interference to reduce the expression of specific genes in a sequence-dependent manner. siRNA, short double-stranded RNA molecules, guide specialized cellular proteins to target mRNAs, promoting their degradation or inhibiting translation. This process allows for precise and reversible control of gene expression, making siRNA powerful tools for both molecular biology studies and targeted therapeutic applications. The effectiveness of silencing depends on the specific interaction between the siRNA guide strand and the target mRNA, the correct assembly of the RISC protein complex, and the cell's ability to degrade or sequester the target transcripts. After entering the cytoplasm, the siRNA duplex is incorporated into the RISC loading complex, which includes Dicer, the RNA-binding protein TRBP, and Argonaute 2 (Ago2). Dicer facilitates the processing of longer double-stranded RNAs or the transfer of synthetic siRNAs to Ago2, while TRBP contributes to the recruitment and stabilization of the complex. Ago2 represents the catalytic core of the RISC and is essential for siRNA-guided silencing. During RISC assembly, the passenger strand of the duplex is cleaved and eliminated, leaving the guide strand associated with Ago2 within the activated RISC complex [32]. The guide strand then directs the RISC toward complementary sequences of the target mRNA through Watson–Crick base pairing. The high specificity of this interaction allows for efficient silencing; in the presence of perfect or near-perfect complementarity, the mRNA is correctly positioned for cleavage. Under these conditions, Ago2 exerts its endonuclease ("slicer") activity, cutting the mRNA in a defined region and generating fragments that are rapidly degraded by cellular exonucleases, thus preventing protein translation. Alternatively, when the complementarity between the guide strand and

the mRNA is imperfect, RISC can inhibit gene expression without inducing direct cleavage of the transcript. In this case, RISC-associated mRNAs can be sequestered in processing bodies (P-bodies), cytoplasmic structures enriched in enzymes involved in mRNA decay and storage, where the transcripts are temporarily stored or subjected to degradation [33]. After cleavage or translational repression of the target mRNA, the activated RISC complex can dissociate from the transcript and bind to additional mRNA molecules, allowing multiple rounds of silencing from a single guide strand. This recycling mechanism contributes significantly to the high efficiency of RNA interference (**Figure 6**).

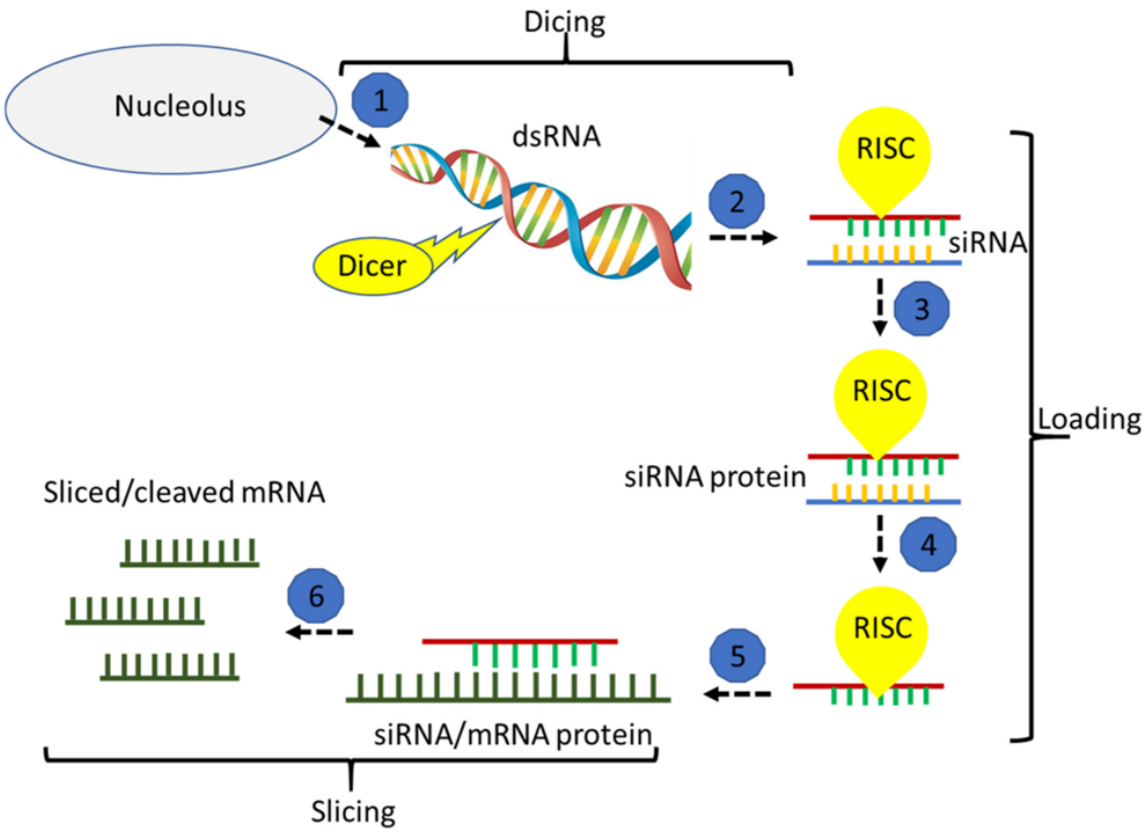

Figure 6. Molecular mechanism of siRNA-mediated gene silencing. The siRNA duplex is incorporated into the RISC complex, where the guide strand directs the degradation of the target complementary mRNA or inhibits its translation, allowing sequence-specific control of gene expression [32].

This mechanism allows for precise and targeted post-transcriptional control of gene expression, making siRNA a powerful tool for silencing oncogenes such as GOLPH3, even in cases where the encoded proteins are not easily inhibited by traditional drugs.

1.7 siRNA delivery systems

Despite the high specificity of siRNA in silencing target genes, the clinical application of this technology is severely limited by its instability and poor bioavailability *in vivo* [34].Naked siRNA is highly susceptible to rapid degradation by plasma ribonucleases, resulting in a short circulating half-life following systemic administration. In addition, its hydrophilic and negatively charged nature severely limits passive diffusion across the cell membrane, leading to inefficient cellular uptake. Together, these physicochemical and biological barriers substantially hinder the therapeutic application of naked siRNA in vivo, underscoring the need for effective delivery strategies to protect siRNA from degradation and facilitate its intracellular delivery [34]. Furthermore, siRNA can activate the innate immune system, in particular through the receptors TLR3, TLR7 and TLR8, generating a nonspecific inflammatory response that limits its safe use *in vivo*. To obtain a significant therapeutic effect, it is therefore necessary to use delivery systems that protect the siRNA from degradation, favor its accumulation in the target tissue and promote its endocytosis and release into the cell cytoplasm, where it can interact with the RISC complex. The several limitations associated with the therapeutic use of siRNAs, including their instability in biological fluids, rapid enzymatic degradation, poor cellular uptake, and potential immune activation, make the development of effective delivery systems essential. In this context, nanoparticles can enhance siRNA therapy by protecting the molecules from degradation, facilitating targeted accumulation in the desired tissue, promoting cellular internalization via endocytosis, and enabling controlled intracellular release, all of which improve the overall efficacy of gene silencing [35].

Indeed, gene therapy carriers represent fundamental tools for overcoming the numerous obstacles that limit the clinical application of siRNA. These vectors **(Table 2)** can be divided into natural, such as liposomes, attenuated viral vectors, and peptide or protein-based nanoparticles, and synthetic, such as polymeric nanoparticles, dendrimers, cationic lipids, and functionalized hybrid systems [30]. Natural vectors generally offer good biocompatibility, the ability to interact with cellular processes, and often exhibit intrinsic tissue-targeting properties. Synthetic vectors, on the other hand, allow for greater modularity in design, precise control of size and surface properties, and the possibility of functionalization for the specific targeting of tumor tissues through ligands, antibodies, peptides, or sugars recognized by receptors present on malignant cells [36].

In addition to protecting siRNA from enzymatic degradation, these carriers enhance the molecules' entry into cells through various internalization mechanisms, such as receptor-mediated endocytosis, direct membrane fusion, or micropinocytosis. Furthermore, many advanced systems allow controlled

release of siRNA into the cytoplasm, sensitive to internal stimuli (acid pH, specific enzymes, redox environment) or external stimuli (light, ultrasound, heat), thus optimizing drug availability at the site of action and reducing systemic side effects. In summary, carriers represent a key strategy for making siRNA therapy safe, effective, and targeted, opening up new perspectives for personalized clinical applications [9].

Vector Type	Examples	Advantages	Disadvantages
Natural vectors	Viral vectors (adenovirus, lentivirus), extracellular vesicles (exosomes)	High delivery efficiency; efficient cellular uptake; potential intrinsic targeting properties	Immunogenicity; safety concerns; limited cargo capacity; complex and costly production
Synthetic vectors	Lipid nanoparticles, cationic lipids, polymers (e.g., PEI), dendrimers	Tunable physicochemical properties; scalable and reproducible manufacturing; reduced immunogenicity; formulation versatility	Potential cytotoxicity; lower delivery efficiency in some contexts; limited targeting specificity without functionalization
Hybrid systems	Lipid–polymer nanoparticles, biomimetic nanoparticles	Improved stability and delivery efficiency; enhanced biocompatibility by combining natural and synthetic features	Increased formulation complexity; potential challenges in scalability and reproducibility

Table 2. Natural and synthetic vectors for siRNA delivery: advantages and limitations

1.8 Nanoparticles: characteristics and potential in the field of nanomedicine

Nanomedicine represents one of the most innovative and rapidly evolving fields of biomedical research, focusing on the use of materials, devices, and systems with nanometric dimensions (1–100 nm) for the diagnosis, treatment, and prevention of diseases. The development of nanomedicine is based on the ability of nanoscale materials to interact with biological components, such as proteins, membranes, and nucleic acids at the molecular and cellular level, thus enabling precise control over biological responses. Nanoparticles (NPs) are defined as particulate structures with at least one dimension in the nanometric range (1–100 nm). At this scale, materials exhibit unique physicochemical, optical, electrical, and mechanical properties that differ significantly from their bulk counterparts, due to quantum size effects and high surface area-to-volume ratios. These distinctive characteristics make nanoparticles highly versatile tools for biomedical applications, as they can be engineered to optimize drug solubility, stability, biodistribution, and cellular uptake. In the biomedical field, nanoparticles serve as carriers for the delivery of therapeutic and diagnostic agents, including small-molecule drugs, nucleic acids (such as siRNA and mRNA), proteins, peptides,

and imaging probes. By modulating parameters such as size, surface charge, morphology, and surface functionalization, it is possible to design nanoparticles that achieve targeted and controlled release, enhance bioavailability, and reduce systemic toxicity compared to conventional formulations [37]. Moreover, nanoparticles can be designed as stimuli-responsive systems, capable of releasing their payload in response to specific internal or external cues such as pH, redox potential, enzymes, temperature, light, or magnetic fields thus ensuring spatiotemporal precision in therapy. In parallel, the application of nanoparticles in diagnostics and theragnostic has enabled advances in imaging, biosensing, and real-time monitoring of disease progression. Overall, nanoparticles represent a fundamental component of nanomedicine, offering a multifunctional platform that integrates chemistry, biology, and materials science to advance the development of next-generation personalized therapeutic and diagnostic solutions [38].

1.8.1 Types of nanoparticles

Nanoparticles can be classified into two main macro-categories based on their composition: inorganic and organic, each with unique characteristics that determine their application in the biomedical and pharmacological fields (**Table 3**).

Nanoparticle Type	Advantages	Disadvantages
Gold nanoparticles (AuNPs)	Low cytotoxicity, chemical inertness; easy functionalization with drugs, nucleic acids, antibodies; excellent optical properties (SPR) for imaging and photothermal therapy; tunable size and shape.	Potential accumulation in tissues; size- and shape-dependent biodistribution may complicate delivery; cost of production.
Superparamagnetic iron oxide nanoparticles (SPIONs)	Magnetic properties allow active targeting and localized drug release; applications in MRI contrast, hyperthermia, and radiotherapy; good biocompatibility.	Non-biodegradable; risk of long-term tissue accumulation; requires coatings for in vivo safety.
Ceramic nanoparticles (MSNs)	High drug loading capacity due to porous structure; controllable release; easily functionalizable surface for targeting; good *in vitro* biocompatibility.	Poor biodegradability; potential systemic accumulation; purification and modification required to improve degradability.
Carbon nanotubes (CNTs)	Excellent mechanical and electrical properties; high loading capacity for drugs, genes, or proteins; tunable surface chemistry.	Potential cellular toxicity (oxidative stress, inflammation, apoptosis); biocompatibility concerns; challenges in in vivo use.
Nanodiamonds (NDs)	Small size (2–9 nm); easily functionalizable surface; good biocompatibility; promising for drug delivery and diagnostics.	Limited preclinical and clinical data; production and functionalization can be costly.
Liposomes	High biocompatibility and biodegradability; can encapsulate both hydrophilic and	Relatively low encapsulation efficiency for some drugs; stability issues; rapid release kinetics.

	hydrophobic molecules; clinically approved and widely used.

Table 3. Comparative analysis of the main nanoparticle platforms. The table summarizes the advantages and limitations of different nanosystems, highlighting the balance between chemical and physical properties, loading capacity, and biocompatibility profiles for therapeutic and diagnostic applications.

Among inorganic nanoparticles, the most studied and applied are gold nanoparticles (AuNPs). These particles, with dimensions ranging from 1 to 100 nm, exhibit low cytotoxicity and high chemical inertness, characteristics that make them ideal for diagnostic and therapeutic applications. Their surface, rich in thiol groups, allows for easy functionalization with drugs, nucleic acids, antibodies, or other biomolecules, making them extremely versatile systems. Furthermore, the optical properties of AuNPs, particularly surface plasmon resonance (SPR), make them effective tools for imaging, biosensing, and photothermal therapies. Particle shape and size significantly influence the efficiency of therapeutic drug delivery, determining biodistribution, tissue penetration, and cellular interaction [39]. Superparamagnetic iron oxide nanoparticles (SPIONs) represent another class of inorganic nanoparticles of great interest. Typically composed of magnetite (Fe_3O_4) or maghemite (γ-Fe_2O_3), with dimensions between 10 and 180 nm, SPIONs exploit their magnetic properties for active targeting via external magnetic fields and for localized drug release. In addition to drug and gene delivery, these particles are used in diagnostics, as contrast agents for magnetic resonance imaging, magnetic hyperthermia, and targeted radiotherapy. Despite their good biocompatibility, their non-biodegradable nature requires attention due to the risk of long-term accumulation in tissues, which may limit their clinical use without appropriate removal strategies or biodegradable coatings. Ceramic nanoparticles, particularly mesoporous silica nanoparticles (MSNs), range in size from 20 to 100 nm and are characterized by a highly ordered and porous internal structure. This morphology allows for high drug loading capacity and controlled release. The surface of MSNs can be functionalized with peptides, nucleic acids, or antibodies, making them suitable for targeted applications. Despite good *in vitro* biocompatibility, a major limitation of ceramic particles is their poor biodegradability, resulting in persistence in the body and potential systemic accumulation. Current research focuses on the development of biodegradable coatings or chemical modifications to improve their degradation profile. Carbon-based materials, such as carbon nanotubes (CNTs) and nanodiamonds (NDs), have also attracted considerable interest. Single- or multi-walled CNTs have diameters ranging from 2.5 to 100 nm and are characterized by excellent mechanical and electrical properties, as well as a high

loading capacity for drugs, genes, or proteins. However, their potential cellular toxicity, which can manifest as oxidative stress, inflammation, or apoptosis, limits their clinical use. Nanodiamonds, by contrast, are characterized by small dimensions (2–9 nm), an easily functionalizable surface, and favorable biocompatibility. These properties make them promising platforms for drug delivery and diagnostic applications; however, further preclinical and clinical studies are required to fully establish their safety and efficacy [40].

Organic nanoparticles, by contrast, are characterized by high biocompatibility and an enhanced ability to interact with biological systems. Among these, liposomes represent one of the most well-established and widely used carriers in clinical applications. These are spherical vesicles, ranging in size from approximately 50 nm to several micrometers, consisting of one or more lipid layers surrounding an aqueous core. Thanks to their amphiphilic structure, they can transport both hydrophilic (in the aqueous core) and hydrophobic (in the lipid bilayer) molecules, making them highly versatile [41]. Liposomes offer high biodegradability and biocompatibility, but they present limitations such as relatively low encapsulation efficiency for some molecules, stability issues during storage, and rapid release kinetics. Despite these challenges, numerous liposomal formulations are already approved and used in oncology, antimicrobial, and vaccine applications [41]. Other organic systems include polymeric micelles, hydrogel nanoparticles, dendrimers, and extracellular vesicles (EVs). Polymeric micelles self-assemble in aqueous solutions using amphiphilic copolymers and are particularly suitable for transporting hydrophobic drugs, improving their bioavailability and pharmacokinetics. Hydrogel nanoparticles, three-dimensional and highly hydrophilic, can absorb large amounts of water while maintaining a stable cross-linked structure, allowing for modulated drug release in response to external stimuli such as pH, temperature, or enzymes [30,42]. Dendrimers are hyperbranched macromolecules with dimensions between 1 and 10 nm, allowing precise control of molecular mass, surface charge, and chemical functionalization; they can transport drugs or nucleic acids by binding to the surface or inserting them between the branches. EVs, including exosomes and microvesicles, are vesicles naturally secreted by cells that mediate intercellular communication and represent natural delivery systems for therapeutic molecules due to their biocompatibility and ability to cross biological barriers such as the blood-brain barrier [43]Finally, polymeric nanoparticles, the subject of further study, represent organic colloidal systems with typical dimensions between 10 and 100 nm, composed of natural or synthetic biodegradable polymers. They can take on various architectures, such as nanocapsules with a drug-containing core or nanospheres in which the active ingredient is distributed within the polymer matrix. Their versatility, biocompatibility, and ability to provide controlled release make them promise for the targeted delivery of drugs and therapeutic molecules, including nucleic acids such as siRNA. In recent years, “smart” systems have been

developed, capable of responding to external stimuli such as pH, temperature, enzymes, or radiation, allowing for selective release of the active ingredient at pathological sites and reducing systemic side effects [35](**Figure 7**).

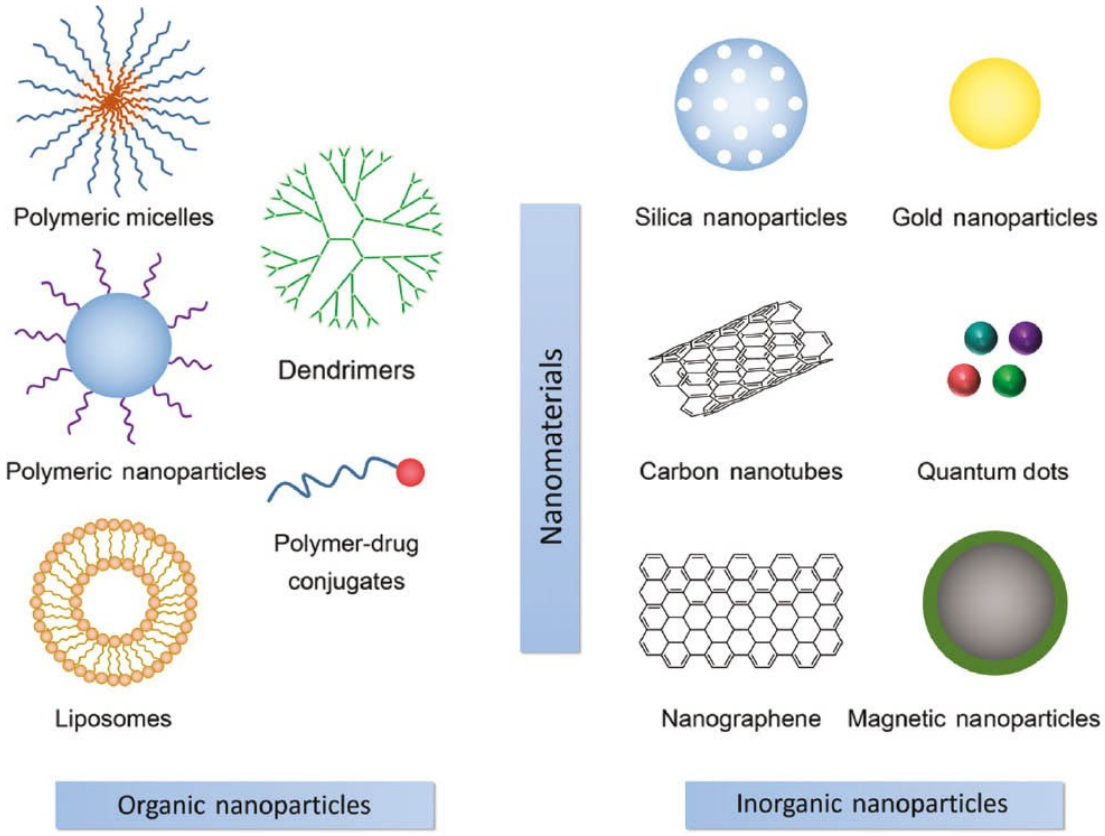

Figure 7. Classification of the main nanomaterials for biomedical purposes. The image illustrates the systematic subdivision between organic nanoparticles (such as liposomes and dendrimers) and inorganic nanoparticles (such as metals and nanotubes), highlighting the structural diversity underlying their different applications in nanomedicine.

1.9 Polymeric nanoparticles

Polymeric nanoparticles are colloidal systems typically ranging in size from 10 to 200 nanometers, made from natural or synthetic polymers. Owing to their structural and chemical versatility, these nanoparticles are considered among the most promising delivery platforms for a wide range of therapeutic agents, including small-molecule drugs, proteins, antibiotics, and nucleic acids such as siRNA. Their structure allows for the protection of the incorporated molecules, controlled release, and enhanced entry into target cells. Natural polymers, such as chitin, alginate, gelatin, collagen, and albumin, offer excellent biocompatibility and biodegradability, with a reduced risk of systemic toxicity [43]However, they show some limitations, such as batch-to-batch variability, less precise control over particle size, and lower stability in circulation. Synthetic polymers, including poly(lactic acid) (PLA), poly(glycolic acid) (PGA), poly(lactic-co-glycolic acid) (PLGA), poly(ε-caprolactone)

(PCL), polyethylenimine (PEI), and polyacrylates, enable more precise control over nanoparticle size, surface characteristics, and drug release profiles. They can also be functionalized to improve targeting or make them sensitive to external stimuli. Disadvantages include the need for organic solvents or specific synthesis conditions, the risk of tissue accumulation before complete degradation, and the potential production of local acidic byproducts. The use of polymeric nanoparticles offers numerous advantages: protection of the therapeutic load, controlled and modulated release, greater efficacy in cellular internalization, and the possibility of designing "smart" systems that respond to stimuli such as pH, temperature, enzymes, or radiation. However, some synthetic polymers may require complex synthesis conditions and sometimes present problems with tissue accumulation if not fully biodegradable [44] (**Table 4**).

Category	Nanoparticle Type	Representative Examples	Advantages for siRNA Delivery	Disadvantages / Limitations
Natural nanoparticles	**Liposomes**	Cationic liposomes (DOTAP), neutral liposomes, PEGylated liposomes	Efficient siRNA encapsulation; protection from nuclease degradation; enhanced cellular uptake; clinical validation in RNA therapeutics	Limited stability in serum; potential toxicity of cationic lipids; rapid clearance without surface modification
	Extracellular vesicles (exosomes)	MSC-derived exosomes, tumor-derived exosomes	Excellent biocompatibility; low immunogenicity; intrinsic cell-targeting ability;	Low loading efficiency; limited scalability; heterogeneity
	Protein-based nanoparticles	Albumin nanoparticles, protamine–siRNA complexes	Biodegradable; mild formulation conditions; reduced immunogenicity; receptor-mediated uptake	Limited protection against degradation; poor endosomal escape; batch variability
	Polysaccharide-based nanoparticles	Chitosan, hyaluronic acid nanoparticles	Electrostatic siRNA complexation; biodegradability; mucoadhesive and targeting properties (e.g., CD44)	Weak endosomal escape; instability at physiological pH; variable transfection efficiency
Synthetic nanoparticles	**Polymeric nanoparticles**	PLGA, PLA, PGA, PCL nanoparticles	Controlled siRNA release; tunable size and surface charge; good reproducibility; scalable production	Low encapsulation efficiency without modification; limited endosomal escape; acidic degradation products
	Cationic polymers / polyplexes	Polyethylenimine (PEI), poly(L-lysine)	Strong siRNA condensation; efficient cellular uptake; proton sponge–mediated endosomal escape	Significant cytotoxicity; non-specific interactions with serum proteins; inflammatory responses
	Lipid nanoparticles (LNPs)	Ionizable lipid-based nanoparticles	High siRNA loading efficiency; efficient endosomal escape; clinical success in approved siRNA therapies	Formulation complexity; potential immunostimulation; stability challenges
	Dendrimers	PAMAM dendrimers	Precise architecture; high siRNA loading; multivalent surface functionalization	Generation-dependent toxicity; costly synthesis; limited biodegradability
	Inorganic nanoparticles	Gold nanoparticles, silica nanoparticles, nanodiamonds	High stability; easy surface functionalization; potential for theranostic applications	Limited biodegradability; long-term accumulation; lower gene-silencing efficiency without coatings

Hybrid systems	**Lipid–polymer nanoparticles**	Lipid-coated PLGA nanoparticles	Enhanced siRNA protection; improved cellular uptake; balanced stability and biocompatibility	Increased formulation complexity; reproducibility challenges
	Biomimetic nanoparticles	Cell membrane–coated siRNA nanoparticles	Immune evasion; prolonged circulation; enhanced targeting and uptake	Complex fabrication; limited scalability; regulatory challenges

Table 4. Advantages and disadvantages of synthetic and natural polymers. Summary of the main advantages and disadvantages associated with the use of natural and synthetic polymers in drug delivery systems.

1.9.1 Methods for the synthesis of polymeric nanoparticles

The production of polymeric nanoparticles requires the use of tailored synthetic strategies that allow precise control over particle size, morphology, encapsulation efficiency, and release kinetics of the active cargo. Numerous synthesis approaches have been reported in the literature, each presenting specific advantages and limitations depending on the polymer employed and the nature of the therapeutic agent or nucleic acid to be delivered. Among the most well-established methods are:

Emulsion-solvent/evaporation: The polymer is dissolved in an organic solvent and dispersed in an aqueous phase containing surfactants. Evaporation of the solvent leads to the formation of stable nanoparticles. This method enables good control over particle size and achieves reasonable encapsulation efficiency; however, it requires the use of organic solvents, which may raise concerns regarding toxicity and residual solvent contamination. *Nanoprecipitation:* The polymer, soluble in a water-miscible organic solvent, is rapidly added to an aqueous phase, causing the controlled precipitation of the polymer in the form of nanoparticles. This method is simple, reproducible, and suitable for delicate molecules such as siRNA or peptides [45]. However, it can be less efficient for encapsulating highly hydrophilic molecules and requires careful removal of solvent residues. *Microemulsion:* This uses the formation of nanosized droplets stabilized by surfactants, in which the polymer self-assembles. It allows for high encapsulation efficiency and precise size control, but purification can be complex and scalability limited [46]. *Ionic coacervation/gelation, salting-out, and self-assembly* of amphiphilic copolymers are other methods available in the literature, often used with natural polymers or systems sensitive to external stimuli, but less commonly used for large-scale industrial production [47](**Table 5**).

Preparation Method	Principle / Mechanism	Suitability for siRNA Delivery	Advantages for siRNA	Disadvantages / Limitations	Key Parameters Influencing siRNA Performance
Emulsion–solvent evaporation (single or double emulsion)	Polymer dissolved in organic solvent is emulsified in aqueous phase; solvent removal leads to nanoparticle formation	Moderate (often requires double emulsion or cationic modification)	Good particle size control; reasonable siRNA protection when properly encapsulated; established and reproducible method	Use of organic solvents may compromise siRNA integrity; low encapsulation efficiency for hydrophilic siRNA; complex processing	Polymer type and charge; emulsifier; solvent system; stirring speed; evaporation rate
Nanoprecipitation (solvent displacement)	Rapid diffusion of solvent into aqueous phase induces polymer precipitation	Moderate to good (typically via electrostatic complexation)	Simple and mild process; narrow size distribution; compatible with siRNA polyplex formation	Limited siRNA encapsulation without cationic polymers; weak endosomal escape unless modified	Polymer concentration; solvent–water ratio; mixing rate; polymer charge density
Microemulsion	siRNA-loaded nanodroplets formed in thermodynamically stable microemulsions	Limited	Very small and uniform particle size; controlled formulation	High surfactant content; difficult purification; potential toxicity; limited clinical relevance for siRNA	Surfactant/co-surfactant ratio; phase composition; temperature
Coacervation / ionic gelation	Electrostatic interactions between oppositely charged polymers and siRNA	High	Mild, aqueous conditions; no organic solvents; strong siRNA complexation; good nuclease protection	Poor mechanical stability; broad size distribution; limited endosomal escape	Polymer charge density; pH; ionic strength; polymer-to-siRNA ratio
Salting-out	Reduced solvent miscibility induced by salts leads to nanoparticle formation	Moderate	Avoids high-energy emulsification; preserves siRNA integrity	Requires extensive purification; limited polymer compatibility; less commonly used for siRNA	Salt concentration; solvent system; dilution rate
Self-assembly of amphiphilic copolymers	Spontaneous formation of core–shell structures via hydrophobic and electrostatic interactions	High	Efficient siRNA loading (especially with cationic blocks); good stability in serum; tunable surface and targeting; improved endosomal escape	Complex polymer synthesis; higher cost; formulation sensitivity	Block composition and ratio; molecular weight; surface charge; assembly conditions

Table 5. Advantages and disadvantages of the main methods of nanosystem preparation. Preparation methods for polymeric nanoparticles for siRNA delivery: principles, advantages, and limitation.

In this study, polymeric nanoparticles were carefully designed using polymers selected for their complementary properties, aiming to optimize the stability, efficacy, and safety of the delivery system. The synthetic copolymer PLGA, for example, is widely recognized for its ability to provide

controlled release of both drugs and nucleic acids. Its excellent biocompatibility, chemical and physical stability make it particularly suitable for therapeutic applications, while also allowing for modulation of release kinetics to meet the specific requirements of each treatment. However, it is important to consider that PLGA degradation can generate local acidic byproducts that, if not properly formulated, can accumulate in tissues and potentially compromise their biocompatibility [43] PEI, a cationic polymer, was used for its well-established ability to form stable electrostatic complexes with negatively charged molecules, such as siRNA. This property enhances cellular internalization and ensures efficient gene delivery, making PEI an effective carrier for nucleic acids. However, its cationic nature also introduces a risk of cytotoxicity at higher concentrations, requiring careful optimization to balance transfection efficiency with biological safety. Finally, ionic liquids have been used as surface coatings for nanoparticles to further improve their stability, promote selective accumulation in target tissues, and enhance cellular uptake. Choosing the right ILs is crucial, as it directly influences the toxic profile and bioavailability of nanoparticles. Synthetic methods were chosen based on the properties of each polymer system. For PEI-based nanoparticles, nanoprecipitation was used, as this technique reliably produces uniform, size-controlled, positively charged particles, ideal for complexation with siRNA. Nanoprecipitation is simple, reproducible, and compatible with delicate molecules, although it may be less efficient for encapsulating highly hydrophilic compounds and requires careful removal of residual solvents. For ionic liquid-coated nanoparticles, microemulsion was chosen for its ability to finely control particle size, achieve high encapsulation efficiency, and design a tunable release profile for therapeutic cargo. While highly effective, this method also presents challenges, including the need for surfactants, complex purification procedures, and limited scalability, which must be considered when planning for large-scale production [48]By integrating the choice of polymer with the most suitable preparation method, these nanoparticle systems achieve a balance between stability, efficacy, and targeted release, providing a versatile platform for the therapeutic delivery of nucleic acids such as siRNA.

1.10 Ionic Liquids

In recent years, ionic liquids (ILs) have attracted growing interest in the field of nanomedicine due to their versatility and unique chemical and physical properties that distinguish them from traditional solvents. These salts consist entirely of cations and anions and remain liquid at room temperature or at low temperatures, thanks to their low lattice energy and charge delocalization [49]. ILs exhibit low volatility, high thermal and chemical stability, a wide electrochemical window, tunable viscosity, and a marked ability to solubilize both hydrophilic and hydrophobic compounds. These properties make them ideal materials for the synthesis, stabilization, and functionalization of nanoparticles, where they can act as solvents, cosolvents, coating agents, or structural components of the nanostructured system. In the biomedical field, the use of ILs improves colloidal stability, regulates drug release, protects nucleic acids from degradation, and increases interaction with cell membranes, while maintaining good biocompatibility [49] (**Table 6**).

Type	Representative Ions / Examples	Main Physicochemical Properties	Typical Applications
CATIONS			
Imidazolium	$[BMIM]^+$ (1-butyl-3-methylimidazolium), $[HMIM]^+$, $[OMIM]^+$	High thermal and chemical stability, π–π interactions, tunable polarity and viscosity	Nanoparticle synthesis and coating, gene delivery, catalysis
Pyridinium	$[C_4Py]^+$, $[C_6Py]^+$	Aromatic planar structure, charge delocalization	Electrochemical systems, conductive nanomaterials
Pyrrolidinium	$[PYR_{14}]^+$, $[PYR_{13}]^+$	Saturated ring, low viscosity, high robustness	Ionic conductors, energy storage materials
Cholinium	$[Ch]^+$ (choline-based)	Biocompatible, biodegradable, hydrophilic	Biomedical and environmental applications
Tetraalkylammonium / phosphonium	$[N_4R_4]^+$, $[P_4R_4]^+$	Adjustable hydrophobicity, tunable chemical behavior	Catalysis, functional surface coatings
ANIONS			
Hexafluorophosphate (PF_6^-)	—	Hydrophobic, thermally stable	Nanoparticle stabilization, electrochemistry
Tetrafluoroborate (BF_4^-)	—	Low viscosity, high ionic mobility	Controlled nanoparticle growth
Bis(trifluoromethylsulfonyl)imide (NTf_2^-)	—	Bulky, hydrophobic, reduces melting point and viscosity	Dispersion and colloidal stability
Chloride (Cl^-), Acetate (CH_3COO^-)	—	Hydrophilic, suitable for biopolymer solubilization	Biomolecule processing, bioactive systems
Trifluoromethanesulfonate (OTf^-)	—	Chemically stable, hydrophobic	Surface functionalization, hybrid nanostructures

Table 6. Classification and Main Characteristics of Ionic Liquids. The table illustrates the chemical diversity of cations and anions used in the synthesis of nanomaterials, highlighting how the modulation of parameters such as thermal stability, hydrophobicity and biocompatibility allows for the optimization of catalysis, gene delivery and colloidal stabilization processes

Among the various classes of ionic liquids, imidazolium-based ones are undoubtedly the most studied and applied in the biomedical field, thanks to their combination of chemical stability, structural modularity, and ability to interact with biomolecules. They are predominantly derived from the 1-

alkyl-3-methylimidazolium cation, in which the length of the alkyl chain modulates key parameters such as polarity, viscosity, and hydrophobicity, influencing their affinity for cell membranes and proteins. The planar aromatic structure of the imidazole ring allows π–π interactions with other aromatic molecules, while the cation's positive charge favors electrostatic interactions with anionic species, such as membrane phospholipids and nucleic acids (DNA and siRNA), facilitating their condensation and protecting them from enzymatic degradation [50]. Numerous studies have demonstrated that imidazolium salts possess marked intrinsic biological activity, including antimicrobial, antibiofilm, and antitumor effects. In particular, their antitumor activity has been attributed to complementary mechanisms, such as altered mitochondrial function with the induction of oxidative stress and apoptosis, direct interaction with DNA through binding and intercalation, and impaired plasma membrane integrity due to their amphiphilic and cationic nature. Structure-activity relationship studies have also shown that benzyl-substituted derivatives exhibit increased cytotoxicity, attributable to increased hydrophobicity and the presence of an aromatic group capable of strengthening both interaction with lipid membranes and binding to nucleic acids [51]. Although these properties make imidazolium salts highly attractive bioactive molecules, their direct use may be limited by dose-dependent cytotoxic effects. In this context, the use of imidazolium salts as functional coatings on polymeric nanoparticles, such as those based on PLGA or PEG-PLGA, represents an effective strategy to exploit their benefits while reducing their undesirable effects. When integrated as a coating, imidazole cations form an ionic shell around the polymer core, providing colloidal stability through a combination of electrostatic repulsion and steric barrier, even under complex physiological conditions and in the presence of serum proteins [51,52]. Furthermore, the positive charge of the imidazole cation enables electrostatic binding to DNA or siRNA, protecting the therapeutic cargo from nuclease degradation and promoting its cellular internalization, primarily through clathrin-mediated endocytosis. Inside the cell, the controlled interaction between ionic liquid, polymer, and nucleic acid allows for modulated release of the cargo, the kinetics of which can be regulated through appropriate design of the ionic composition. At the same time, the cationic nature of ILs promotes adhesion to the cell surface and interaction with negatively charged membranes, improving the intracellular bioavailability of the active ingredient [53].

Another crucial factor is the choice of anion associated with the imidazole cation. Bulky and weakly coordinating anions, such as NTf_2^-, are generally associated with greater colloidal stability and reduced toxicity, while more hydrophobic or strongly coordinating anions, such as PF_6^-, can increase the overall hydrophobicity of the system, improving some of its physicochemical properties, but at the expense of biocompatibility. Rational selection of the cation-anion pair therefore allows for fine-tuning the properties of nanoparticles, maximizing therapeutic efficacy while maintaining an adequate safety profile. Overall, these findings support the idea that imidazolium salts, while possessing intrinsic biological activity, can be repurposed more safely and effectively as functional components of nanostructured systems. In this configuration, they act not only as stabilizing elements and carriers for therapeutic molecules, but also as modulators of nanoparticle-cell interactions, offering new opportunities for the development of innovative and less aggressive anticancer strategies [54] **(Figure 8).**

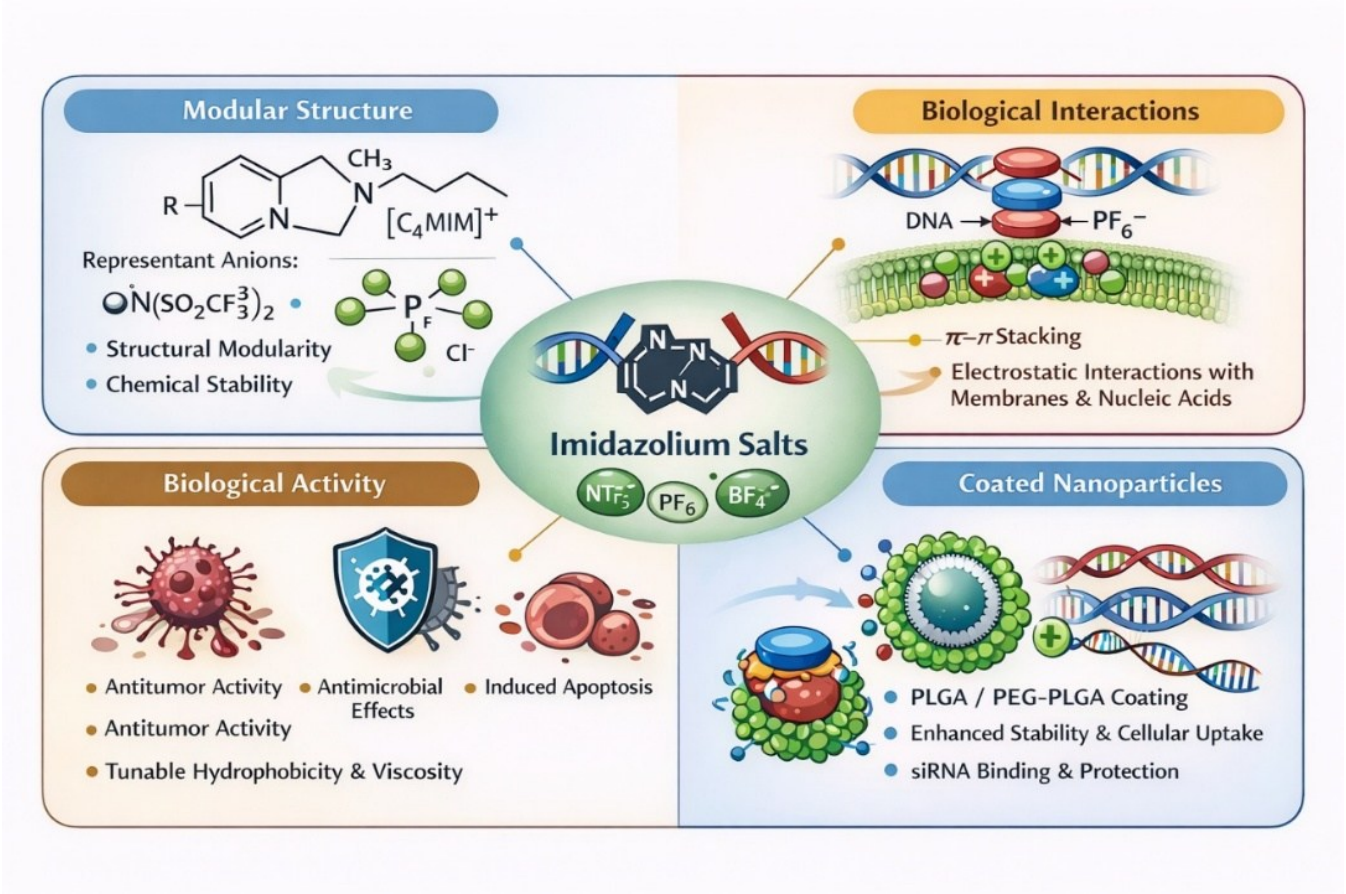

Figure 8. Multifunctional properties and biomedical applications of imidazole salts. The image illustrates the structural modularity of these ionic liquids, highlighting their ability to stabilize nucleic acids and membranes through electrostatic interactions and pi-pi stacking. Their use in coating polymeric nanoparticles (PLGA/PEG) for drug delivery and their intrinsic biological properties, including strong antimicrobial and anticancer activities, are also highlighted.

1.11 Polyethylenimine

Polyethylenimine (PEI) is a cationic polymer widely used as a nonviral vector for nucleic acid delivery, thanks to its high density of positive charges that allows it to form stable complexes (polyplexes) with DNA, mRNA, or siRNA The polymer exists in two main forms: branched (bPEI) and linear (lPEI). The latter consists of repeating ethylene-imine units arranged in a linear chain, a characteristic that provides a more uniform distribution of charges than the branched form, resulting in lower cytotoxicity and greater transfection efficiency [55]. A key property of linear PEI is the "proton sponge" effect, whereby secondary amines along the polymer backbone can buffer endosomal acidification. Protonation of these groups induces the influx of ions and water into endosomes, causing osmotic swelling, membrane disruption, and release of the gene cargo into the cytoplasm. Although the exact molecular mechanism of endosomal escape is still under investigation, numerous experimental lines of evidence confirm the effectiveness of linear PEI in promoting the intracellular entry of siRNA and plasmid DNA [56]. The transfection efficiency of linear PEI depends strongly on its molecular weight and the N/P ratio, i.e., the ratio of PEI amino groups to nucleic acid phosphate groups. A molecular weight of approximately 25 kDa is considered the gold standard, as it represents an optimal compromise between condensation capacity, protection from enzymatic degradation, cellular internalization, and toxicity. At this molecular weight, linear PEI is able to form stable nanoparticle polyplexes, typically between 50 and 150 nm, which effectively condense siRNA, facilitate interaction with the cell membrane, and promote endosomal escape. In recent years, hybrid systems have been developed in which linear PEI is combined with biodegradable polymers such as PLGA or PEG-PLGA. In these systems, lPEI acts as an electrostatic modulator, enhancing nucleic acid complexation, cellular internalization, and controlled intracellular release, while the biodegradable component increases biocompatibility, circulation time, and reduces acute toxicity [57]. Despite these advantages, dose-dependent cytotoxicity remains a significant limitation. The high density of cationic charges can damage cell membranes and induce oxidative stress, apoptosis, and inflammatory responses [57,58]. To mitigate these effects, several chemical modification strategies have been developed, including PEGylation, which shields positive charges and reduces interaction with serum proteins; the insertion of hydrophobic or aromatic groups, such as tyrosine, to increase complex stability and facilitate endosomal escape; and the synthesis of degradable derivatives that degrade intracellularly, reducing toxicity without compromising transfection efficiency [59].

In addition, functionalizing PEI-based polyplexes with specific ligands, such as peptides or antibodies, can increase cell specificity and further improve therapeutic efficacy, making linear PEI a versatile platform for targeted gene therapy. In summary, linear PEI represents one of the most

studied and used materials for the non-viral delivery of siRNA and DNA, thanks to its ability to form stable complexes, promote endosomal escape, and integrate into advanced nanostructured systems, constituting a fundamental benchmark in the development of safe and efficient vectors [60].

1.12 Three-dimensional models for the study of nanoparticle-mediated gene delivery

Two-dimensional (2D) cell cultures have long been a standard tool in *in vitro* studies; however, they exhibit significant limitations in accurately recapitulating the complexity of the in vivo tumor microenvironment. In 2D systems, cells grow in a monolayer on rigid surfaces, lacking the three-dimensional cell-cell and cell-extracellular matrix interactions that strongly influence the migration, proliferation, and therapeutic response of real tumors. This can lead to data that are not predictive of actual biological behavior, particularly for the penetration and release of therapeutic agents such as siRNA 3D cell models, such as spheroids, organoids, or co-cultures in hydrogel matrices, better reproduce the architecture, composition, and oxygen/nutrient conditions that characterize solid tissues, thus providing a more physiologically relevant context for studying cellular behavior and the efficacy of new therapeutic strategies. In particular, 3D models allow for the evaluation of the efficacy, penetration, and accumulation of nanoparticles within dense cell masses, which cannot be captured in monolayer models.

Numerous studies have therefore investigated nanoparticle-based delivery systems in 3D culture models for the transport of therapeutic agents and nucleic acids, as summarized in **Table 7**. Compared with conventional two-dimensional (2D) cultures, polymeric nanoparticles exhibit markedly different penetration and internalization behaviors in spheroid models, highlighting the importance of 3D systems for evaluating nanoparticle transport and cellular uptake. Moreover, the use of polyethylenimine (PEI)-coated nanoparticles has enabled effective delivery of siRNA and plasmid DNA in 3D co-culture models, supporting the relevance of three-dimensional platforms for assessing gene delivery efficacy in tumor-relevant contexts [61].These findings highlight how the use of 3D models is critical for the development and validation of gene delivery vectors, helping to overcome the limitations of 2D assays and bringing experimental conditions closer to those encountered in tumor tissues in vivo .

Nanoparticles System	siRNA Loading Strategy	3D Cancer Model	Key Observations in 3D Cultures	Comparison with 2D Cultures	Endosomal Escape / Gene Silencing Efficiency
Polymeric nanoparticles (e.g., PLGA-based)	Physical encapsulation or adsorption with cationic modifiers	Tumor spheroids	Limited penetration into spheroid core; heterogeneous siRNA distribution; uptake mainly in peripheral cells	Uniform uptake and higher apparent silencing in 2D	Poor endosomal escape without functionalization; low gene silencing efficiency
Surface-modified polymeric nanoparticles	Electrostatic complexation with siRNA	Cancer spheroids	Improved penetration and internalization depending on surface charge and ligand density	siRNA efficacy often overestimated in 2D systems	Moderate gene silencing when pH-responsive or cationic components are included
PEI-coated polymeric nanoparticles	Electrostatic complexation	3D tumor co-cultures (tumor–stromal)	Efficient cellular uptake; penetration limited by spheroid density	Higher transfection efficiency but reduced predictability in 2D	Efficient endosomal escape via proton sponge effect; significant target gene knockdown
PEI-based polyplexes	Direct electrostatic condensation	Tumor spheroids	siRNA delivery predominantly to outer cell layers	Homogeneous silencing in 2D	Strong endosomal escape; spatially restricted gene silencing in 3D
Lipid–polymer hybrid nanoparticles	Encapsulation within polymer core and lipid shell	Cancer spheroids	Enhanced stability and deeper penetration compared with polymer-only systems	Minimal transport barriers in 2D	Improved endosomal escape; higher and more uniform gene silencing
Targeted polymeric nanoparticles	Ligand-mediated complexation or encapsulation	Receptor-expressing tumor spheroids	Increased specificity and uptake in target-positive cells; heterogeneous penetration	Targeting effects less evident in 2D	Enhanced gene silencing in receptor-expressing regions

Table 7. Application of siRNA-loaded nanoparticle systems in 3D cancer cell culture models

2. Aim of the study

The overall aim of this PhD thesis is the rational design, physicochemical characterization, and *in vitro* biological evaluation of innovative poly(lactic-co-glycolic acid) (PLGA)–based nanocarriers for the safe and efficient delivery of anti-GOLPH3 small interfering RNA (siRNA) in prostate cancer cells. To address this objective, the work focuses on two distinct yet complementary polymer functionalization strategies: (i) surface modification of PLGA nanoparticles with imidazolium-based ionic liquids (PLGA-ILs) and (ii) conjugation of PLGA with polyethylenimine (LGIP). These approaches are investigated as tools to modulate nanoparticle surface properties and their interactions with biological systems.

Within this framework, the study aims to elucidate how nanoparticle surface chemistry regulated by the alkyl chain length of imidazolium-based ionic liquids or by PEI conjugation affects key biological and functional parameters, including biocompatibility, cellular uptake, endocytic internalization pathways, intracellular trafficking, and the efficacy of siRNA-mediated gene silencing. Imidazolium-based ionic liquids are initially selected and evaluated as independent functional entities in order to identify optimal physicochemical and biological profiles. The most promising ionic liquids are subsequently employed as surface coatings for PLGA nanoparticles, with the objective of enhancing surface charge, colloidal stability, and interactions with negatively charged biomolecules such as siRNA.

In parallel, the thesis involves the synthesis and comprehensive characterization of PLGA-ILs and LGIP nanoparticles, including the assessment of particle size, morphology, surface charge, colloidal stability, and structural integrity, to ensure their suitability for biomedical and gene delivery applications. Particular attention is devoted to understanding how variations in ionic liquid alkyl chain length or PEI conjugation influence nanoparticle behavior in complex biological environments.

From a biological standpoint, the work systematically evaluates the *in vitro* biocompatibility of ionic liquids, PLGA-ILs nanoparticles, and LGIP nanoparticles in both non-tumorigenic and malignant prostate cell lines. This evaluation includes analyses of cytotoxicity, oxidative stress, apoptosis induction, and effects on cell migration, with the aim of defining safe and effective concentration ranges for nanocarrier-mediated gene delivery. Furthermore, cellular uptake kinetics and intracellular localization are investigated to identify the predominant endocytic pathways involved in nanoparticle internalization. Through the use of selective pharmacological inhibitors, particularly those targeting clathrin-mediated endocytosis and macropinocytosis the study examines how nanoparticles surface functionalization and concentration influence cellular entry routes and intracellular fate, which are critical determinants of siRNA delivery efficiency.

Finally, the thesis assesses siRNA loading capacity, release profiles, and functional gene silencing efficacy, using GOLPH3 as a therapeutically relevant target in prostate cancer cells. By correlating the physicochemical properties of the nanocarriers with cellular uptake mechanisms, intracellular trafficking pathways, and gene silencing outcomes, this work aims to define rational design principles for next-generation PLGA-based siRNA delivery systems. Overall, this PhD thesis seeks to provide mechanistic insight into how ionic liquid functionalization and polymer conjugation strategies can be exploited to optimize nanoparticle–cell interactions, improve endocytic routing, and enhance siRNA-mediated gene silencing, thereby contributing to the development of safer and more effective non-viral gene delivery platforms for cancer therapy.

3. Materials and Methods

3.1 Preparation of Imidazolium salts.

All ionic liquids (ILs) were dissolved in dimethyl sulfoxide (DMSO) to prepare stock solutions and subsequently diluted in Dulbecco's Modified Eagle Medium (DMEM) to obtain working concentrations ranging from 0.1 to 10 µg/mL. The final DMSO concentration in cell culture experiments did not exceed 0.1% (v/v). 1-Decyl-3-methylimidazolium chloride (C_{10}MImCl) and 1,3-didecyl-2-methylimidazolium chloride ((C_{10})$_2$MImCl) were purchased from Sigma-Aldrich and used as received. All other imidazolium salts were synthesized according to previously reported procedures in literature. In particular: 1-Dodecyl-3-methylimidazolium chloride (C_{12}MImCl) was prepared according to literature [62]; 1-Methyl-3-tetradecylimidazolium chloride (C_{14}MImCl) [62]; 1-Hexadecyl-3-methylimidazolium chloride (C_{16}MImCl) [63]; 1-Methyl-3-octadecylimidazolium chloride (C_{18}MImCl) [64]; 1-Hexadecyl-3-methylimidazolium methanesulfonate (C_{16}MImMeS) and 1-Methyl-3-octadecylimidazolium methanesulfonate (C_{18}MImMeS)[65]; 1-Hexadecyl-3-(2-hydroxyethyl) imidazolium chloride (C_{16}C2OHImCl) [66]; 1-Benzyl-3-hexadecylimidazolium chloride (C_{16}BnImCl) and 1-Benzyl-3-octadecylimidazolium chloride (C_{18}BnImCl) [67]; 1-Hexadecylimidazole (C_{16}Im); 1-Octadecylimidazole (C_{18}Im) [68,69] ; 1-Hexadecylmethanesulfonate (C_{16}MeS) [70]; 1-Octadecylmethanesulfonate (C_{18}MeS) [70,71]. C_{16}Im, C_{18}Im, C_{16}MeS, and C_{18}MeS were used as intermediates for the preparation of C_{16}MImMeS, C_{18}MImMeS, C_{16}BnImCl, and C_{18}BnImCl via quaternization reactions. C_{18}BnImCl was synthesized by reacting 1-octadecylimidazole (1.00 mmol, 1.00 equiv.) with benzyl chloride (2.00 mmol, 2.00 equiv.) under reflux at 110 °C for 24 h, followed by recrystallization from ethyl acetate, affording a pale white solid in 76% yield C_{18}MImMeS was obtained following the literature procedure reported , affording a white solid in 70% yield. All synthesized compounds were characterized by ^{1}H and ^{13}C nuclear magnetic resonance spectroscopy, attenuated total reflection Fourier transform infrared spectroscopy (ATR-FTIR, 4000–750 cm^{-1}), and high-resolution mass spectrometry. Spectral data were consistent with previously reported values.

3.2 Synthesis of PLGA-ILs nanoparticles

PLGA-ILs nanosystems were prepared using PLGA (Sigma-Aldrich) nanoparticles functionalized with imidazolium-based ionic liquids (Sigma-Aldrich), specifically C_{16}MImCl and C_{10}MImCl. The nanoformulations were prepared using an oil-in-water (O/W) microemulsion method. Briefly, 60 mg

of poly(lactic-co-glycolic acid) (PLGA) were completely dissolved in 3 mL of chloroform and subsequently added dropwise to an aqueous solution containing 50 mg of either 1-hexadecyl-3-methylimidazolium chloride (C_{16}MImCl) or 1-decyl-3-methylimidazolium chloride (C_{10}MImCl) under continuous homogenization. Owing to their amphiphilic nature, the ionic liquids interact with the hydrophobic PLGA chains through van der Waals interactions, while their hydrophilic moieties remain exposed to the aqueous phase, thereby promoting colloidal stabilization of the nanoparticles. Subsequent overnight evaporation of chloroform led to the formation of PLGA–C16 and PLGA–C10 nanoparticles. For cellular internalization studies using confocal microscopy and flow cytometry, the fluorescent probe dichlorofluorescein (DCF, Sigma-Aldrich) was incorporated into the polymer core using the same microemulsion process. In particular for both PLGA-ILs and LGIP nanoparticles, DCF was incorporated into the polymer core by adding the dye to the organic phase containing PLGA prior to the oil-in-water microemulsion and nanoprecipitation process. This approach allows for the integration of the fluorescent probe within the polymer matrix during solvent evaporation and particles solidification.After formation, the suspensions were purified by centrifugation to remove the unencapsulated dye. The hydrodynamic diameter, PDI, and ζ potential were measured to evaluate the physicochemical properties of the loaded nanoparticles. The individual ionic liquids, C_{16}MImCl and C_{10}MImCl, were first characterized by NMR to confirm their chemical structure before being incorporated into the PLGA nanoparticles. Nuclear magnetic resonance (NMR) spectra were recorded on a Bruker (400 MHz) equipment at ambient temperature. The chemical shifts are given in parts per million (ppm) and referenced to the residual solvent signal ($CDCl_3$ = 7.26 (^{1}H), 77.16 (^{13}C); DMSO-d6 = 2.50 (^{1}H), 39.52 (^{13}C)).

3.3 Synthesis of LGlP nanoparticles

LGlP NPs based on PLGA 75:25 (66–107 kDa) and linear PEI (4 kDa) were synthesized as follows. PLGA (1 eq, 0.1 mM) was activated in DMSO (Acros Organics) using EDC (Fluka) (10 eq) and NHS (Sigma-Aldrich) (10 eq) under stirring at room temperature for 4 h. Subsequently, PEI (4 kDa, Sigma-Aldrich) (1 eq), previously dissolved in DMSO and supplemented with Et_3N (20 µL), was added dropwise to the activated PLGA solution and allowed to react under stirring for 20 h. The reaction mixture was then purified by dialysis (MWCO 14 kDa) against deionized water for 48 h and lyophilized. The final LGlP product was characterized by ^{1}H-NMR in DMSO-d_6 and by FTIR-ATR.

3.4 Physicochemical and morphological characterization of nanoparticles

For all prepared nanoparticles (PLGA-ILs and LGlP NPs), the colloidal properties hydrodynamic diameter (Dh), polydispersity index (PDI) and zeta potential (ζ) were assessed by Dynamic Light

Scattering (DLS). DLS measurements were performed using a Zetasizer Nano Z (Malvern Instruments Ltd., UK) operating in backscattering mode at 173° with a He–Ne laser (λ = 532 nm) at 25 °C. Hydrodynamic diameter, PDI and zeta potential values were reported as the mean ± standard deviation (SD) of three independent measurements from three different batches (n = 9).

3.5 Transmission electron microscopy

Size distribution of PLGA-ILs and LGIP NPs were examined by a transmission electron microscope (TEM, JEM 2100 HT), operating at an electron voltage of 120 kV. The samples were prepared by drop-casting 30 µL of diluted solution on a carbon-coated copper grid, which was then dried at RT. The diameters and size distributions from the TEM images were analyzed using ImageJ software. The average size and the SD have been calculated for each sample.

3.6 In *vitro* cell culture

DU145 were cultured in Dulbecco's Modified Eagle's Medium High Glucose (DMEM) and PNT-2 in Roswell Park Memorial Institute (RPMI) 1640 Medium with L-Glutamine (Sigma-Aldrich, Milan, Italy); both media were supplemented with 10% fetal bovine serum of South American origin (Microgem, Italy), antibiotic solution (streptomycin) 100 µg/mL and penicillin 100 U/mL (Sigma-Aldrich, Italy) in a 95% humidified atmosphere containing 5% CO_2 at 37 °C. For the co-culture experiments, DU145 tumor cells were cultured in high-glucose DMEM and 2% fetal bovine serum. Human endothelial cells (HUVECs) were cultured in Endothelial Cell Growth Medium with 2% FBS, conditions necessary to ensure proliferation and maintenance of endothelial morphology. For three-dimensional cultures, PhenoDrive-Y material was used, reconstituted in a solution of ethanol:water (75:25, v/v). 200 µL of the solution was distributed on the bottom of 24-well plates and left to dry at room temperature for 3 hours. Before cell seeding, the coated wells were sterilized by exposure to UV light for 1 hour, thus creating a suitable surface for the formation of spheroids and stable 3D cultures.

3.7 Cell viability and oxidative stress

Alamar blue assay: PNT2 and DU145 cells were seeded in 96-well plates at a density of 5,000 cells/well in RPMI and DMEM, respectively. After 24 h, nanoformulations of PLGA-ILs NPs and LGIP NPs were added at the following concentrations: 150 ng/mL; 500 ng/mL; 5 µg/mL; 10 µg/mL; 20 µg/mL; 25 µg/mL; 50 µg/mL; 100 µg/mL. Cells were incubated with NPs for 72 h. Alamar Blue 10 v/v% solution (Life Technologies, Italy) was added to each well (200 µL) and incubated for 4 h at 37 °C. The conversion of resazurin to resorufin by mitochondrial reductase was measured as optical density using a spectrophotometer (PerkinElmer VICTOR™ X3 Multimode Reader) at wavelengths of 570 and 600 nm. All experiments were performed in at least triplicate cultures and repeated three times. The biocompatibility of ILs was assessed using the CCK-8 cytotoxicity assay. PNT2 and DU145 were seeded in 96-well plates, along with control wells containing culture medium only (5,000/well). At 80% cell confluence, cultures were treated with ILs at different concentrations (0.025 to 2.0 µg/mL) and incubated for 24 hours. Cell viability was then assessed using the CCK-8 assay following the manufacturer's instructions. Briefly, 10 µL of CCK-8 reagent was added per well, and the plates were incubated for 4 hours at 37°C. Optical density (OD) was measured at 450 nm using a Victor X3™ microplate reader (Perkin Elmer, Milan, Italy). All experiments were performed in triplicate and results are expressed as mean ± SD of the percentage viability compared to untreated controls. In contrast, for DU145–HUVEC cocultures, 25,000/60,000 cells were seeded in 24 wells. Twenty-four hours after treatment with PLGA-C16 NPs and PLGA-C10 NPs at concentrations of 150 and 500 ng/mL, the supernatants were collected and used for the LDH cytotoxicity assay (ROCHE Cytotoxicity Detection Kit) and the protein assay (Pierce™ BCA, Thermo Fisher Scientific), following the manufacturer's instructions. A Triton X-100-treated sample served as a positive control (maximum LDH release), while untreated cells served as a negative control. The absorbance of the LDH assay was read at 492 nm, while that of the BCA protein assay was read at 660 nm. The LDH values were then normalized to the protein content obtained for each sample and expressed as specific enzyme units.

Live/dead assay: PNT2 and DU145 cells were seeded in 96-well plates and exposed for 24 hours to 0.1 µg/mL, 0.5 µg/mL, and 1 µg/mL of C10MImCl, C16MImCl, and C16BnImCl. Live cells were stained with the membrane-permeable dye Cytotrace (1µg), which penetrates intact cells and is hydrolyzed by intracellular esterases, producing a green fluorescence signal. In contrast, dead cells were labeled with propidium iodide (PI, 1 µg/mL), which cannot cross intact membranes but readily penetrate cells with compromised membranes. Once inside, PI binds to DNA and emits red fluorescence, which can be detected using JuliStage TimeRecorder microscopy.

ROS assay: Intracellular reactive oxygen species (ROS) were quantified using the DCFH-DA fluorescent probe at a final concentration of 20 μM. 7.000 cells were seeded in 96-well plates and, after adhesion, were treated with 0.1 μg/mL, 0.5 μg/mL and 1 μg/mL of C_{10}MImCl, C_{16}MImCl and C_{16}BnImCl for 24 h and then incubated with the probe to allow intracellular de-esterification and subsequent ROS-dependent oxidation. Fluorescence intensity of the oxidized product (DCF) was measured using a plate reader equipped for excitation/emission in the green channel. Fe^{2+}/H_2O_2 was used as a positive control for ROS generation, while untreated cells served as baseline controls.

3.8 3D Spheroid formation and treatment assay

To generate three-dimensional (3D) spheroids of DU145 cells, Matrigel (Corning, USA) was used as a matrix to mimic the extracellular environment. Prior to use, Matrigel was thawed overnight at 4 °C according to the manufacturer's instructions. A volume of 50 μL/cm^2 of diluted Matrigel was dispensed into the wells of a 96-well plate. The plate was then incubated at 37 °C in a humidified atmosphere containing 5% CO_2 for 30 minutes to allow Matrigel polymerization, thereby forming a biologically active matrix resembling the basement membrane. After polymerization, a cell suspension of DU145 (5,000 cells/cm^2, respectively) was seeded onto the Matrigel-coated wells. The cells were cultured for 7 days under standard conditions, with the culture medium replaced every 2 days. During spheroid formation, spheroids were monitored daily under an inverted microscope. At day 7, spheroids were treated with 1 μg/mL of the compounds C_{10}MImCl, C_{16}MImCl, and C_{16}BnCl for 72 hours. Control spheroids were maintained in their respective culture medium. Following treatment, the spheroids were placed in the JuLi™ Stage Real-Time Cell History Recorder (NanoEnTek, Korea) for imaging acquisition (10X objective). To evaluate cell viability after treatment, an Alamar Blue (Invitrogen, Italy) assay was performed. Cells were incubated with the Alamar Blue reagent (1:10 dilution) for 4 hours, and absorbance was measured at 570 nm. All experiments were carried out in technical and biological triplicates.

3.9 Hematoxylin and Eosin (H&E) staining

This staining was used to evaluate the morphology of DU145–HUVEC cocultures treated with PLGA-C16 and PLGA-C10 nanoparticles at concentrations of 150 and 500 ng/mL, in order to compare any morphological changes and variations in cell density and integrity induced by the different alkyl lengths of the ionic liquids. After 24 hours of treatment, the cells were fixed with 4% paraformaldehyde (PFA, Sigma-Aldrich) for 15 minutes at room temperature and then washed with

PBS. The samples were stained with hematoxylin (abcam) for 5 minutes and counterstained with eosin (abcam) for 2 minutes. The samples were subsequently observed under a light microscope to evaluate cellular morphology, distribution, and organization, comparing the treated conditions with the controls.

3.10 Immunofluorescence analysis

To assess the internalization capacity of the nanoparticles, cells were seeded onto 12-mm glass coverslips placed in 24-well plates. After 24 h, cells were treated with DCF-loaded PLGA-ILs and LGIP nanoparticles at concentrations of 150 ng/mL, 500 ng/mL, and 10 μg/mL, and incubated for different time intervals (6, 24, 48, and 72 h). Subsequently, the cells were fixed in 10% neutral buffered formalin for 2 hours at room temperature, washed with PBS and permeabilized with 0.1% Triton X-100 in PBS. After blocking with 2% BSA in PBS for 45 minutes, the cells were incubated with CellMask Deep Red Plasma Membrane Stain (Invitrogen™) 1:1000 for 30 minutes, mounted with Fluoromount (SouthernBiotech) and analyzed by confocal microscopy (Leica DMi8, HC PL APO CS2 63x/1.40 OIL objective). For GOLPH3 silencing, after 48 and 72 hours, cells on slides treated with all three anti-GOLPH3 siRNA binding nanosystems and their respective Lipofectamine-treated controls were fixed in formalin for 2 h and incubated overnight at 4°C with anti-GOLPH3/MIDAS antibody (Abcam) 1:400. The next day, cells were incubated for 30 min with CellMask Orange Plasma Membrane Stain 1:1000 and Goat anti-Rabbit IgG (H+L) DyLight™ 488 secondary antibody 1:200, and GOLPH3 protein reduction was analyzed by fluorescence microscopy (Leica DMi8, HC PL FLUOTAR 100x/1.32 OIL PH3 objective).

3.11 Flow cytometry analysis

To evaluate the biocompatibility of the ILs, apoptosis was assessed by Annexin V–FITC and propidium iodide staining, followed by flow cytometric analysis using a MACSQuant flow cytometer. DU145 and PNT2 cells were treated for 24 hours with 0.1, 0.5, and 1 μg/mL of C10MImCl, C16MImCl, and C16BnImCl. After treatment, cells (1 × 10^6) were harvested, washed in binding buffer, and incubated with Annexin V–FITC to detect phosphatidylserine externalization, while PI was used to identify loss of membrane integrity. The analysis was performed immediately on the MACSQuant flow cytometer using the appropriate channels: FITC was excited at 488 nm with emission collected at 518 nm (green channel), while PI was excited at 535 nm with emission collected at 617 nm (red channel). Data were processed using MACSQuantify software. The internalization of

PLGA-ILs and LGIP nanoparticles was also evaluated by flow cytometry. Briefly, DU145 cells were seeded in 6-well plates at a density of 1×10^5 cells per well in complete culture medium and incubated for 24 h prior to treatment. Nanoparticles were then added at concentrations of 150 ng/mL, 500 ng/mL, 10 μg/mL, and 50 μg/mL, and cells were incubated for 6, 24, and 72 h. After incubation, the cells were treated with trypsin and centrifuged at 1200 rpm for 5 minutes at 25°C. The cell pellet was washed twice with 1X PBS. Fluorescence associated with DCF incorporated into the internalized nanoparticles was detected using a MACSQuant® Analyzer 16 flow cytometer (Miltenyi Biotec), with excitation at 525 nm and emission at 550 nm. At least 10,000 cells were analyzed, excluding cellular debris by gating the plot area. To identify the endocytic pathway involved in nanoparticle internalization, Pitstop-2 (Sigma-Aldrich), an inhibitor of clathrin-mediated endocytosis, and Amiloride (Sigma-Aldrich), an inhibitor of macropinocytosis, were used. DU145 cells were seeded in 6-well plates at 100,000 cells/well in complete medium and incubated for 24 hours before treatment. PLGA-ILs and LGIP NPs were added at 10 μg/mL and 50 μg/mL for 72 hours, in the presence of Pitstop 2 (1 nM) or Amiloride (10 μM) for the entire treatment duration. Samples containing only PLGA-ILs and LGIP NPs without inhibitors were used as controls. After treatment, cells were separated with 0.25% trypsin-EDTA (Sigma-Aldrich), centrifuged for 5 minutes at 1200 rpm with acceleration and deceleration set to 9, and washed three times with 1X PBS before analysis.

3.12 Preparation of PLGA-ILs and LGIP/anti-GOLPH3 siRNA complexes

The nanoparticles were conjugated with a pool of anti-GOLPH3 siRNA (Merck, Milan, Italy), containing the following sequences (**Table 8**). The polymer/siRNA complexes were prepared by mixing a fixed amount of siRNA (0.614 μg, corresponding to 50 nM) with 3.21 μg of PLGA-ILs. For LGIP formulations, two polymer/siRNA weight ratios were tested using 3 μg (LGIP-1) and 30 μg (LGIP-10) of polymer. The mixtures were incubated for 3 hours at room temperature to allow nanoparticles/siRNA electrostatic complexes. The release of siRNA from the nanoparticles was assessed over time by incubating the complexes in distilled water under constant agitation at room temperature for 2, 24, and 72 hours. After each time point, 10 μL of sample was collected for the Picogreen assay, which allows for the sensitive detection of nucleic acids. Fluorescence was measured using a plate reader with excitation at 480 nm and emission at 520 nm. The selection of nanoparticles/siRNA ratios was based on a mass ratio (w/w) approach rather than theoretical N/P calculations. This strategy is commonly adopted in polymeric nanoparticle-based siRNA delivery systems, particularly when complexation occurs at the surface of preformed nanoparticles rather than

through condensation with freely accessible cationic polymer chains [72]. In the present PLGA-ILs and LGIP nanosystem, positive charges are distributed at the nanoparticles surfaceand their effective accessibility cannot be accurately predicted using conventional N/P stoichiometric calculations. Therefore, empirical optimization based on weight ratios was considered more appropriate. An initial screening was performed by testing nanoparticles/siRNA mass ratios of 0.614 µg/ 4 µg; 0.614 µg/ 10 µg; 614 µg/ 40 µg , and in order to identify the minimum amount of carrier required for efficient siRNA binding and colloidal stability. Complex formation and release behavior were evaluated using the PicoGreen assay. Among the tested conditions, the 0.614 µg/4 µg ratio provided efficient siRNA complexation while maintaining controlled release kinetics. The improved performance observed at the 1:1 ratio may be attributed to an optimal surface charge balance, ensuring sufficient electrostatic interaction for stable siRNA adsorption without excessive carrier excess. Higher nanoparticle excess (614 µg/10 µg and 614 µg/40 µg) did not significantly enhance binding efficiency and may lead to excessive surface charge density, potentially affecting release kinetics and biological performance. Therefore, the 0.614 µg/4 µg ratio was selected for subsequent experiments as it represents the minimal effective carrier amount ensuring stable complex formation and suitable release behavior [72].

siRNA anti-GOLPH3	Forward Primer	Reverse Primer
#1 GOLPH3	AAAUGAUGUGUAACCCU CGCGGUCC	GGACCGCGAGGGUUACACAU CAUUU
#2 GOLPH3	AAUCCAGAUGAUAUACA GUCAUUCC	GGAAUGACUGUAUAUCAUCU GGAUU
#6 GOLPH3	AAUCCAGAUGAUAUACA GUCAUUCC	GGAAUGACUGUAUAUCAUCU GGAUU
#7 GOLPH3	UCAAGGACCGCGAGGGU	UAACCCUCGCGGUCCUUGA

Table 8. siRNA sequences. Sequences of siRNAs used for GOLPH3 gene silencing

3.13 mRNA extraction, retrotranscription and RT-PCR

To assess gene silencing in DU145 cells, total RNA was extracted using an on-column RNA extraction kit (abm). Reverse transcription was subsequently performed using the All-in-One 5× RT MasterMix kit (abm), according to the manufacturer's instructions. The cDNA was used to amplify the GOLPH3 gene by qPCR. qPCR reactions were performed in triplicate in a 20 µL reaction volume using the BlasTaq™ 2X qPCR MasterMix kit (abm). Conditions were as follows: 95°C for 3 minutes, followed by 35 cycles of 95°C for 15 seconds, 60°C for 1 minute. The HPRT1 gene was used as a reference gene for normalization of real-time PCR products. The PCR primers used to detect each gene were designed using the Primer 3 program and synthesized by Sigma Aldrich. The tests were performed in technical duplicate for each subject. To confirm the specificity of the reactions, we performed dissociation curve analysis of the amplification products. To analyze the data and obtain relative gene expression levels, the 2-DDCt method was used.

3.14 GOLPH3 Silencing

To inhibit the GOLPH3 gene, DU145 cells were seeded in 12-well plates at 90,000 cells/well in complete medium. After 24 hours, cells were treated with PLGA-IL and LGIP NPs and a pool of anti-GOLPH3 siRNA (50 nM), containing the following sequences as reported in the table for 48–72 hours. The nanosystems and siRNA were diluted in complete medium (750 µL) where 0.614 µg of siRNA (50 nM) was bound to PLGA-ILs (3.21 µg) in a 1:1 ratio. As an internal positive control, cells were treated with Lipofectamine™ RNAiMAX transfection reagent (ThermoFisher).

3.15 Scratch Assay

A scratch assay was performed to first evaluate the effects of ILs on cell migration. PNT2 and DU145 were used. Cells were seeded in 48-well plates (growth area ≈ 1.0 cm^2/well) at a density of 10,000 cells per well, allowing confluence to be reached within 18–24 hour. At confluence, a scratch was created using a sterile 1 mm pipette tip held perpendicular to the well surface. Detached cells were gently removed by washing with PBS, and fresh culture medium was added. Plates were incubated at 37 °C with 5% CO_2, and images of the scratch area were acquired at 0, 24, 48, and 72 h using an inverted optical microscope (Julistage Time Recorder, Nanoentek, Korea) with phase-contrast optics at 4× and 10× magnification. Migration into the wound area was monitored over time, and assays were performed in duplicate.

To assess the effect of GOLPH3 gene silencing on cell migration, cells were seeded in 96-well plates at a density of 15,000 cells/well and allowed to adhere for 24 hours. Subsequently, they were treated

with PLGA-ILs, LGIP-1 NPs and LGIP-10 NPs that bound GOLPH3-specific siRNA and the control treated with Lipofectamine for up to 72 hours. After 72 hours, a linear scratch was performed on the cell monolayer using a sterile 200 µL tip (p200), followed by washing with 1× PBS to remove non-adherent cells and debris, and the subsequent addition of DMEM) and the wound closure was monitored at 2, 4, 6, and 24 hours. Images were acquired using a JuLI™ Stage Recorder inverted optical microscope (Nanoentek, Korea) with a 4× objective. The residual scratch area was quantified by image analysis with ImageJ software (version 1.48i). Each experimental condition was analyzed in three independent experiments, each performed in triplicate.

3.16 Statistical analysis

Statistical analysis was performed using GraphPad Prism software (version 8.0). For the cell proliferation experiments, a two-way ANOVA was performed to compare cell proliferation across increasing NPs concentrations at different timepoints. The results obtained by flow cytometry are reported as the median of the distribution of cellular fluorescence intensity (Resolution matrix) obtained by analyzing 10,000 cells in the gate and normalized on CTR. For qPCR analysis, gene expression fold change was calculated by the 2^(-ΔΔCt) method, and statistical significance was assessed by two-way ANOVA. For the scratch assay, data for each condition were normalized to their respective T0 values, and statistical comparisons with the corresponding control condition were performed using two-way ANOVA.

4. Results

4.1 Preparation of imidazolium-based ionic liquids

Ionic liquids (ILs) represent a class of highly versatile materials, characterized by the presence of completely dissociated ionic species in the liquid phase. This characteristic gives them unique properties, including high chemical stability, low vapor pressure, remarkable ionic conductivity, and the ability to finely tune their chemical and physical characteristics through appropriate structural modifications[73]. These properties make ionic liquids particularly attractive for biomedical applications, particularly as functional components in drug and gene delivery systems. One of the most notable characteristics of ILs is their modular structure. The combination of an ionic head and an alkyl chain of variable length allow for the tuning of key parameters such as hydrophobicity, amphiphilicity, surface charge, and the ability to interact with biomolecules. In the context of gene delivery, this modularity allows for the optimization of electrostatic interaction with the genetic payload, ensuring complexation and protection from enzymatic degradation, without compromising the system's stability or biological compatibility [74]. From a biological perspective, positively charged of imidazolium-based ionic liquids are particularly effective in interacting with polyanionic molecules such as siRNA. This interaction not only promotes high loading efficiency but also helps reduce the loss of genetic material during preparation, transport, and cellular internalization. Furthermore, the ionic nature of ILs can facilitate interaction with the cell membrane, promoting endocytosis and increasing the overall uptake efficiency of nanoparticles [50,75].

Another aspect of particular relevance emerging from this work concerns the ability of ionic liquids to interact with biological membranes. The presence of hydrophobic domains within imidazolium-based ILs likely promotes their partial insertion into lipid bilayers, resulting in increased membrane permeability and enhanced cellular uptake of the nanoparticle systems. This effect is especially advantageous for non-viral vectors, which are generally limited by lower internalization efficiency compared with viral delivery platforms. Importantly, our results suggest that modulation of the alkyl chain length represents a key parameter for balancing membrane interaction and cytocompatibility, as excessive hydrophobicity may lead to membrane destabilization and cytotoxicity. Consistent with this, the initial screening of imidazolium salts with different alkyl chain lengths performed in this study allowed the identification of ILs that are compatible with PLGA nanoparticles and suitable for use as functional surface coatings for siRNA delivery. The ILs selected for the screening were initially dissolved in DMEM to prepare concentrated stock solutions. These stock solutions were

subsequently diluted in DMEM to obtain working concentrations ranging from 0.1 to 10 µg/mL (**Table 9**).

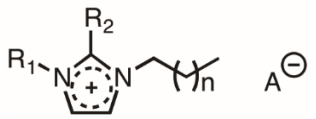

Imidazolium Salt	R_1	R_2	n	A
C_{10}MImCl	CH_3	H	8	Cl
C_{12}MImCl	CH_3	H	10	Cl
C_{14}MImCl	CH_3	H	12	Cl
C_{16}MImCl	CH_3	H	14	Cl
C_{18}MImCl	CH_3	H	16	Cl
C_{16}MImMeS	CH_3	H	14	H_3CSO_3
C_{18}MImMeS	CH_3	H	16	H_3CSO_3
$(C_{10})_2$MImCl	$(CH_2)_9CH_3$	CH_3	8	Cl
$C_{16}C_2$OHImCl	$(CH_2)_2OH$	H	14	Cl
C_{16}BnImCl	$CH_2C_6H_5$	H	14	Cl
C_{18}BnImCl	$CH_2C_6H_5$	H	16	Cl

Table 9. Structural characteristics of the imidazolium core-based ionic liquids selected for this study. The selection includes series characterized by different hydrophobic chain lengths (C10-C18), different functionalizations of the R_1 group (methyl, hydroxyethyl, benzyl), and different anions (chloride and methanesulfonate).

4.1.1 ^{1}H NMR characterization of selected ionic liquids

All ILs included in the screening were characterized by ^{1}H NMR spectroscopy. However, for clarity and conciseness, this thesis reports only the ^{1}H NMR spectra of the ILs selected for nanoparticles functionalization, which are presented as representative of the complete characterization. The ^{1}H NMR spectra of C16MImCl and C10MImCl were acquired in $CDCl_3$ at 400 MHz to confirm their chemical identity and purity. For C16MImCl, the spectrum shows characteristic signals of the imidazole ring at δ 10.57 (s, 1H), 7.40 (s, 1H), and 7.28 (s, 1H), consistent with the predicted proton environment for the heterocyclic core. The methylene protons adjacent to the nitrogen atom appear as a triplet at δ 4.32 (t, J = 7.4 Hz, 2H), while the methyl group bonded to the nitrogen shows a singlet at δ 4.13 (s, 3H). The long alkyl chain exhibits a broad multiplet between δ 1.38–1.22 (m,

26H) and a terminal triplet at δ 0.89 (t, J = 6.7 Hz, 3H), confirming the presence of the sixteen-carbon chain. Similarly, C10MImCl shows signals from the imidazole ring at δ 10.18 (s, 1H), 7.45 (s, 1H), and 7.30 (s, 1H), the methylene protons near the nitrogen at δ 4.28 (t, J = 7.4 Hz, 2H), and the N-methyl protons at δ 4.07 (s, 3H). The ten-carbon alkyl chain appears as a multiplet between δ 1.38–1.16 (m, 14H) and a terminal triplet at δ 0.85 (t, J = 6.9 Hz, 3H) [76,77]. No significant impurities were observed, confirming the successful synthesis of the ionic liquids (**Figure 9**).

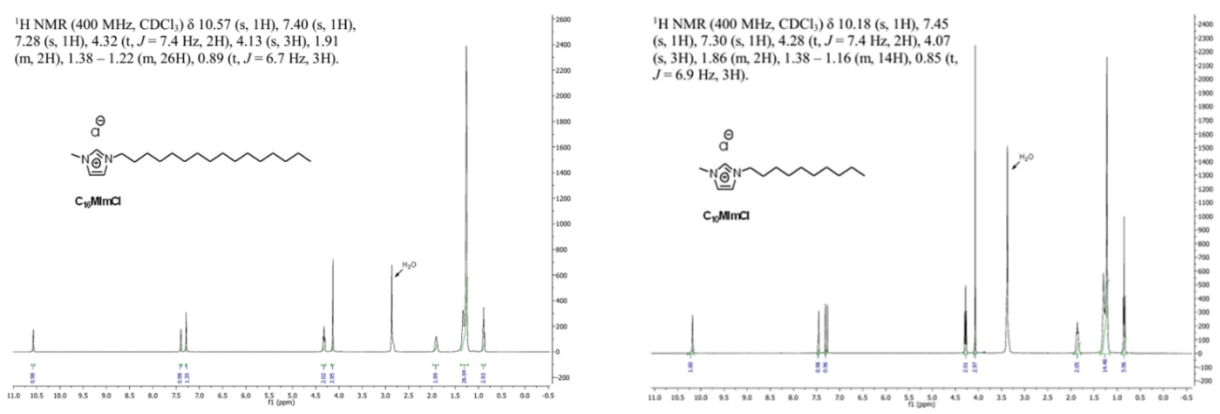

Figure 9. .^1H NMR spectra of C16MImCl and C10MImCl in $CDCl_3$ (400 MHz). The spectra show the imidazolium ring protons (δ 10.57–10.18, 7.40–7.30 ppm), the N-methyl group (δ 4.13–4.07 ppm), and the methylene and terminal methyl protons of the alkyl chains, confirming the expected chemical structure and absence of significant impurities.

The differences in chemical shift patterns between the C16 and C10 derivatives primarily reflect the variation in alkyl chain length, which influences the number and position of methylene protons. These structural differences directly determine key properties such as hydrophobicity and molecular packing, crucial parameters when these ionic liquids are used to functionalize PLGA nanoparticles. In particular, longer chains (C16) increase lipophilicity and can promote more stable interaction with cell membranes, while shorter chains (C10) reduce hydrophobicity, favoring faster diffusion but less intense surface adsorption [78].These NMR data therefore not only confirm the chemical identity and purity of the synthesized ILs, but also provide a structural basis for interpreting the differences observed in their biological behavior in both 2D and 3D models, as well as their impact on the functional properties of PLGA-based nanoparticles.

4.1.2 ILs *in vitro* biocompatibility studies

ILs, particularly imidazolium-based ionic salts, are increasingly explored as functional components in nanoparticles formulations for gene delivery due to their tunable amphiphilicity, cationic character, and ability to modulate surface properties [75]. When incorporated into polymeric or hybrid nanocarriers, ILs can enhance nucleic acid complexation, cellular uptake, and intracellular trafficking. However, their membrane-active nature raises important safety considerations, making it essential to carefully evaluate their intrinsic cytotoxicity and selectivity prior to nanoparticle formulation. In this context, a screening was conducted to assess the tolerability of a structurally diverse panel of imidazolium salts in healthy and cancerous prostate cells. The aim of this study was not to evaluate ILs as standalone therapeutics, but rather to identify ionic salts with favorable biocompatibility and selectivity profiles that could be safely integrated into nanoparticle systems for gene delivery applications. As shown in **Table 9**, a large panel of structurally diverse ILs was selected for this study, including imidazole derivatives with different alkyl chain lengths, aromatic substitutions, and different counterions. Cell viability was assessed using a CCK-8 assay in PNT-2 and DU145 cell lines. PNT-2 cells, representing non-malignant prostate epithelial cells, were employed to evaluate biocompatibility toward healthy tissue, while DU145 cells, a human prostate carcinoma cell line, were used to assess selective cytotoxicity against malignant cells. This dual-cell model enabled a direct comparison between safety in normal cells and therapeutic selectivity toward cancer cells. The compounds were tested at concentrations ranging from 0.025 to 2.0 μg/mL to identify a concentration range that preserves cell viability in both healthy and tumor cells, ensuring their suitability for use as coatings on PLGA-based nanoparticles and for subsequent siRNA delivery applications. In PNT2 cells, exposure to the different ionic salts did not result in a significant reduction in cell viability, which generally remained above 80% for both 24 and 72 hours of treatment. Notably, at the lowest concentrations (0.025–0.1 μg/mL), viability consistently exceeded 90% for all compounds tested, indicating negligible cytotoxic effects. Even at the highest concentrations (1.0–2.0 μg/mL), only slight decreases in viability were observed, with the most notable effect associated with C16MImCl after 72 hours. However, it is crucial to emphasize that in no case did cell survival fall below the critical threshold of 70%. This value is defined by the international standard ISO 10993-5 as the minimum viability limit below which a material is considered cytotoxic [79]. Full compliance with these international standards confirms the biocompatibility of imidazolium salts and supports their suitability as functionalizing agents for nanoparticles. Furthermore, the relative resistance of healthy cells to imidazolium salts suggests that non-tumorigenic cells possess more efficient protective mechanisms against oxidative stress and membrane alterations induced by amphiphilic cations (**Figure 10**).

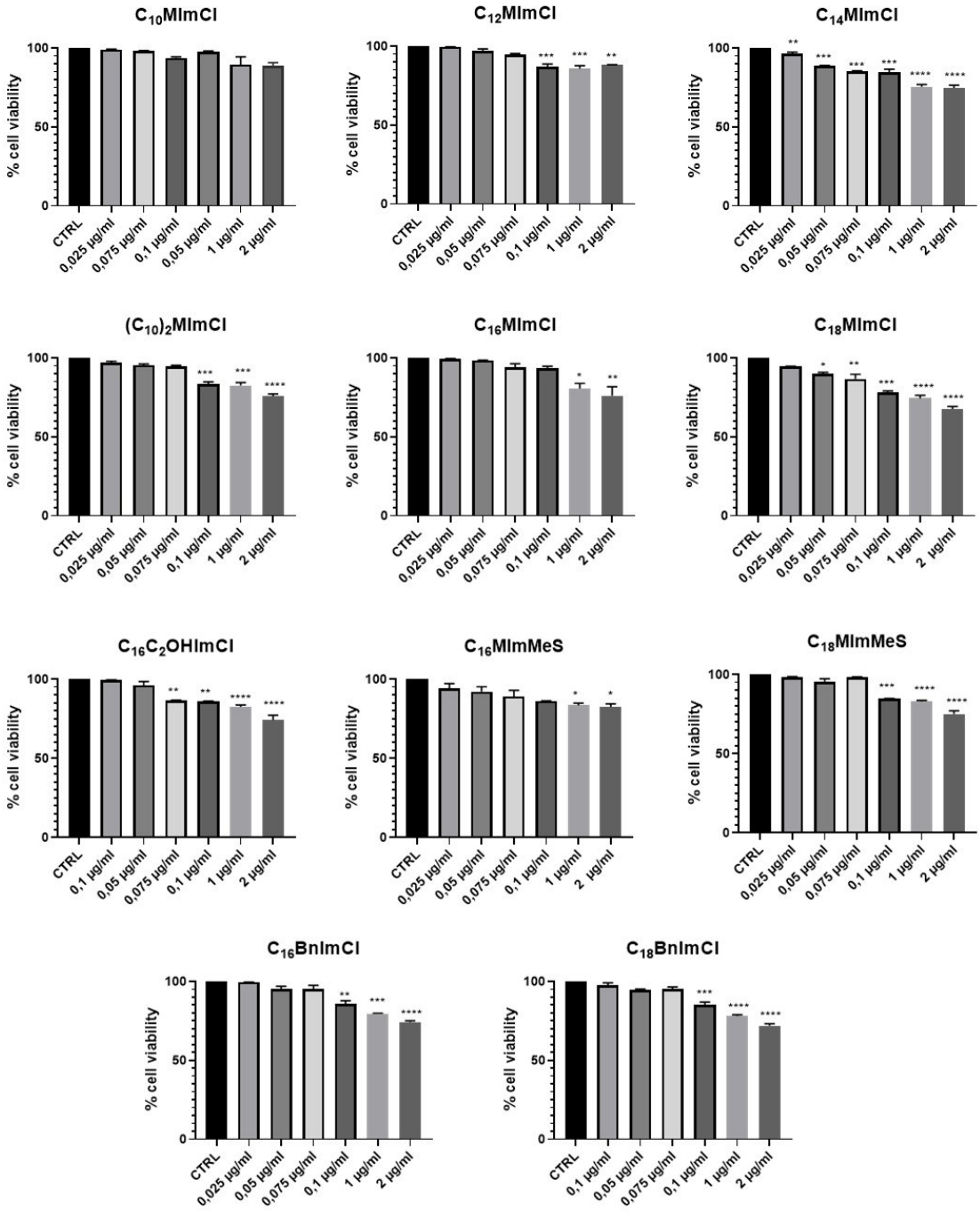
C10MImCl
C12MImCl
C14MImCl
(C10)2MImCl
C16MImCl
C18MImCl
C16C2OHImCl
C16MImMeS
C18MImMeS
C16BnImCl
C18BnImCl
% cell viability
CTRL
0,025 µg/ml
0,05 µg/ml
0,075 µg/ml
0,1 µg/ml
1 µg/ml
2 µg/ml

(A)

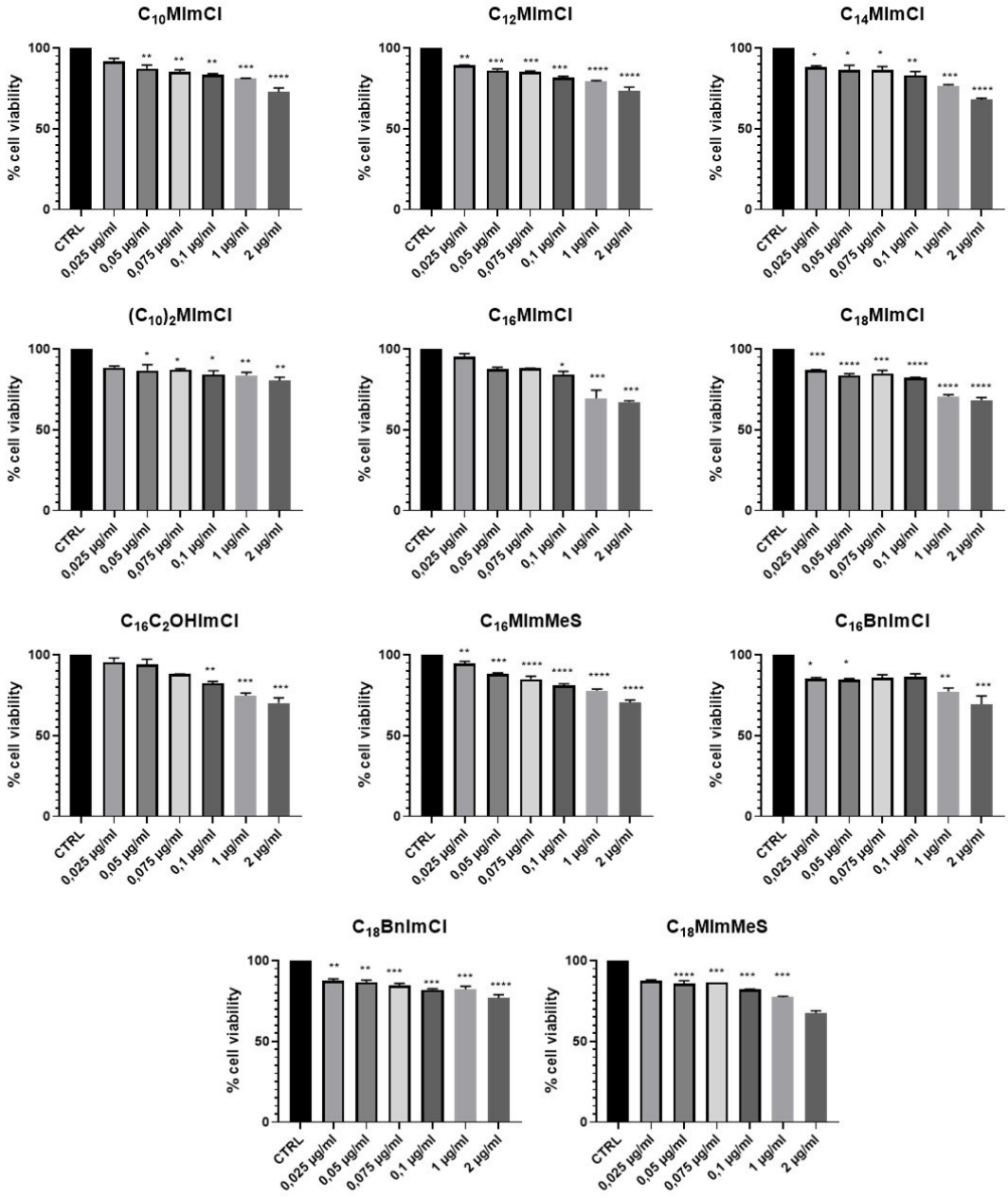

(B)

Figure 10. Assessment of cell viability in non-tumorigenic prostate epithelial cells (PNT2) following exposure to selected ionic liquids. Cell viability was measured using the CCK-8 assay after **A**) 24 h and **B**) 72 h of treatment with concentrations ranging from 0.025 to 2.0 µg/mL. Results are expressed as mean ± SD (n = 3). Statistical significance compared with the untreated control: (*) $0.05 < p \leq 0.10$; (**) $0.01 < p \leq 0.05$; (***) $0.001 < p \leq 0.01$; (****) $p \leq 0.001$.

The data obtained with the CCK-8 assay were further confirmed by live/dead staining. PNT2 cells treated with C_{10}MImCl, C_{16}MImCl, and C_{16}BnImCl at concentrations of 0.1, 0.5, and 1.0 µg/mL displayed predominantly green fluorescence, indicative of membrane integrity and preserved

metabolic activity. Only minimal red fluorescence signals, indicative of cell death, were observed, primarily at the highest concentration of C_{16}MImCl (1.0 µg/mL), confirming the high tolerability of ILs in healthy cells even at doses higher than those required to induce cytotoxic effects in tumor cells (**Figure 11**).

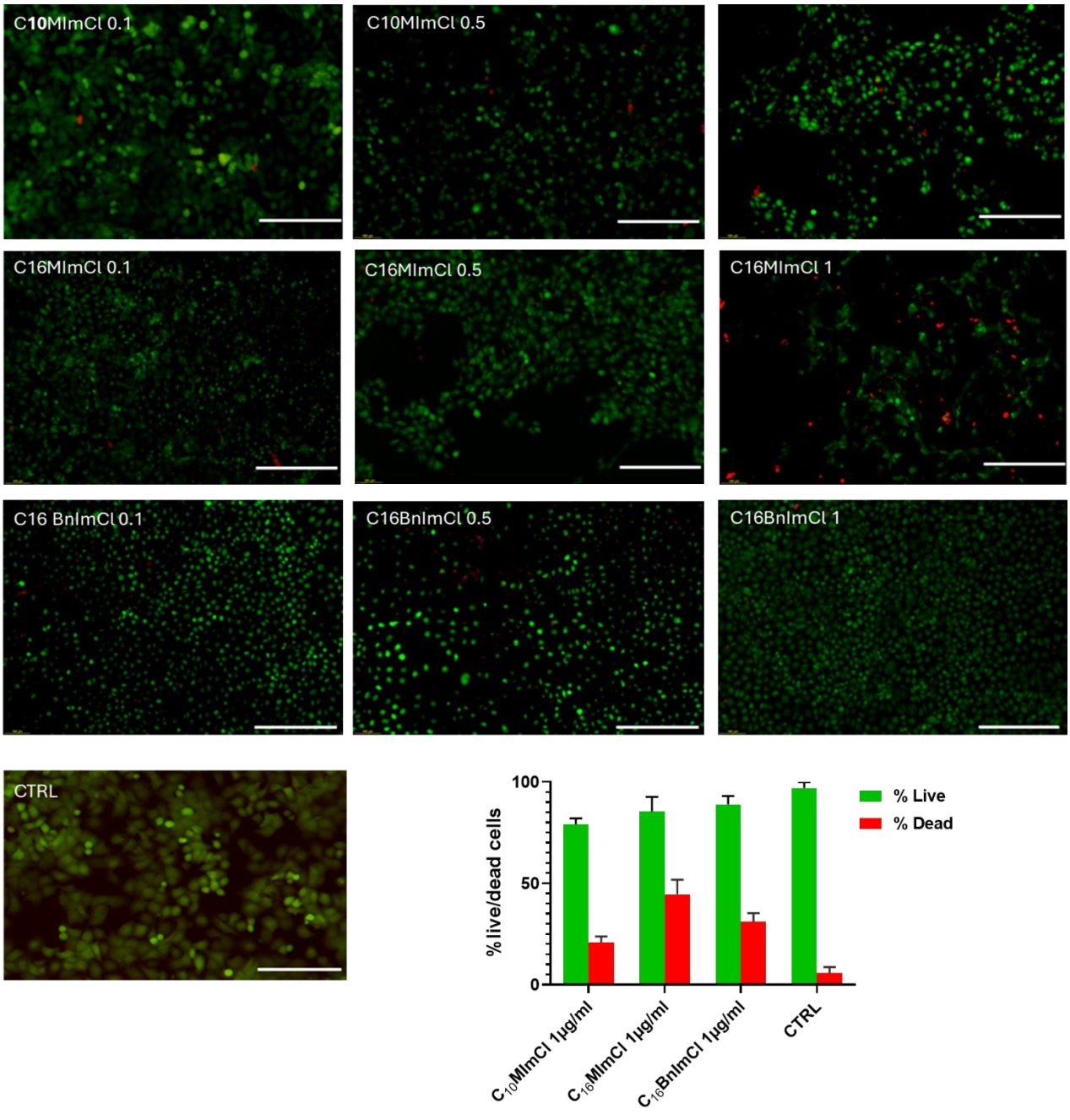

Figure 11. Assessment of cell viability in non-tumorigenic prostate epithelial cells (PNT2) following exposure to selected ionic liquids. Representative fluorescence images from the live/dead assay performed on non-tumorigenic prostate epithelial cells (PNT2) after 24 h of exposure to C_{10}MImCl, C_{16}MImCl, and C_{16}BnImCl at 0.1, 0.5, and 1.0 µg/mL. Viable cells are visualized in green fluorescence, while dead cells appear in red.

In contrast, DU145 cells showed a dose-dependent decrease in viability when exposed to the panel of selected ILs. A reduction in cell survival was observed at concentrations between 0.1 and 2.0 µg/mL, with more pronounced effects at higher doses. Specifically, C_{16}BnImCl caused a more marked reduction in the fraction of viable cells compared to untreated controls, suggesting that certain structural modifications of ionic liquids may modulate cytotoxicity at high concentrations. These results indicate that ILs can have significant biological effects when used at high doses, potentially exploitable for antitumor activity (**Figure 12**).

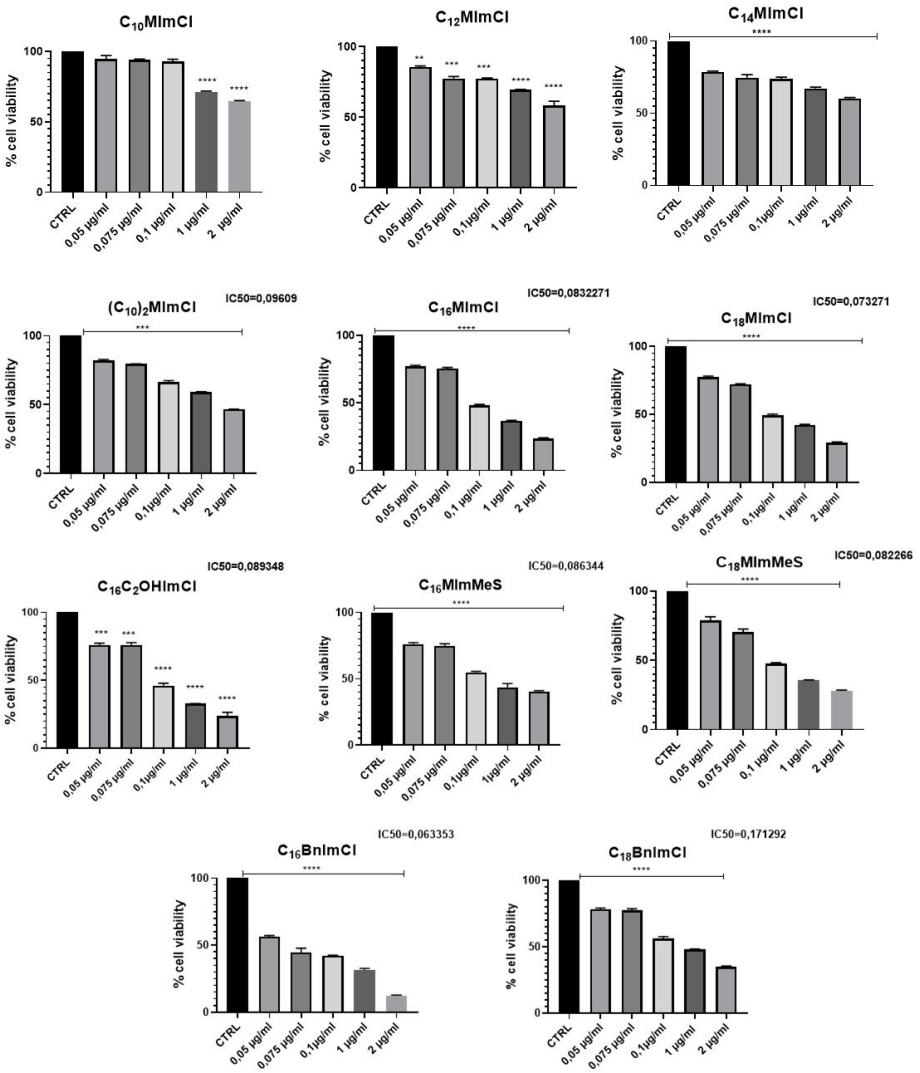

(A)

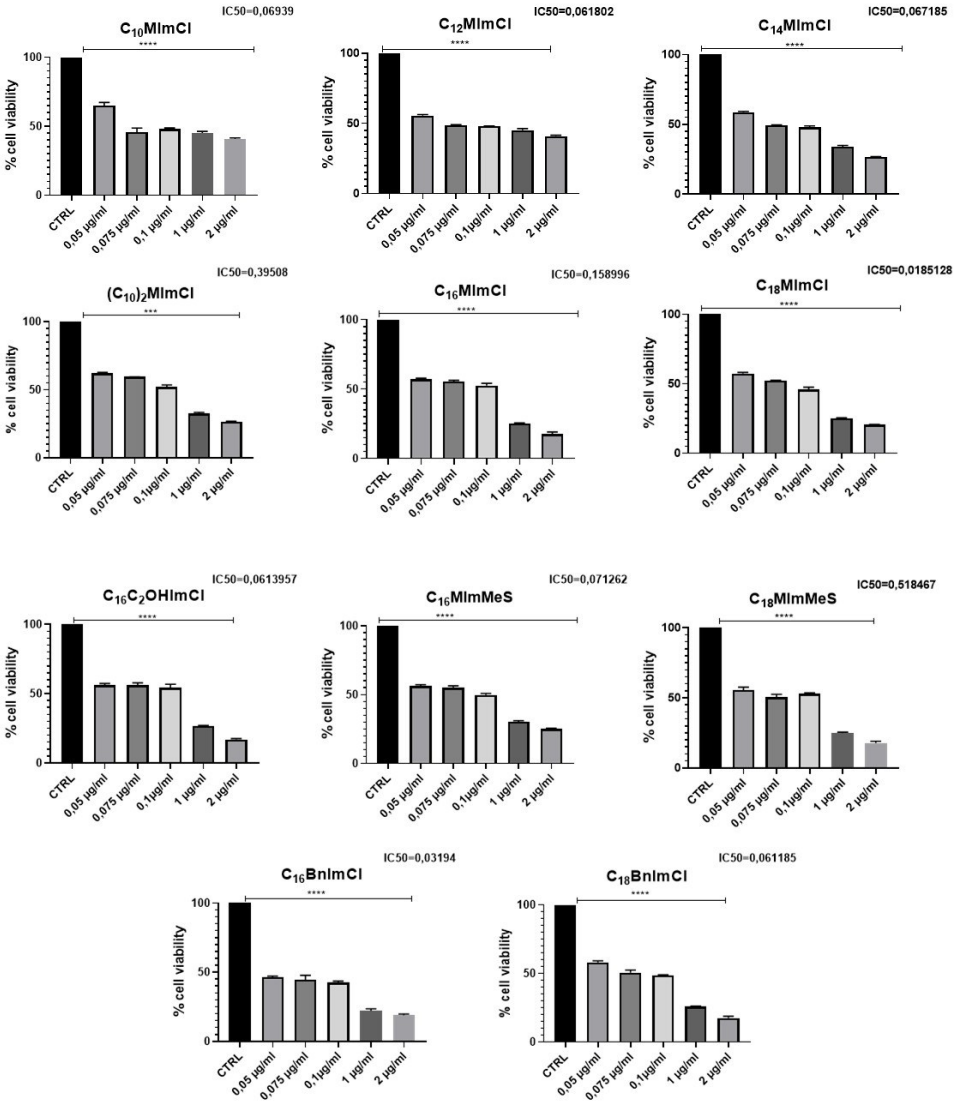

(B)

Figure 12. Assessment of DU145 prostate cancer cell viability following exposure to selected ionic ILs. Cells were treated for **A**) 24 h and **B**) 72 h with increasing concentrations (0.025–2.0 µg/mL), and viability was quantified using the CCK-8 assay. Results are expressed as mean ± SD (n = 3). Statistical significance compared with the untreated control: (*) $0.05 < p \leq 0.10$; (**) $0.01 < p \leq 0.05$; (***) $0.001 < p \leq 0.01$; (****) $p \leq 0.001$.

Live/dead staining corroborated the findings of the viability assays by visually illustrating the concentration-dependent effects of ionic liquids on cellular viability. At lower concentrations, the majority of cells remained viable, as evidenced by predominant green fluorescence. However, as the concentration of the compounds increased, a progressive reduction in green-stained viable cells was observed, accompanied by a marked increase in red-stained dead cells. This trend clearly indicates a dose-dependent cytotoxic response to the ionic liquids (**Figure 13**).

Among the ionic liquids evaluated, C_{16}BnImCl exhibited the most pronounced cytotoxic effect, completely abolishing green fluorescence at a concentration of 1.0 μg/mL. In contrast, C_{10}MImCl and C_{16}MImCl induced less severe, though still detectable, reductions in cell viability. These findings underscore the role of specific structural features, particularly benzyl substitution, in modulating cellular interactions at higher concentrations.

The inclusion of benzyl-substituted ionic salts such as C_{16}BnImCl was intentionally guided by bioinspiration from lepidilines, a family of naturally occurring benzylquinoline and benzylisoquinoline alkaloids whose natural isolates and synthetic analogues have demonstrated notable cytotoxic and antimicrobial activities. Structural motifs characteristic of lepidilines and related benzyl-isoquinoline/benzyl-quinoline compounds have repeatedly been associated with antitumor and antimicrobial efficacy, with several studies reporting selective cytotoxicity across cancer cell lines and structure–activity relationships implicating benzyl and other aromatic substructures as key pharmacophoric elements [80,81].

Accordingly, the incorporation of a benzyl substituent into the imidazole core represents a bioinspired design strategy aimed at mimicking these pharmacophore features, namely, a planar aromatic system combined with a lipophilic benzyl moiety. These characteristics are known to enhance membrane affinity and cellular uptake and to influence target interactions in quinoline and isoquinoline derivatives. Consistent with this rationale, previous synthetic and biological investigations of lepidilines and benzylisoquinoline derivatives have reported enhanced antiproliferative activity and, in some cases, increased selectivity for benzyl-substituted analogues. Collectively, these observations support the hypothesis that benzylation of the imidazole scaffold may contribute to increased cytotoxic potency against prostate cancer cells through augmented lipophilicity and membrane interactions.

Importantly, despite their pronounced effects at higher concentrations, these ionic liquids maintained acceptable biocompatibility at lower doses, confirming their suitability for use as nanoparticle coatings. Under these conditions, cell viability was preserved, and the functional properties required for gene delivery applications were retained.

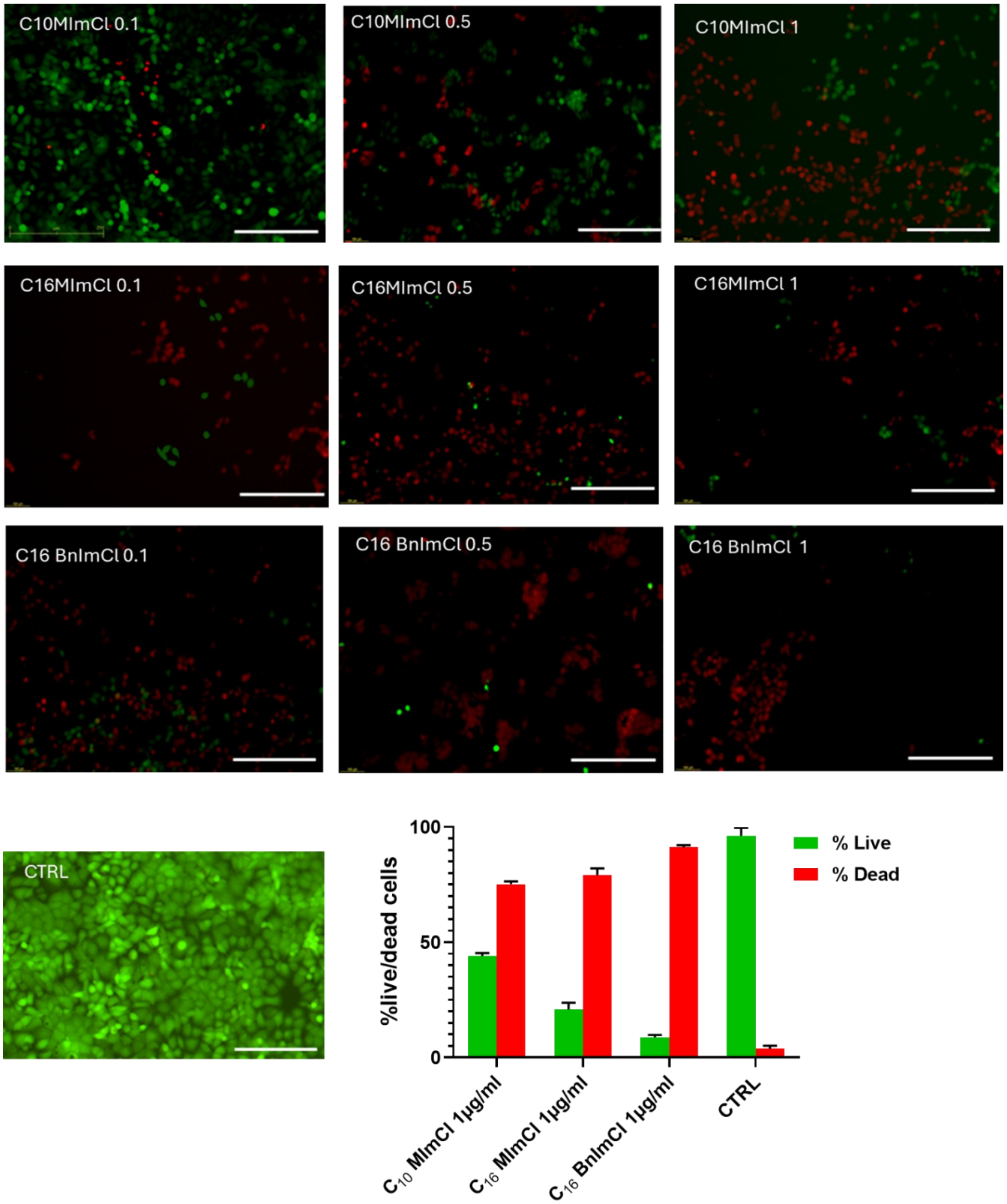

Figure 13. Assessment of DU145 prostate cancer cell viability following exposure to selected ionic ILs

Representative fluorescence images from the live/dead assay performed on DU145 prostate cancer cells after 24 h exposure to the ionic liquids C_{10}MImCl, C_{16}MImCl, and C_{16}BnImCl at 0.1, 0.5, and 1.0 µg/mL. Viable cells are visualized by green fluorescence, while dead cells appear red.

These results identified a concentration range in which imidazolium-based ionic salts can be considered biologically safe for both non-tumorigenic (PNT2) and prostate cancer (DU145) cells. Across the entire panel of ionic salts tested, cell viability in PNT2 cells consistently remained above commonly accepted biocompatibility thresholds at concentrations up to 2.0 μg/mL, indicating good tolerability of these compounds in healthy prostatic epithelial cells. In DU145 cells, a clear dose-dependent reduction in viability was observed only at higher concentrations; however, cell survival remained acceptable at lower concentrations, particularly in the submicrogram range. Analyzing the different ionic salts, derivatives with C_{10} and C_{16} alkyl chains stood out for the best safety and selectivity profile, showing little impact on the viability of both healthy and cancer cells. Overall, these results successfully identified imidazolium salts with favorable characteristics, supporting their use as functional components in nanoparticle-based gene delivery systems. In particular, C_{10}MImCl and C_{16}MImCl emerge as ideal candidates for incorporation into PLGA nanoparticles, whose physicochemical properties were exploited to optimize siRNA loading while ensuring an acceptable biocompatibility profile.

4.1.3 Selective ILs-induced oxidative stress

Oxidative stress is a well-recognized mechanism through which many amphiphilic and cationic compounds exert biological effects, particularly in cancer cells, which are characterized by altered redox homeostasis and elevated basal levels of reactive oxygen species (ROS). Excessive ROS production can disrupt mitochondrial function, induce oxidative damage to cellular macromolecules, and ultimately lead to cell death. Conversely, normal cells typically possess more efficient antioxidant defense systems, enabling them to tolerate moderate oxidative challenges. In the context of ionic salts intended for incorporation into nanoparticle-based gene delivery systems, it is therefore essential to evaluate whether their intrinsic biological activity induces oxidative stress in a dose- and cell-type–dependent manner. Accordingly, intracellular ROS generation was assessed in non-tumorigenic and malignant prostate cell lines following exposure to selected imidazolium-based ionic salts.

Intracellular ROS production was quantified using the fluorescent probe DCFH-DA (20 μM) after 24 h treatment with C_{10}MImCl, C_{16}MImCl, and C_{16}BnImCl at increasing concentrations (0.1, 0.5, and 1.0 μg/mL). In PNT-2 cells, ROS levels remained low and comparable to untreated controls across all concentrations tested, indicating the absence of significant oxidative stress. Even at the highest concentration, fluorescence signals did not deviate from baseline, confirming that these ionic salts do not induce measurable ROS accumulation in normal prostate epithelial cells.

In contrast, DU145 prostate cancer cells exhibited a clear, dose-dependent increase in intracellular ROS levels (**Figure 14**). The strongest ROS induction was observed for C_{10}MImCl at 1.0 µg/mL, followed by C_{16}BnImCl, while C_{16}MImCl elicited a more moderate increase. This pattern closely mirrors the trends observed in cytotoxicity assays, suggesting that oxidative stress contributes to the anticancer activity of these compounds. The selective induction of ROS in malignant cells highlights a redox vulnerability that may be therapeutically exploited.

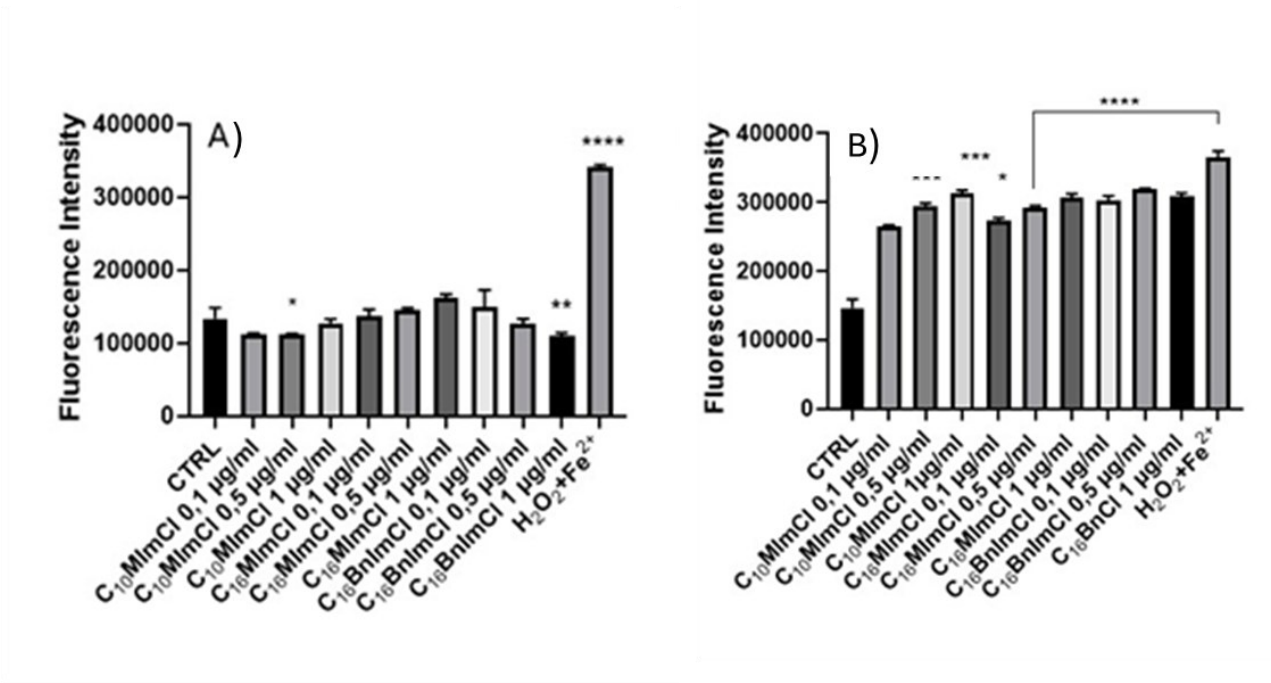

Figure 14. ILs-induced oxidative stress. Measurement of reactive oxygen species (ROS) levels in **A**) PNT2 and **B**) DU145 cells following 24 h exposure to the ionic liquids C_{10}MImCl, C_{16}MImCl, and C_{16}BnImCl at 0.1, 0.5, and 1.0 µg/mL. ROS production was evaluated by fluorescence quantification. Data represent mean ± SD (n = 3). Statistical significance compared with the untreated control: (**) $0.01 < p \leq 0.05$; (****) $p \leq 0.001$

Importantly, while C_{16}BnImCl displayed a pronounced pro-oxidant and cytotoxic profile, C10MImCl and C_{16}MImCl exhibited more balanced behavior, characterized by minimal oxidative stress in non-malignant cells and a controlled, dose-dependent ROS induction in cancer cells. This more favorable safety profile supports their selection for further development as surface-modifying agents for PLGA nanoparticles, where maintaining cell viability and minimizing unintended oxidative damage are essential for efficient and safe siRNA loading and delivery.

.

4.1.4 *In vitro* assessment of ILs-induced activation of apoptosis

Assessment of apoptosis and necrosis is essential to clarify the mechanisms underlying changes in cell viability observed in preliminary cytotoxicity studies. While reductions in metabolic activity can arise from reversible cytostatic effects, the activation of apoptotic or necrotic pathways reflects more profound cellular damage and has important implications for both safety and selectivity. For ionic salts intended for integration into nanoparticle-based gene delivery systems, it is particularly important to ensure that they do not trigger programmed cell death in healthy cells within the intended concentration range. At the same time, differential activation of apoptosis in cancer cells may provide useful information on selective biological responses. In this context, Annexin V–FITC and propidium iodide (PI) staining followed by flow cytometry was employed to investigate apoptosis and necrosis induced by selected imidazolium salts in non-tumorigenic and malignant prostate cells. PNT2 and DU145 cells were treated for 24 hours with increasing concentrations of 0.1, 0.5, and 1.0 μg/mL of the compounds. For PNT2 cells, the majority of the cell population remained in the viable cell gate under all conditions tested, with only a small fraction showing apoptotic or necrotic signals at higher concentrations, especially for C_{16}MImCl. No significant differences were observed compared to untreated controls, confirming that ILs exert negligible cytotoxic pressure on non-tumorigenic prostatic epithelial cells. These results indicate that imidazole salts do not activate major apoptotic or necrotic pathways in normal cells, consistent with their favorable safety profile (**Figure 15**).

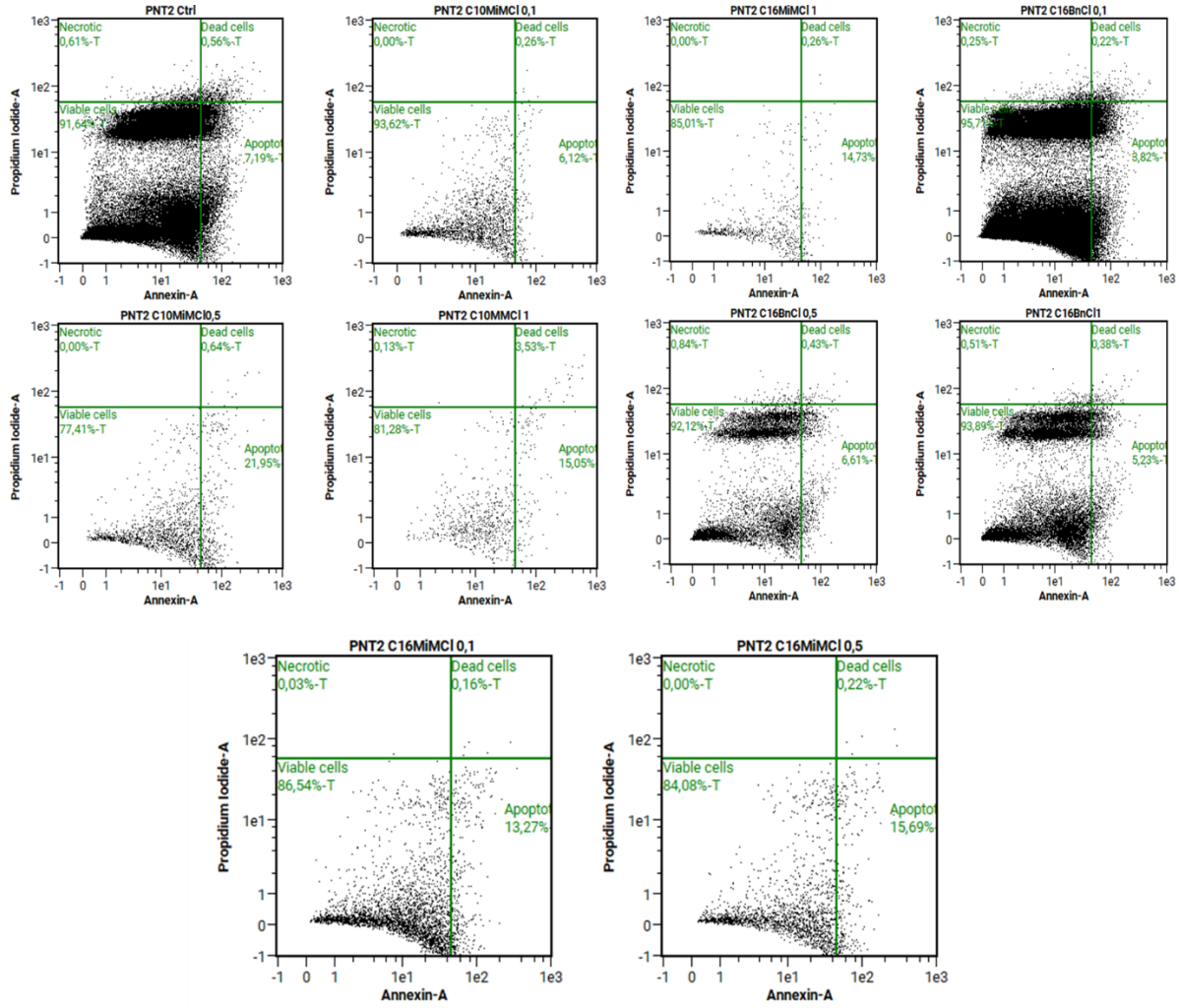

Figure 15. ILs-induced activation of apoptosis in non-tumorigenic prostate epithelial cells (PNT2). Representative flow cytometry dot plots of non-tumorigenic prostate epithelial cells (PNT2) following 24 h exposure to the ionic liquids C_{10}MImCl, C_{16}MImCl, and C_{16}BnImCl at 0.1, 0.5, and 1.0 µg/mL. The plots display the gating strategy used to distinguish viable cells from apoptotic and necrotic populations.

In DU145, however, flow cytometry revealed a clear dose-dependent effect. As ILs concentrations increased, a large portion of the cell population shifted from the viable cell gate to the apoptotic and necrotic quadrants. The most pronounced effect was observed with C_{16}BnImCl at 1.0 µg/mL, which induced high levels of late apoptosis and necrosis. C_{16}MImCl and C_{10}MImCl showed more moderate cytotoxic activity, confirming that imidazole salts selectively activate programmed death pathways in aggressive tumor cells (**Figure 16**).

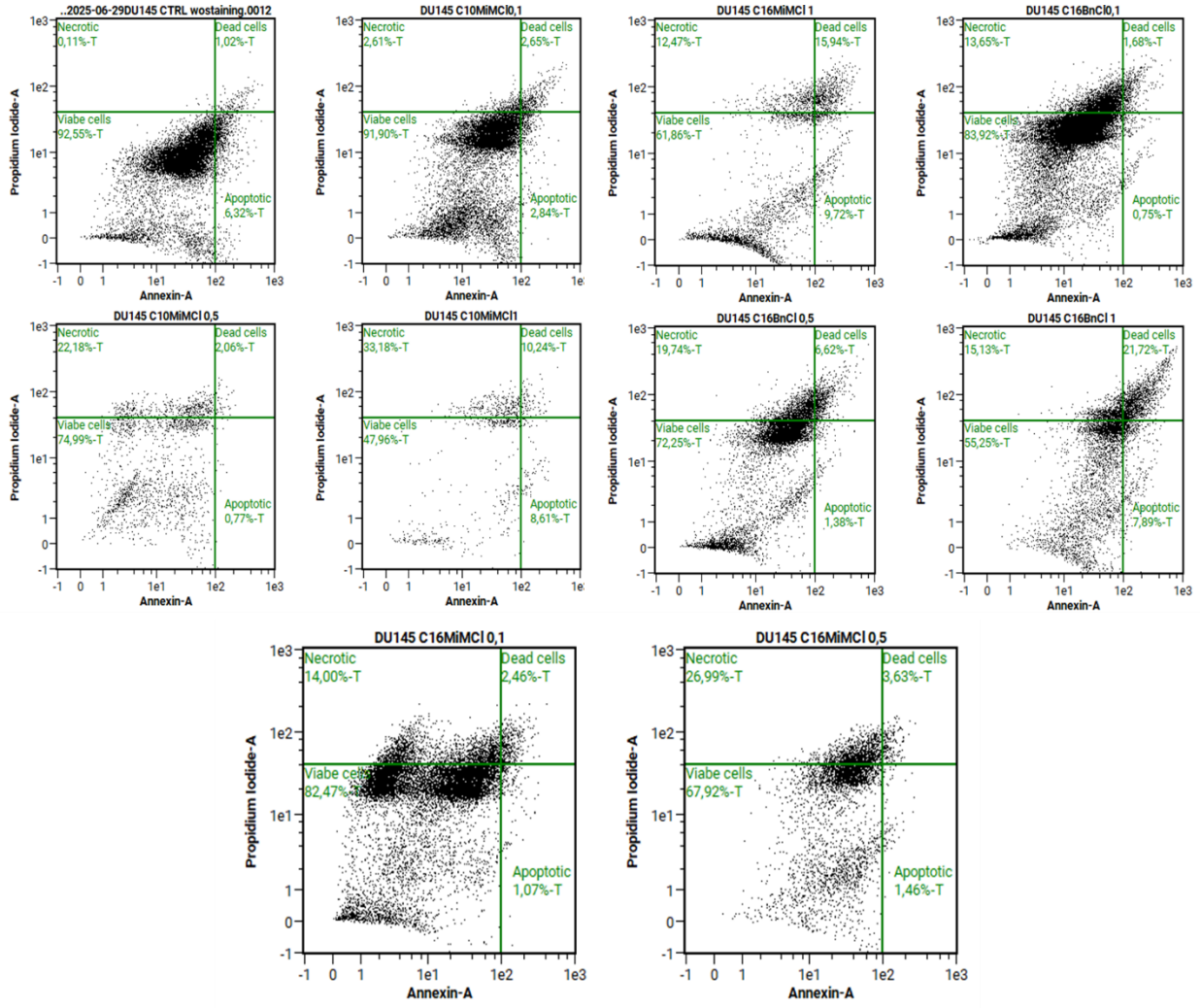

Figure 16. ILs-induced activation of apoptosis in DU145 cancer cells. Representative flow cytometry dot plots of DU145 prostate cancer cells following 24 h exposure to the ionic liquids C_{10}MImCl, C_{16}MImCl, and C_{16}BnImCl at 0.1, 0.5, and 1.0 μg/mL. The plots illustrate the distribution of viable, apoptotic, and necrotic cell populations.

The apoptosis analysis provides important confirmation of the cytotoxicity and ROS data, helping to distinguish between general metabolic impairment and the activation of defined cell death pathways. The preservation of viability and the minimal induction of apoptosis or necrosis in PNT2 cells across all tested concentrations indicate that imidazolium-based ionic salts do not trigger deleterious death signaling in healthy prostate epithelial cells within the identified safe range. This finding is particularly relevant for their intended use as functional components in nanoparticle formulations, where maintaining the integrity of normal cells is a primary requirement. In contrast, the pronounced and dose-dependent induction of apoptosis in DU145 cells demonstrates that malignant prostate cells are significantly more susceptible to ILs-induced cell death. This selective response is consistent with

earlier observations of increased ROS production and reduced viability in DU145 cells and suggests that oxidative stress and membrane perturbation converge on apoptotic pathways in cancer cells. The progression from early apoptosis to late apoptosis and necrosis at higher concentrations further indicates that increasing ILs exposure overwhelms tumor cell defense mechanisms.

Overall, this apoptosis study reinforces the conclusion that imidazolium salts display a favorable safety profile in non-tumorigenic cells and a distinct, concentration-dependent biological response in prostate cancer cells. By defining concentrations that do not induce ROS production and do not activate apoptotic pathways in cells, these results support the use of selected ionic salts within a controlled window for nanoparticle-based gene delivery applications.

4.1.5 Effect of Ionic Liquids on cell migration

Cell migration is a fundamental biological process involved in tissue homeostasis and repair, but it also plays a critical role in cancer invasion and metastasis. The wound-healing assay is widely used to assess collective cell migration and provides functional insight into how chemical agents influence cytoskeletal organization, cell–cell interactions, and adhesion dynamics. In the context of ionic salts intended for use as functional components of nanoparticle-based gene delivery systems, it is essential to verify that they do not adversely affect the migratory capacity of healthy cells within the selected concentration range. At the same time, differential effects on tumor cell migration may indicate selective biological responses that could be therapeutically advantageous. In this context, the effects of selected imidazolium-based ionic salts on the migratory behavior of non-tumorigenic and malignant prostate cells were systematically evaluated. The wound healing assay was used to assess the impact of ILs on the migratory capacity of PNT2 and DU145 prostate cells. After 24 hours of seeding, cells were treated with C_{10}MImCl, C_{16}MImCl, and C_{16}BnImCl at concentrations ranging from 0.1 to 1.0 μg/mL, and the scratch area was monitored for 72 hours by imaging at regular intervals. In PNT-2 cells, the scratch progressively closed under all treatment conditions, indicating that neither migratory behavior nor proliferative capacity were compromised. No statistically significant differences were observed compared to untreated controls, confirming that these ionic salts do not interfere with essential cellular functions in non-malignant prostate epithelial cells. These findings are consistent with viability data, which showed preserved cell morphology and proliferation, suggesting that cytoskeletal organization, cell adhesion, and intercellular communication remain functionally intact following treatment (**Figure 17**).

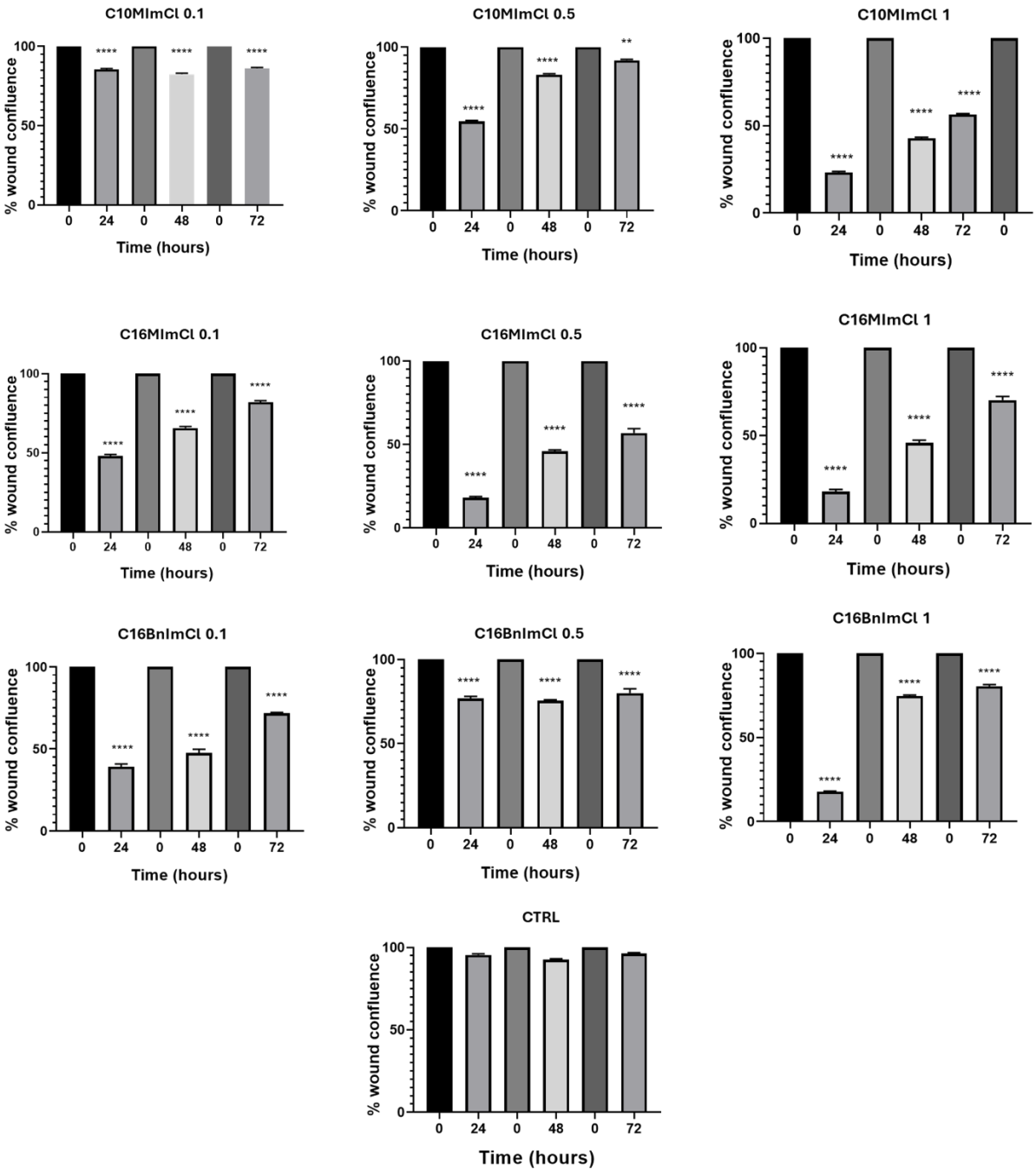

Figure 17. ILs-mediated effects on cell migration in non-tumorigenic prostate epithelial cells (PNT2).

Representative images from the scratch assay performed on non-tumorigenic prostate epithelial cells (PNT2) following treatment with the ionic liquids C_{10}MImCl, C_{16}MImCl, and C_{16}BnImCl at 0.1, 0.5, and 1.0 µg/mL. Images were collected at 0, 24, 48, and 72 h to evaluate cell migration dynamics and wound closure.

In contrast, treatment of DU145 cells resulted in a marked inhibition of cell migration, with a clear concentration-dependent effect. While control cells progressively closed the wound, treated cultures retained substantial open areas over time. Among the tested compounds, C_{16}BnImCl at 1.0 µg/mL almost completely suppressed migratory activity, whereas C_{10}MImCl and C_{16}MImCl induced partial but reproducible inhibition, indicative of a more moderate effect on tumor cell motility. These results indicate that ionic salts selectively impair migration in malignant cells, a key hallmark of tumor aggressiveness, while sparing healthy cells. The observed inhibition of migration in DU145 cells may be associated with alterations in cytoskeletal remodeling and signaling pathways involved in invasiveness, including Rho GTPase signaling and integrin-mediated adhesion. Overall, these findings confirm the selective biological activity of imidazolium-based ionic salts toward malignant cells, suggesting a potential anti-migratory or antimetastatic effect, while non-tumorigenic cells retain normal migratory and proliferative functions (**Figure 18**).

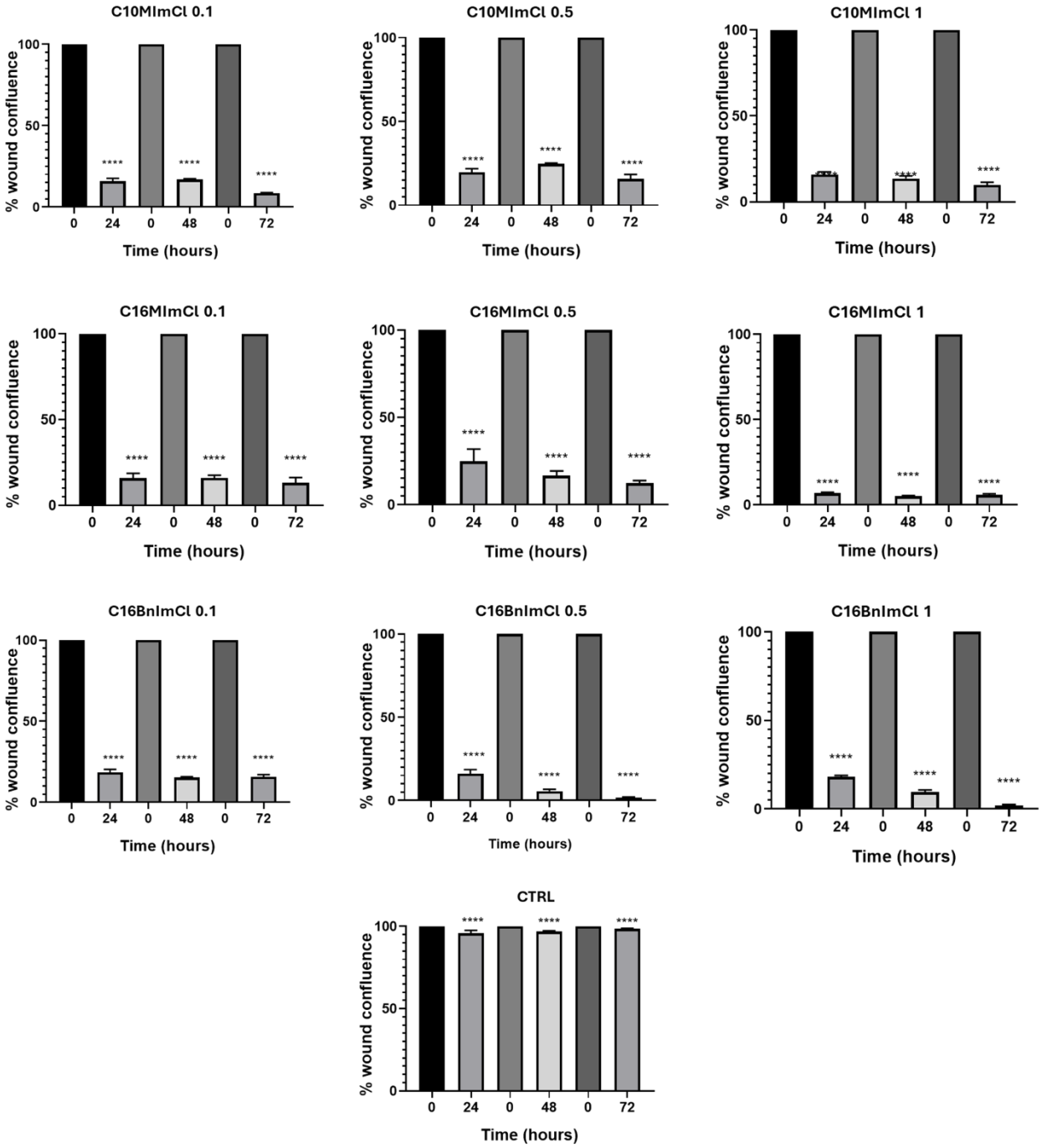

Figure 18. ILs-mediated effects on cell migration in DU145 cancer cells. Representative images from the scratch assay of DU145 prostate cancer cells following treatment with the ionic liquids C_{10}MImCl, C_{16}MImCl, and C_{16}BnImCl (0.1–1.0 µg/mL). Images were acquired at 0, 24, 48, and 72 h to assess the effects of treatment on cell migration and wound closure.

Importantly, although C_{16}BnImCl exhibited the strongest inhibitory effect on cancer cell migration, its pronounced biological activity at higher concentrations may limit its suitability for incorporation into nanoparticle-based delivery systems. In contrast, C_{10}MImCl and C_{16}MImCl demonstrated a more

balanced profile, characterized by preserved migration in healthy cells and controlled inhibition in malignant cells. This balance is particularly desirable for PLGA nanoparticle functionalization, where maintaining normal cellular behavior while enabling selective biological interactions is essential for effective and safe siRNA loading and delivery.

Together with viability, ROS, and apoptosis analyses, the migration assay provides functional confirmation that C_{10}MImCl and C_{16}MImCl represent the most suitable candidates for further development in nanoparticle-based gene delivery applications, combining biocompatibility, selectivity, and functional safety.

4.2 PLGA-ILs preparation and characterization

PLGA nanoparticles have been widely investigated as drug delivery systems due to their biocompatibility, biodegradability, and versatility in surface functionalization [82,83]. For example, PLGA-based nanocarriers have been employed for the encapsulation and controlled release of anticancer drugs such as doxorubicin and paclitaxel, for the delivery of antibiotics and anti-inflammatory agents, and for the transport of nucleic acids and vaccines, demonstrating their broad applicability across different therapeutic areas [84].

In recent years, the incorporation of ILs onto polymeric nanocarriers has attracted increasing attention as a strategy to modulate surface charge, colloidal stability, and potential biological interactions [85]. For instance, ILs-functionalized polymeric nanoparticles have been reported to exhibit enhanced electrostatic stabilization in aqueous media, improved interaction with negatively charged cell membranes, and increased antimicrobial or anticancer activity depending on the nature of the ionic moiety. In particular, the grafting or adsorption of cationic ILs onto polymeric surfaces has been shown to improve nanoparticle dispersion, prolong colloidal stability, and facilitate cellular uptake through charge-mediated mechanisms [52]. In this context, imidazole-based ionic liquids, characterized by tunable alkyl chain lengths and a positively charged imidazolium ring, represent promising candidates for nanoparticle functionalization, as their amphiphilic structure allows fine control over surface properties and biological interactions. The following section describes the synthesis of PLGA-based nanocarriers functionalized with imidazole ILs and their physicochemical characterization. PLGA-based nanocarriers functionalized with imidazole ionic liquids were prepared using an oil-in-water microemulsion method (**Figure 19**). Specifically, the ionic liquids C_{16}MImCl and C_{10}MImCl, containing hexadecyl and decyl alkyl chains, respectively, were dissolved in ultrapure water to form the continuous phase, while the organic phase, consisting of PLGA in chloroform, was slowly added while stirring. Subsequently, the mixture was subjected to sonication, resulting in a

stable microemulsion, and the organic solvent was removed by evaporation under constant stirring. At the end of the process, the spontaneous formation of nanosystems coated with ionic liquids was observed.

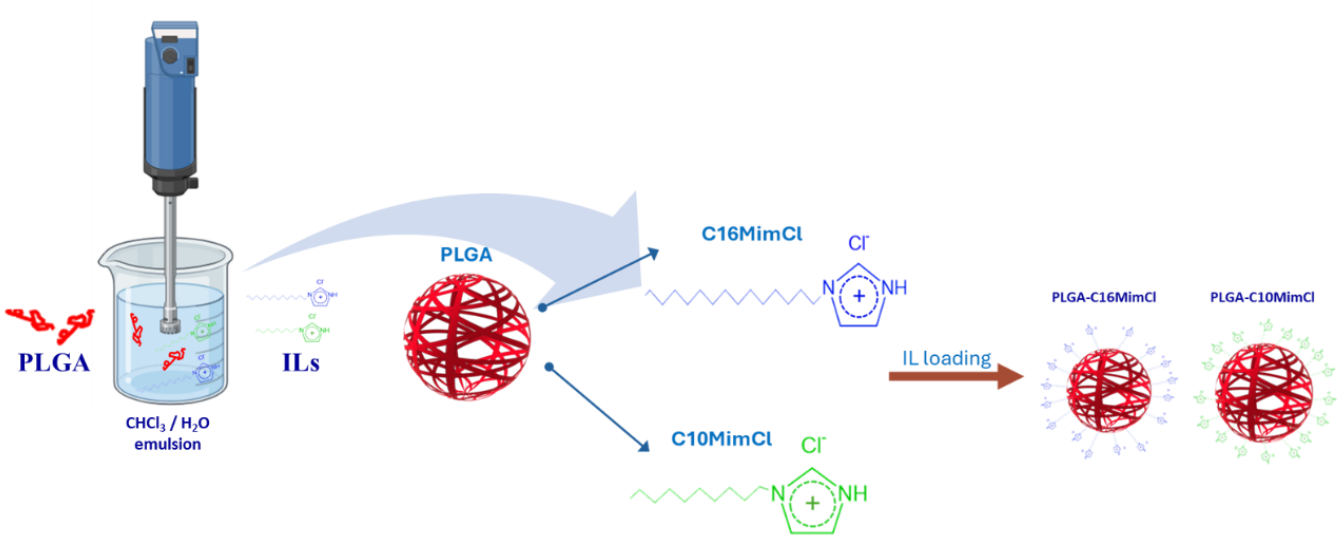

Figure 19. Preparation scheme of PLGA-ILs nanoparticles. Schematic representation of the preparation process of PLGA-based nanoparticles functionalized with imidazole ionic liquids (C_{16}MImCl and C_{10}MImCl). The aqueous phase containing the ionic liquids was mixed with the organic phase containing PLGA in chloroform to obtain an oil-in-water emulsion. Subsequently, solvent evaporation and centrifugation allowed the formation and purification of the nanoparticles coated with ionic liquids (PLGA-C_{16}MImCl and PLGA-C_{10}MImCl).

To evaluate the morphology, size distribution, surface charge, and colloidal stability of the PLGA-ILs NPs nanoparticles, morphological and dimensional characterization was performed using TEM, DLS, and ζ potential measurements (**Figure 20**). TEM images showed spherical nanoparticles with dimensions ranging from 170 to 200 nm for both PLGA-C16 and PLGA-C10 NPs. These values agree with what was reported in previous studies on PLGA nanoparticles functionalized with similar cationic or amphiphilic components, which presented comparable morphology and dimensions, confirming the reproducibility of the adopted formulation strategy [28](**Figure 20A**). DLS analyses confirmed the presence of a monomodal distribution for both nanosystems. The mean hydrodynamic diameter was 182 ± 5.8 nm for PLGA-C16 and 170 ± 11.11 nm for PLGA-C10. In both cases, the polydispersity index (PDI) was less than 0.3, a value indicative of good dimensional homogeneity [86]. Amphiphilic imidazolium-based ionic liquids such as C_{10}MImCl and C_{16}MImCl, characterized by a charged imidazolium headgroup and a hydrophobic alkyl chain, are known to exhibit surfactant-

like behavior in aqueous media. Above their critical aggregation concentration, these molecules may spontaneously self-assemble into micelle-like structures driven by hydrophobic interactions, as previously reported for long-chain 1-alkyl-3-methylimidazolium salts [87]. However, under the formulation conditions adopted in this study, DLS analysis revealed a strictly monomodal size distribution with no evidence of secondary populations in the lower nanometric range that could be attributed to independent IL micelles. This finding strongly supports the formation of a single population of hybrid PLGA-functionalized nanoparticles, in which the ionic liquid is associated with the polymeric matrix rather than forming separate self-assembled aggregates. Finally, the determination of the ζ potential highlighted a positive surface charge for both types of nanoparticles, with values equal to +41,6 ± 0.3 mV for PLGA-C16 and +45.26 ±2.10 mV for PLGA-C10 NPs, confirming the colloidal stability of the nanosystems in aqueous suspension and finding no substantial differences after the loading of dichlorofluorescein. (**Figure 20B**). In previous studies, PLGA nanoparticles functionalized with ILs have shown similar positive ζ potential values and prolonged colloidal stability over time, confirming that the positive surface charge contributes to maintaining the dispersion stable in aqueous suspension [83]. Furthermore, to evaluate the long-term stability of the nanosystems, a stability study was conducted in aqueous solution at 4 °C, monitoring changes in hydrodynamic diameter (Dh) for up to 120 days. As shown in **Figure 20C**, the ionic liquid-functionalized nanoparticles exhibited good dimensional stability for up to 3 months, with Dh values remaining essentially constant during this time interval. After 120 days, a slight increase in size was observed, indicating minimal change in size beyond the 3-month period.

Overall, the obtained results demonstrate that the oil-in-water microemulsion method is a reliable and reproducible approach for the preparation of PLGA nanoparticles functionalized with imidazole-based ionic liquids. The nanosystems exhibited suitable dimensions in the nanometric range, narrow size distributions, and a highly positive surface charge, all of which are key parameters for the development of efficient nanocarriers. Nanoparticles with sizes around 150–200 nm are particularly advantageous for biomedical applications, as they can promote cellular internalization while limiting rapid clearance and the low PDI values indicate a homogeneous population that is essential for reproducible biological performance [88].

The positive ζ potential values observed for both PLGA-C16 and PLGA-C10 nanoparticles can be directly attributed to the presence of the imidazolium-based ionic liquids at the nanoparticle surface. This cationic character not only contributes to electrostatic stabilization in aqueous environments, preventing aggregation over time, but also represents a relevant feature for interaction with negatively charged biological membranes and biomolecules (*i.e.*, siRNA). In particular, such surface properties are highly desirable for gene loading and delivery applications, where electrostatic interactions

between cationic carriers and anionic nucleic acids can facilitate efficient complexation and protection of genetic material.

Moreover, the comparable physicochemical properties obtained for nanoparticles functionalized with ILs bearing different alkyl chain lengths suggest that the formulation strategy is robust and adaptable. While variations in alkyl chain length may influence hydrophobic interactions, membrane affinity, and biological responses, they did not compromise nanoparticle formation or colloidal stability, indicating the possibility of fine-tuning surface characteristics without altering the overall nanosystem integrity.

Finally, the demonstrated long-term stability of the PLGA-ILs nanoparticles under refrigerated storage conditions further highlights their robustness and practical applicability. Stability over extended periods is a critical requirement for the translation of nanocarriers from laboratory-scale preparation to real-world biomedical use [89]. Taken together, these findings support the potential of imidazole-based ionic liquid–functionalized PLGA nanoparticles as versatile and stable platforms for advanced drug and gene delivery applications, warranting further investigation into their loading capacity, biological performance, and therapeutic efficacy.

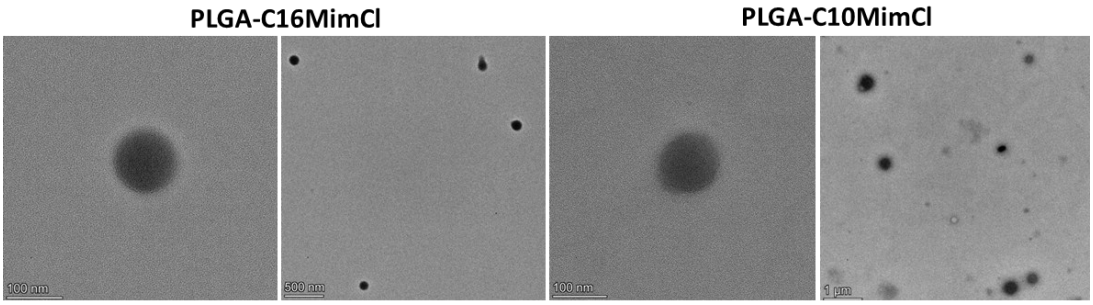

(A)

PLGA-Ils	D_h (nm)	PDI	ζ (mV)
PLGA-C16 NPs DCF	182,76 8,20 ± 8,02	0,184	+ 41,6
PLGA-C16 NPs No DCF	180,9 ± 2,77	0,10	+45,8
PLGA-C10 NPs DCF	190 ± 10,47	0,17	+ 42,7
PLGA-C10 NPs No DCF	169,9 ± 14,9	0,201	+ 45,17

(B)

Stability	90d	120d
PLGA- C16 NPs	182,77±5,83	204,77±25,87
PLGA-C10 NPs	184 ±18,74	219,77±8,16

(C)

Figure 20. Morphological and physicochemical characterization of PLGA-ILs NPs. **A)** Representative TEM morphology of PLGA-C_{16}MImCl and PLGA-C10MImCl nanoparticles. Scale bars: 100–500 nm and 1 um. **B)** Table of the average hydrodynamic dimensions, PDI, and ζ-potential of PLGA-C16 and PLGA-C10 nanoparticles, obtained by DLS analysis. Values are expressed as mean ± standard deviation (n = 3). **C) C)** Evaluation of the stability of PLGA-ILs up to 120 days.

4.3 LGlP NPs synthesis and characterization

Cationic polymer–based nanoparticles have been extensively explored for nucleic acid delivery due to their ability to electrostatically interact with negatively charged genetic material and promote cellular uptake [90]. Among these polymers, PEI is widely recognized for its high transfection efficiency, although its direct use is often limited by cytotoxicity. For example, PLGA–PEI copolymers have been successfully employed for the delivery of plasmid DNA, siRNA, and mRNA, showing improved nucleic acid complexation, enhanced cellular uptake, and higher transfection efficiency compared to non-functionalized PLGA nanoparticles. In several studies, PEI-grafted PLGA systems also demonstrated reduced cytotoxicity relative to free PEI while maintaining effective gene delivery performance, highlighting their potential for safe and efficient nucleic acid

delivery applications [46]. In this section, LGlP NPs were synthesized and characterized, confirming successful PEI conjugation.

LGlP NPs formulations were prepared using the nanoprecipitation method followed by a solvent evaporation process (**Figure 21**). LGlP polymer was dissolved in THF, dried and nanoprecipitated in nuclease-free H_2O; the organic solvent was evaporated under vacuum, and the aqueous solution was then filtered through 0.45 μm filters, obtaining a 1 mg/mL nanoparticles solution (**Figure 21A**)**.** The conjugation of PEI to PLGA was confirmed by H-NMR, which confirmed the successful conjugation of PEI by the appearance of two triplets at 3.90 and 4.36 ppm related to the protons of CH_2 groups of PEI involved in the formation of new bonds with PLGA. Other proton peaks at 1.46, 4.90, and 5.18 ppm corresponding respectively to the -CH_3, -CH_2- and -CH- protons of PLGA were observe [56] .A peak at 2.99 ppm was also found assigned to the terminal -N-CH_3 protons of PEI units. The presence of overlapping peaks given by the presence of the solvents used for NP preparation masked the presence of other distinctive PEI peaks. In addition, PLGA/PEI ratio in the final product was determined by NMR analysis. Based on the theoretical molar ratio used in the reaction feed (PLGA/PEI = 1:1), corresponding to a 10:1 ratio of PLA to PEI repeating units, NMR integration revealed a PLA/PEI ratio of approximately 20:1 in the LGlP product. This value was obtained by comparing the integrals of the characteristic –CH_3 signals of the PLA repeating units with those of the terminal –CH_3 protons of PEI, indicating an effective PLGA functionalization of approximately 50% (**Figure 21B).** FTIR spectra also showed the conjugation of PEI units to PLGA. The peak related to the bending of PEI -NH- amino groups at 1622 cm^{-1}, and the -NH- stretching band in the range 3124 - 3707 cm^{-1} were respectively visible. Less relevant was the stretching vibration of the -O-C=O ester bond in PLGA at 1745 cm^{-1}, as well as additional characteristic peaks of PLGA moieties detected in the LGlP spectrum (**Figure 21C**) [82].

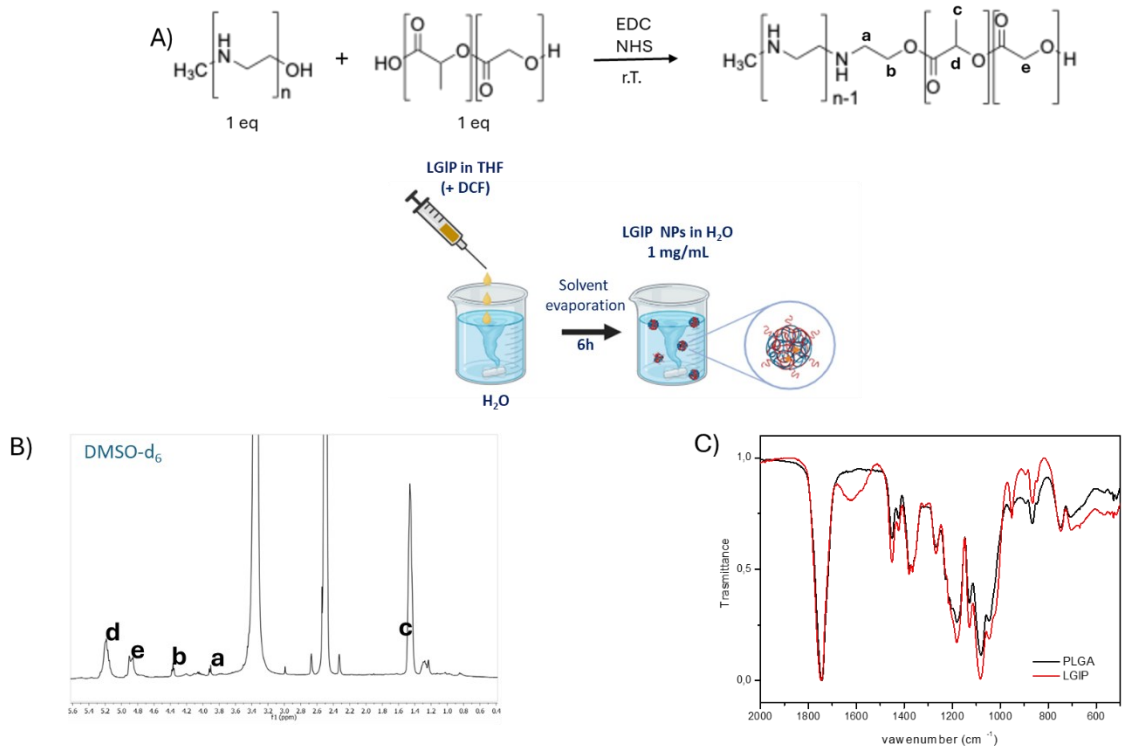

Figure 21. Synthesis and characterization of the LGlP polymer. A) Synthesis of the LGlP polymer by conjugating PLGA (75:25, 66–107 kDa) with linear PEI (4 kDa) in a 1:1 molar ratio, after activation of the terminal carboxyl group of PLGA with NHS/EDC. **B**) DMSO-d6 H NMR spectra of PLGA and the LGlP product. **C**) IR spectra of PLGA and the LGlP product: the peak at 1622 cm^{-1}, attributable to the bending of the PEI amino groups, confirms the presence of PEI in the polymer.

The combined results obtained from NMR and FTIR analyses clearly confirm the successful conjugation of PEI to the PLGA backbone, validating the synthesis of LGlP nanoparticles. The appearance of characteristic PEI proton signals in the NMR spectrum, together with the retention of PLGA-specific peaks, demonstrates that the polymer structure was preserved during functionalization. Although some PEI resonances were partially masked by solvent-related signals, the presence of diagnostic peaks associated with PEI confirms its effective incorporation into the copolymer. Quantitative NMR analysis further revealed that approximately 50% of the theoretically available PLGA chains were functionalized with PEI. This partial functionalization is consistent with previously reported PLGA–PEI systems and represents a favorable balance between achieving sufficient cationic character and maintaining biocompatibility[83]. Excessive PEI content is often associated with increased cytotoxicity, whereas moderate grafting degrees have been shown to enhance gene complexation efficiency while reducing adverse biological effects [43].

The FTIR data provide complementary evidence of PEI conjugation, particularly through the presence of –NH– bending and stretching vibrations, which are absent in native PLGA. The coexistence of PLGA ester bands and PEI-related amine signals confirms the formation of a hybrid polymer rather than a simple physical mixture.

Overall, the successful synthesis and characterization of LGlP NPs demonstrate the effectiveness of the nanoprecipitation approach for generating PEI-functionalized PLGA nanocarriers. The structural features and controlled PEI content of the LGlP system make it a promising platform for nucleic acid delivery, combining the gene-condensing capability of PEI with the biodegradability and safety profile of PLGA. These results provide a solid foundation for further studies addressing nanoparticle physicochemical properties, gene-loading efficiency, and biological performance.

LGlP nanoparticles were further characterized by transmission electron microscopy and DLS to evaluate their size, distribution, and surface charge (**Figure 22**). TEM images show spherical and well-defined nanoparticles, with a regular morphology and no significant aggregates. Direct diameter measurements verified the formation of particles within the nanoscale range, supporting their suitability for efficient siRNA delivery applications (**Figure 22A**). DLS analysis revealed an average hydrodynamic size of 117.3 ± 2.10 nm, with a polydispersity index of 0.107, indicative of a highly homogeneous population. The positive ζ potential (+41.2 ± 0.874 mV) suggests high colloidal stability, favored by the presence of the ionic liquid coating. Furthermore, no differences in size or zeta potential were detected after the presence of the fluorescent probe. This positive charge also indicates a good ability to interact with negatively charged cell membranes, favoring internalization into target cells (**Figure 22B**).Particles between 100 and 150 nm in size are able to efficiently exploit cellular endocytosis mechanisms, avoiding rapid drainage from tissues and blood and ensuring adequate residence time in target cells. Size homogeneity, confirmed by the low PDI, is a critical factor in ensuring predictable behavior in terms of internalization and release of the gene cargo, as reported in previous work on polymeric nanoparticles for RNA interference [78]. For LGIP, the stability study in aqueous solution at 4°C revealed stable dimensional behavior throughout the entire analysis. As shown in **Figure 22C**, the hydrodynamic diameter (Dh) remained essentially constant for up to 120 days, with no significant variations over time. Overall, the data indicate prolonged dimensional stability for up to four months, confirming the maintenance of LGIP size throughout the observation period**.** The positive ζ potential represents another key parameter, not only for colloidal stability but also for the efficiency of cellular internalization. The positive surface charge favors electrostatic interaction with cell membranes, which are typically negatively charged, facilitating uptake via charge-mediated endocytosis. In the literature, nanoparticles with ζ potentials above +30 mV have shown increased uptake capacity and reduced aggregation, key characteristics for RNAi

vectors [35]. These results confirm that LGlP nanoparticles possess the optimal physicochemical properties for efficient siRNA delivery: uniform nanometer size to ensure effective cellular uptake and high ζ potential to ensure colloidal stability and favorable interactions with target cells. The combination of these characteristics suggests high potential for internalization and controlled release, consistent with strategies reported in the literature for polymeric nanoparticles functionalized with cationic groups.

Figure 22. Characterization of LGlP nanoparticles (1 mg/mL). A) Representative TEM morphology of LGIP nanoparticles. Scale bars: 200 and 500 nm. **B)** The size distribution of the nanoparticles was measured by DLS, reporting the mean values of Dh, PDI, and ζ potential at different times. The data indicate that the nanoparticles maintain a stable size and positive surface charge over time, suggesting good colloidal stability. Values are expressed as mean ± standard deviation (n = 3). **C)** Evaluation of the stability of LGIP NPs up to 120 days.

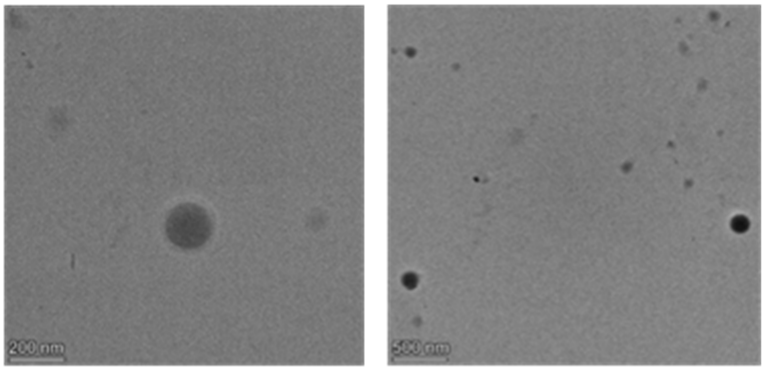

(A)

LGlP 1mg/mL	D_h (nm)	PDI	ζ (mV)
LGIP DCF	123,3 ± 2,108	0,107	+ 41,2
LGIP NO DCF	125,2 ± 0,73	0,098	+39,8

(B)

Stability	90d	120d
LGIP NPs	134,2 ±1.802	122,7 ±0.173

(C)

4.4 PLGA-ILs Nanoparticles *in vitro* biocompatibility

In vitro biocompatibility assessment is a crucial step in the development of nanoparticle-based delivery systems, as it provides preliminary information on their safety and potential biological impact prior to in vivo studies. In particular, polymeric nanoparticles functionalized with cationic groups, such as ionic liquids, require careful evaluation, as surface charge can affect cell viability, membrane integrity, and proliferation. Standardized cytotoxicity assays, conducted on both healthy and tumor cell lines, are widely used to study dose- and time-dependent cellular responses and to ensure compliance with international biocompatibility criteria [84]. In this study, the Alamar Blue assay was used to evaluate the cytocompatibility of PLGA nanoparticles functionalized with PLGA-ILs on DU145 prostate cancer cells and non-cancerous PNT2 prostatic epithelial cells. An initial screening of a large panel of ionic liquids revealed significant differences in cytotoxicity as a function of their chemical structure and concentration. Most compounds exhibited dose-dependent behavior: at low concentrations (0.025–0.1 μg/mL), cell viability was high, while higher concentrations (0.5–2 μg/mL) resulted in increased cell death, particularly for compounds with long alkyl chains or bulky benzyl substituents. Among the tested compounds, C_{10}MImCl and C_{16}MImCl exhibited a favorable cytotoxicity profile, with cell viability exceeding 70% at concentrations lower than 0.5–1 μg/mL and significant reductions only at higher doses. These results guided the selection of C_{10}MImCl and C_{16}MImCl for the functionalization of PLGA nanoparticles. Coating concentrations were quantified by UV analysis, allowing precise determination of the amount of ionic liquid adsorbed onto the surface of PLGA nanoparticles. The measured coating levels were markedly lower than the concentrations shown to induce cytotoxicity in *in vitro* assays. Under these conditions, nanoparticles functionality was preserved, and no adverse effects on healthy cells were observed. In addition, ionic liquids with intermediate alkyl chain lengths exhibited efficient adsorption onto the polymer surface and enabled controlled siRNA release [36].Consistently, DU145 and PNT-2 cells treated with PLGA–IL nanoparticles for 24 and 72 h at increasing concentrations (150–500 ng/mL and 5–100 μg/mL) exhibited cell viability values consistently above 70%. According to ISO 10993-5 guidelines, these results indicate the absence of cytotoxic effects and confirm the biocompatibility of the developed nanosystems. A moderate reduction in cell proliferation was observed at higher nanoparticle concentrations and longer exposure times; however, viability values remained within the non-cytotoxic range defined by the standard (**Figure 23 B,D**). This appears to be dose- and time-dependent, suggesting a cytostatic rather than cytotoxic response [47]. This behavior is commonly reported for cationic nanomaterials and may be associated with transient alterations in cellular metabolism or cell cycle progression rather than irreversible cell damage [59]. Importantly, the

absence of severe toxicity even at the highest concentrations tested highlights the mitigating role of the PLGA matrix, which likely attenuates the membrane-disruptive effects typically associated with highly cationic surfaces. The similar trends observed in both DU145 and PNT2 cells further indicate that the PLGA-ILs nanoparticles do not exhibit pronounced selectivity toward healthy versus cancer cells in terms of acute cytotoxicity (**Figure 23 A,C**). This is a desirable feature for nanocarriers intended for drug or gene delivery, as it suggests that the carrier itself does not induce nonspecific toxicity and that therapeutic efficacy can be primarily attributed to the loaded cargo. Moreover, the moderate reduction in proliferation at elevated concentrations could be advantageous in certain therapeutic contexts, such as cancer treatment, where a cytostatic contribution from the carrier may synergize with the delivered drug [39]. Overall, these findings are consistent with previous reports on PLGA nanoparticles functionalized with ionic liquids or other cationic moieties, which have demonstrated acceptable cytocompatibility profiles despite enhanced surface charge [52,53]. The results confirm that the incorporation of imidazole-based ionic liquids onto PLGA nanoparticles does not compromise their biocompatibility and supports their further development as safe and effective platforms for drug and gene delivery applications.

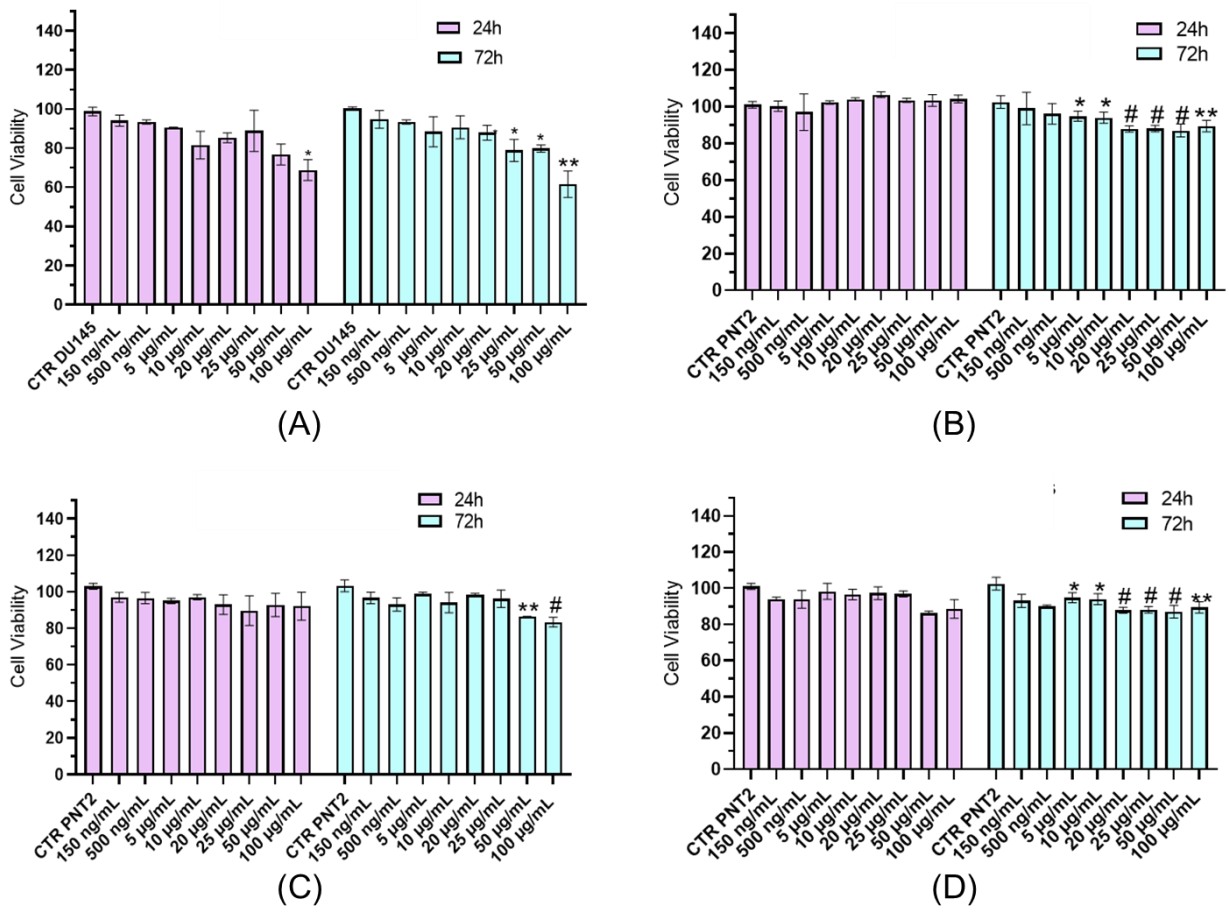

Figure 23. Biocompatibility assay on DU145 and PNT2 cells at different concentrations of PLGA-ILs NPs.
Cell viability assessment by the Alamar Blue assay after treatment with increasing concentrations (from 150 ng/mL to 100 µg/mL) of PLGA-C16 (**A, B**) and PLGA-C10 (**C, D**) nanoparticles on DU145 and PNT2 for 24 and 72 hours. Results are expressed as percentage of cell viability normalized with respect to the untreated control. Data represent the mean of three independent experiments (n = 3) ± standard deviation (SD). Statistical analysis was performed by two-way ANOVA followed by a multiple comparison post-test with respect to the control. Significance levels are indicated as follows: (*) $0.01 < p \leq 0.05$; (**) $0.001 < p \leq 0.01$; (#) $p \leq 0.001$.

4.5 LGIP Nanoparticles *in vitro* biocompatibility

While PEI is known for its high transfection efficiency, its use is often associated with dose-dependent cytotoxicity, making it essential to evaluate whether its conjugation to biodegradable polymers can effectively mitigate adverse biological effects [91]. Here, the biocompatibility of LGIP nanoparticles was assessed in DU145 and PNT2 cells after 24 and 72 hours of exposure to increasing nanoparticle concentrations (150 - 500 ng/mL and 5–100 µg/mL) (**Figure 24**). In both cell lines, a gradual decrease in metabolic activity was observed with increasing concentrations, indicating a dose-dependent response. In DU145 cells cell viability remained relatively stable at low and intermediate concentrations (150-500 ng/mL and 5-50 ug/mL), with a more pronounced reduction only at the highest doses tested (100 µg/mL) (**Figure 24A**). Importantly, even after 72 hours of treatment, viability values remained above the cytocompatibility threshold, indicating the absence of severe cytotoxic effects. A similar trend was observed in PNT2 cells, where a progressive but moderate reduction in viability was observed at higher concentrations (50–100 µg/mL), particularly after prolonged exposure (**Figure 24B**). Overall, the data indicate that LGIP nanoparticles are well tolerated by both prostate cancer and healthy cells over a broad concentration range.

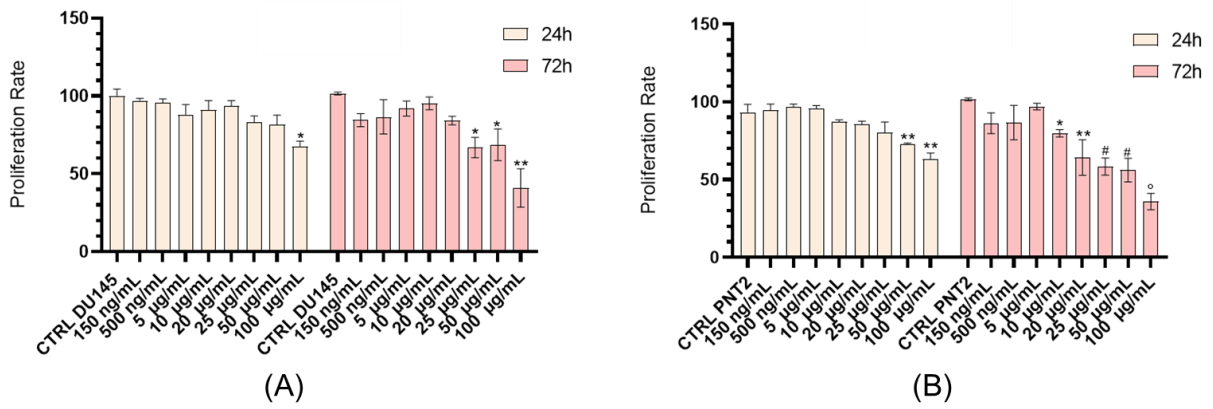

Figure 24. Biocompatibility assay on DU145 and PNT2 cells at different concentrations of LGIP NPs. Cell viability of **A)** DU145 and **B)** PNT2 cells treated with increasing concentrations of LGIP NPs for 24 and 72 hours; Results are expressed as percentage of normalized cell proliferation compared to untreated control. Data are presented as mean ± SD. Statistical analysis was performed using two-way ANOVA, comparing different time points with respect to control. Levels of significance are indicated as follows: (*) $0.05 < p \leq 0.10$; (**) $0.01 < p \leq 0.05$; (#) $0.001 < p \leq 0.01$; (°) $p \leq 0.001$. Experiments were conducted in independent triplicates (n = 3).

The observed dose-dependent reduction in metabolic activity is consistent with the presence of cationic PEI moieties on the nanoparticle surface, which are known to interact with cellular membranes and influence cellular metabolism. However, the maintenance of cell viability above the cytocompatibility threshold even at the highest concentrations tested indicates that PEI conjugation to the polymeric backbone effectively mitigates the severe cytotoxicity commonly associated with free PEI [55,56].

The relatively stable viability observed at low and intermediate concentrations suggests that LGIP nanoparticles can be safely employed within a therapeutically relevant dosing window. This is particularly important for gene delivery applications, where efficient nucleic acid complexation and cellular uptake often require positively charged carriers. The more pronounced decrease in viability observed at the highest nanoparticle concentrations and extended exposure times likely reflects a cytostatic effect rather than acute cytotoxicity, potentially arising from transient membrane interactions or altered metabolic activity. Notably, the similar response patterns observed in DU145 and PNT2 cells indicate that LGIP NPs do not induce selective toxicity toward healthy cells, which is a critical requirement for translational applications. The slightly higher sensitivity observed after prolonged exposure in PNT2 cells may be attributed to differences in proliferation rates or membrane composition between healthy and cancerous cells, as previously reported for cationic nanomaterials [59]. Overall, these findings confirm that LGIP nanoparticles combine the advantageous gene-condensing properties of PEI with the biocompatibility of biodegradable polymers, resulting in a nanosystem that is both effective and well tolerated. The demonstrated cytocompatibility over a broad concentration range supports further investigation of LGIP nanoparticles in gene loading, transfection efficiency, and functional biological studies, ultimately reinforcing their potential as safe and versatile platforms for nucleic acid delivery.

4.6 Cellular uptake of PLGA-ILs nanoparticles

Efficient cellular uptake is a critical prerequisite for the successful application of nanoparticle-based delivery systems, particularly in the context of drug and gene delivery [92]. The internalization process is strongly influenced by nanoparticle physicochemical properties such as size, surface charge, hydrophobicity, and surface functionalization. In particular, the presence of cationic and amphiphilic moieties on the nanoparticle surface can enhance interactions with the negatively charged plasma membrane, thereby promoting cellular association and internalization [93]. Therefore, investigating the uptake kinetics and intracellular behavior of PLGA nanoparticles functionalized with imidazole-based ionic liquids is essential to understand how variations in alkyl chain length affect cellular interactions. Cellular internalization of PLGA-ILs nanoparticles was assessed in DU145 cells by confocal microscopy and flow cytometry (**Figure 25**). The cellular uptake evaluated by confocal microscopy was conducted using DCF-labelled PLGA-C16 and PLGA-C10 nanoparticles, at concentrations of 150 ng/mL, 500 ng/mL, and 10 µg/mL. Cells were treated with NPs for 6, 24, 48 and 72 hours, fixed and fluorescently labelled with CellMask™ Plasma Membrane Stains Deep Red, a plasma membrane marker. Fluorescence imaging demonstrated a clear difference in the interaction kinetics of PLGA–C16 and PLGA–C10 nanoparticles with the plasma membrane. PLGA–C16 nanoparticles displayed rapid membrane association, becoming detectable after 24 h at the lowest concentrations tested (150 and 500 ng/mL), and as early as 6 h at the highest concentration (10 µg/mL) (**Figure 25A**). In contrast, PLGA–C10 nanoparticles exhibited markedly slower interaction kinetics: at low concentrations (150–500 ng/mL), membrane association and internalization were predominantly observed only after 72 h, while at 10 µg/mL these processes occurred earlier, within 24–48 h. Overall, these results indicate that the longer alkyl chain length of C16 accelerates nanoparticle–membrane interactions compared to C10, leading to faster cellular association and uptake. (**Figure 25B**). Nanoparticles internalization was further quantified by flow cytometry. PLGA–C16 nanoparticles exhibited a clear time- and concentration-dependent uptake profile, with internalization detectable as early as 6 h even at the lowest concentrations tested (150–500 ng/mL), and reaching a plateau at concentrations ≥10 µg/mL (**Figure 25C**). In contrast, PLGA–C10 nanoparticles displayed markedly slower and less concentration-dependent internalization kinetics. No clear dose- or time-dependent trend was observed at intermediate concentrations (10–50 µg/mL), while at low concentrations (150–500 ng/mL) internalization became detectable only after 72 h. These results quantitatively confirm the faster cellular uptake kinetics of PLGA–C16 nanoparticles compared to PLGA–C10 nanoparticles. (**Figure 25D**).

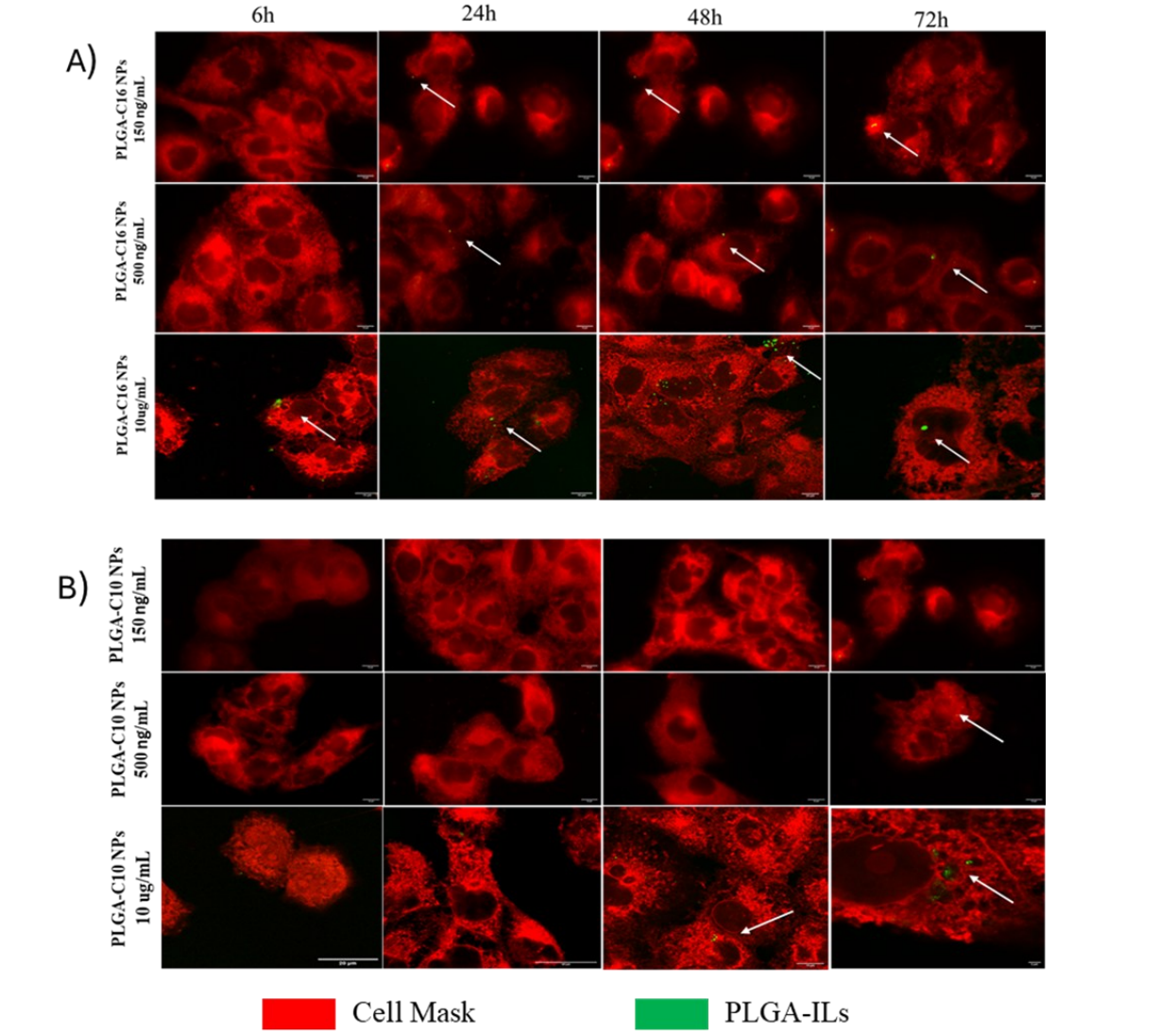
6h
24h
48h
72h
A)
PLGA-C16 NPs 150 ng/mL
PLGA-C16 NPs 500 ng/mL
PLGA-C16 NPs 10ug/mL
B)
PLGA-C10 NPs 150 ng/mL
PLGA-C10 NPs 500 ng/mL
PLGA-C10 NPs 10 ug/mL
Cell Mask
PLGA-ILs

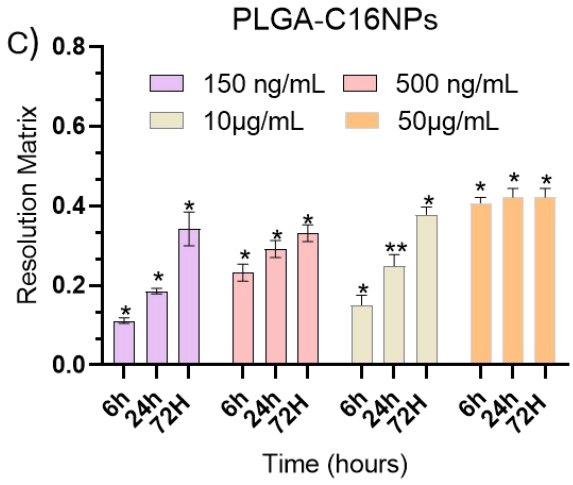
C)
PLGA-C16NPs
150 ng/mL
500 ng/mL
10µg/mL
50µg/mL
Resolution Matrix
0.0
0.2
0.4
0.6
0.8
6h
24h
72H
Time (hours)

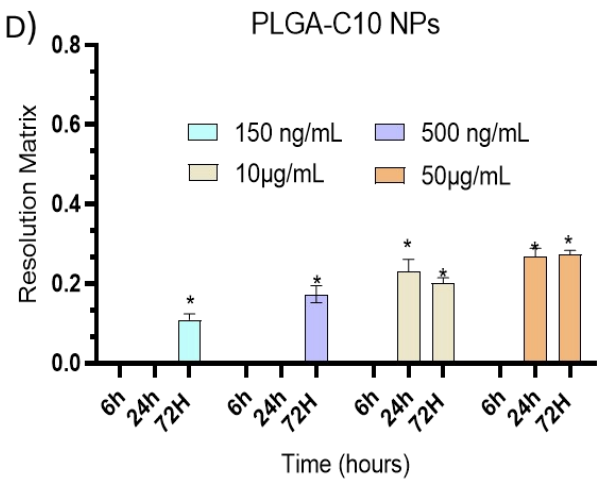
D)
PLGA-C10 NPs
150 ng/mL
500 ng/mL
10µg/mL
50µg/mL
Resolution Matrix
0.0
0.2
0.4
0.6
0.8
6h
24h
72H
Time (hours)

Figure 25. Cellular internalization of PLGA-ILs nanoparticles in DU145 cells analyzed by confocal microscopy and flow cytometry. A) Confocal morphological analysis of PLGA-C16 NPs containing DCF at concentrations of 150 ng/mL, 500 ng/mL, and 10 µg/mL, incubated for up to 72 h. PLGA-C16 (green) showed interaction with the plasma membrane already after 6–24 h, with complete internalization at 72 h. The plasma membrane was stained with CellMask Deep Red (red). Scale Bar: 10 µm. Images were acquired using a 63× oil immersion objective. **B)** Confocal microscopy of PLGA-C10 NPs reveals that uptake is limited at low concentrations (150–500 ng/mL) and becomes more pronounced at higher concentration (10 µg/mL) after 72 h. **C,D**) Flow cytometry results corroborate these observations, showing detectable internalization primarily at 10 µg/mL and limited uptake at lower concentrations. Data are reported as the median of the distribution of cellular fluorescence intensity (resolution matrix) from 10,000 gated cells, normalized to control expressed as mean ± SD. Statistical significance was assessed by t-test: (*) $0.05 < p \leq 0.1$; (**) $0.01 < p \leq 0.05$. Experiments were performed in independent triplicate (n = 3).

PLGA-C16 NPs, bearing a longer hydrophobic alkyl chain, exhibited faster and more efficient cellular uptake across all tested concentrations. Early membrane association and internalization observed even at low nanoparticle concentrations and short incubation times suggest strong hydrophobic and electrostatic interactions with the plasma membrane. These interactions likely facilitate membrane adsorption and subsequent internalization through endocytic pathways. The plateau observed at higher concentrations may indicate saturation of cellular uptake mechanisms, a phenomenon commonly reported for cationic nanocarriers [94].In contrast, PLGA-C10 NPs exhibited slower internalization kinetics, especially at lower concentrations, and required prolonged exposure times to achieve detectable uptake. This effect is likely due to the shorter alkyl chain length.The shorter chain, reducing hydrophobic interactions with the lipid bilayer, may lead to weaker membrane affinity and delayed internalization. The absence of a clear dose-dependent trend at intermediate concentrations further suggests that uptake of PLGA-C10 nanoparticles is less efficient and may rely on slower, nonspecific endocytic processes [95]. Importantly, the efficient internalization observed for PLGA-C16 nanoparticles aligns well with their favorable biocompatibility profile, indicating that enhanced uptake does not come at the expense of increased cytotoxicity. These results also underscore the importance of surface chemistry in dictating cellular interactions. The faster and more efficient internalization of PLGA-C16 nanoparticles suggests their greater potential for intracellular drug or gene delivery applications, while the tunable uptake kinetics offered by varying the alkyl chain length provides a valuable strategy for optimizing nanoparticle design according to specific therapeutic requirements.

4.7 Endocytic pathways of PLGA-ILs nanoparticles internalization

Following cellular uptake, the specific endocytic pathways by which nanoparticles enter cells play a crucial role in determining their intracellular fate, including trafficking, endosomal escape, and ultimately therapeutic efficacy [96]. Different internalization mechanisms, such as clathrin-mediated endocytosis (CME) and macropinocytosis, are known to be influenced by nanoparticle size, surface charge, hydrophobicity, and concentration. Identifying the dominant endocytic routes is particularly important for gene delivery applications, as these pathways can significantly impact nucleic acid release into the cytosol and subsequent biological activity [94]. In this context, the endocytic mechanisms involved in the internalization of PLGA-ILs were investigated using pharmacological inhibitors specific to major endocytic pathways.

The endocytic pathway involved in PLGA-ILs NPs internalization was studied by flow cytometry on DU145 using specific inhibitors of endocytic pathways: pitstop2, an inhibitor of CME, and amiloride, an inhibitor of micropinocytosis (**Figure 26**). Interestingly, treatment with Pitstop2 reduced the uptake of PLGA-C16 NPs at 10 µg/mL, suggesting that at this concentration internalization occurs predominantly via CME. This pathway is typically associated with nanoparticles of smaller effective size and well-defined surface properties, which may be favored by the longer alkyl chain of the C16 ionic liquid. At higher concentrations (50 µg/mL), PLGA-C16 nanoparticles exhibited a plateau in uptake that was not markedly affected by endocytic inhibitors (**Figure 26A**), potentially reflecting saturation of CME machinery or the engagement of multiple internalization mechanisms that compensate for pathway inhibition. For PLGA-C10 NPs, the reduction with Pitstop2 was minimal and significant only at higher concentrations (50 µg/mL), indicating a reduced reliance on clathrin-dependent uptake. In contrast, amiloride caused a significant reduction in internalization only for PLGA-C10 NPs at 50 µg/mL, indicating that micropinocytosis substantially contributes to their cellular entry at higher concentrations (**Figure 26B**). The significant decrease in internalization observed upon amiloride treatment at 50 µg/mL suggests that micropinocytosis plays a major role in the uptake of PLGA-C10 nanoparticles at higher concentrations. Micropinocytosis is a non-specific, actin-driven process often triggered by higher nanoparticle loads or surface features that promote membrane ruffling, which may be more pronounced for nanoparticles incorporating shorter alkyl chain ionic liquids.

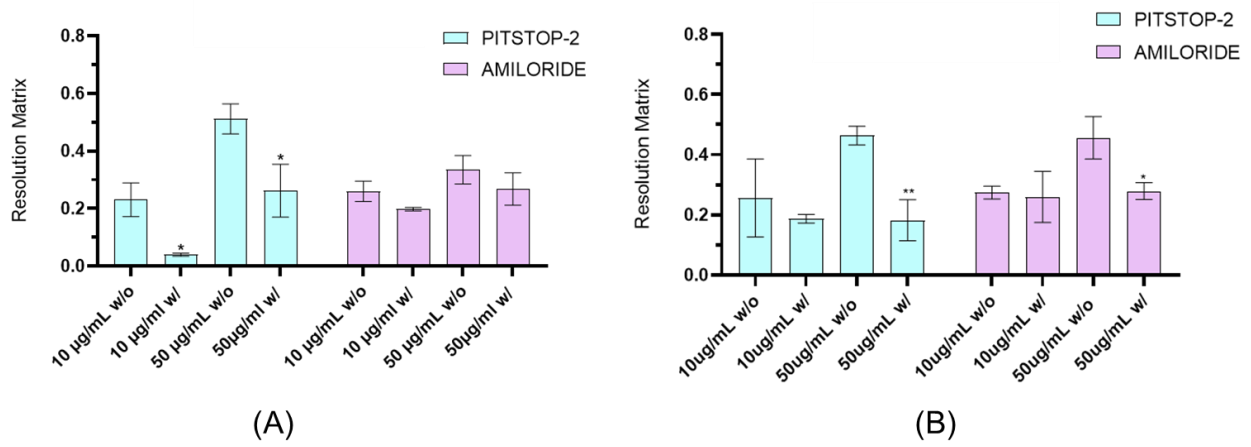

Figure 26. Cellular internalization of PLGA-ILs nanoparticles in DU145 cells assessed by flow cytometry in the presence of the inhibitors Pitstop2 and Amiloride. A) For PLGA-C16 NPs, Pitstop2 reduced uptake at 10 µg/mL, while a plateau was observed at all time points at 50 µg/mL. For PLGA-C10 NPs, the reduction with Pitstop2 was significant only at 50 µg/mL. **B)** The inhibitor Amiloride significantly reduced internalization only at 50 µg/mL, indicating the involvement of macropinocytosis at high concentrations. The results obtained by flow cytometry are reported as the median of the distribution of cellular fluorescence intensity (Resolution matrix), obtained by analyzing 10,000 cells in the gate and normalized to the control. The data are expressed as M ± SD. The t-test was used to compare the data. The levels of statistical significance are indicated as follows: (*) $0.05 < p \leq 0.1$; (**) $0.01 < p \leq 0.05$. The experiment was conducted in independent triplicate (n = 3).

The endocytic pathway analysis provides important mechanistic insight into how ionic liquid functionalization governs nanoparticle–cell interactions beyond simple uptake efficiency. The preferential involvement of CME for PLGA-C16 NPs at lower concentrations suggests a more organized and receptor-associated internalization process. CME is often linked to well-defined nanoparticle surfaces and sizes compatible with clathrin-coated vesicle formation, typically around 100–200 nm [94]. The enhanced hydrophobicity and stronger membrane affinity conferred by the longer C16 alkyl chain likely promote stable membrane adsorption and clustering at endocytic pits, facilitating efficient CME-driven uptake. The saturation behavior observed at higher PLGA-C16 NPs concentrations indicates that cellular uptake mechanisms can become limited by the availability of endocytic machinery. Under such conditions, additional uptake routes may be recruited, or internalization may be constrained by membrane processing capacity, resulting in a plateau effect that is relatively insensitive to pathway inhibition. This phenomenon has been widely reported for cationic nanocarriers and reflects the dynamic and adaptive nature of cellular internalization mechanisms in response to nanoparticle load [96]. In contrast, the uptake of PLGA-C10 NPs appears to rely more strongly on macropinocytosis at elevated concentrations. Macropinocytosis is a less selective, energy-dependent pathway characterized by membrane ruffling and the formation of large vesicles, often

induced by high concentrations of nanoparticles or surface features that promote membrane perturbation rather than organized receptor engagement [97]. The shorter alkyl chain of the C10 ionic liquid may result in weaker hydrophobic interactions and less efficient recruitment of clathrin-mediated pathways, shifting uptake toward macropinocytic mechanisms when nanoparticle concentration increases. These differences in internalization pathways are highly relevant for gene delivery applications. CME often leads to well-regulated intracellular trafficking but may involve tighter endosomal confinement, whereas macropinocytosis can result in larger vesicles with distinct maturation pathways that may favor endosomal escape under certain conditions [97]. Therefore, the ability to modulate endocytic routing through ionic liquid structure and nanoparticle concentration offers a powerful strategy to optimize intracellular delivery outcomes. Taken together, these results demonstrate that even subtle variations in ionic liquid alkyl chain length can significantly alter the cellular entry routes of PLGA-ILs NPs, with important implications for intracellular trafficking, endosomal escape, and ultimately gene silencing efficacy. Such insights are essential for the rational design of next-generation PLGA-ILs nanocarriers tailored for efficient and controlled siRNA delivery.

4.8 Cellular uptake of LGIP nanoparticles

A detailed investigation of the internalization profile of LGIP NPs was carried out to assess their suitability as gene delivery platforms. Cellular internalization of LGIP NPs was assessed in DU145 cells by confocal microscopy and flow cytometry (**Figure 27**). The cellular uptake evaluated by confocal microscopy was conducted using DCF-labelled LGIP NPs, at concentrations of 150 ng/mL, 500 ng/mL, and 10 µg/mL, incubated with cells for up to 72 hours. LGIP NPs primarily associated with the plasma membrane after prolonged incubation times, becoming evident only after 72 hours (**Figure 27A**). This delayed interaction may reflect limited nanoparticle availability at the cell surface or a slower uptake process at sub-microgram concentrations. In contrast, at the highest concentration tested by confocal microscopy (10 µg/mL), LGIP nanoparticles start to be internalized by cells, indicating that increased local nanoparticle concentration facilitates cellular engagement and uptake. Internalization was also assessed quantitatively by flow cytometry. LGIP NPs showed a peak internalization at 72 hours for a concentration of 10 µg/mL. A similar behavior was also observed for concentrations in the nanogram range (**Figure 27B**). Quantitative flow cytometry analysis further supported these observations, revealing maximal internalization at 72 hours for LGIP nanoparticles at 10 µg/mL.

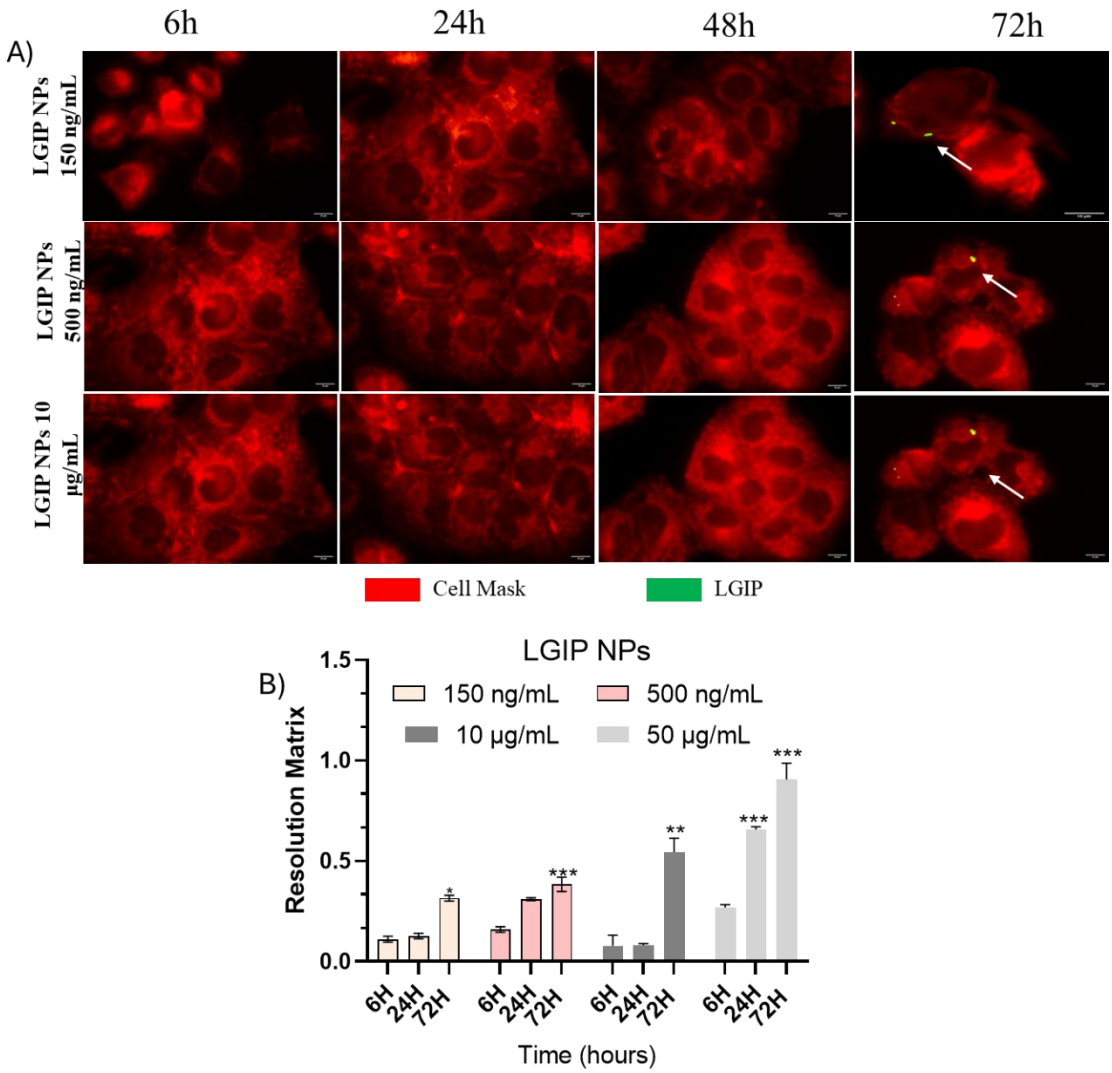

Figure 27. Analysis of LGIP NPs internalization in DU145 cells by confocal microscopy and flow cytometry. Cells were incubated with fluorescent LGIP NPs (in the presence of DCF) at concentrations of 150 ng/mL, 500 ng/mL, 10 µg/mL, and 50 µg/mL for up to 72 hours. **A)** Confocal microscopy shows that interaction of LGIP NPs (green) with the plasma membrane becomes evident after 72 hours at the lowest concentrations (150 and 500 ng/mL), while it is already marked at 10 µg/mL. The plasma membrane was stained with CellMask Deep Red (red). Scale Bar: 10 µm. Images were acquired using a 63× oil immersion objective. **B)** Flow cytometry analysis shows a time- and concentration-dependent trend at both nanogram and microgram concentrations. The results obtained by flow cytometry are reported as the median of the distribution of cellular fluorescence intensity (resolution matrix), obtained by analyzing 10,000 cells in the gate and normalized to the control. Data are expressed as (M) ± (SD). Two-way ANOVA was used to compare data. Statistical significance levels are indicated as follows: (*) $0.05 < p \leq 0.1$; (°) $p \leq 0.001$. The experiment was conducted in independent triplicates (n = 3).

The uptake profile of LGIP nanoparticles reveals a distinct internalization behavior compared to ionic liquid–functionalized PLGA nanoparticles, characterized by slower kinetics and a stronger dependence on prolonged exposure. This behavior can be attributed to the physicochemical features of LGIP nanoparticles, including their polymeric composition and the nature of PEI conjugation, which may result in a more moderate surface charge and reduced immediate membrane interaction. Such characteristics can limit rapid adsorption to the plasma membrane while promoting gradual accumulation at the cell surface over time.

Overall, these results highlight the importance of both exposure time and nanoparticles concentration in governing LGIP nanoparticle internalization. The observed delayed but uptake profile may be advantageous for gene delivery applications requiring prolonged cellular exposure, potentially enabling continuous intracellular delivery of nucleic acids while minimizing acute cytotoxic effects. Furthermore, understanding these uptake dynamics is critical for optimizing dosing strategies and predicting intracellular bioavailability, particularly in the context of siRNA delivery where efficient internalization is a prerequisite for effective gene silencing.

4.9 Endocytic pathways of LGIP nanoparticles internalization

Polyethylenimine is known to promote cellular internalization through multiple mechanisms due to its high cationic charge density and ability to interact with the plasma membrane. When PEI is conjugated to biodegradable polymers, such as in LGIP NPs, the resulting hybrid systems may engage different internalization routes depending on nanoparticle concentration and surface characteristics [98]. The effect of inhibitors of key endocytic pathways on LGIP NPs internalization was assessed by flow cytometry. DU145 cells were treated with LGIP NPs at concentrations of 10 µg/mL and 50 µg/mL. Treatment with Pitstop-2 resulted in a pronounced and significant reduction in nanoparticles uptake at both tested concentrations, indicating that LGIP NPs internalization occurs predominantly through a clathrin-dependent pathway. Amiloride, also caused a marked reduction in internalization at 10 and 50 µg/mL, suggesting that macropinocytosis also contributes substantially to LGIP NPs cellular entry (**Figure 28**).

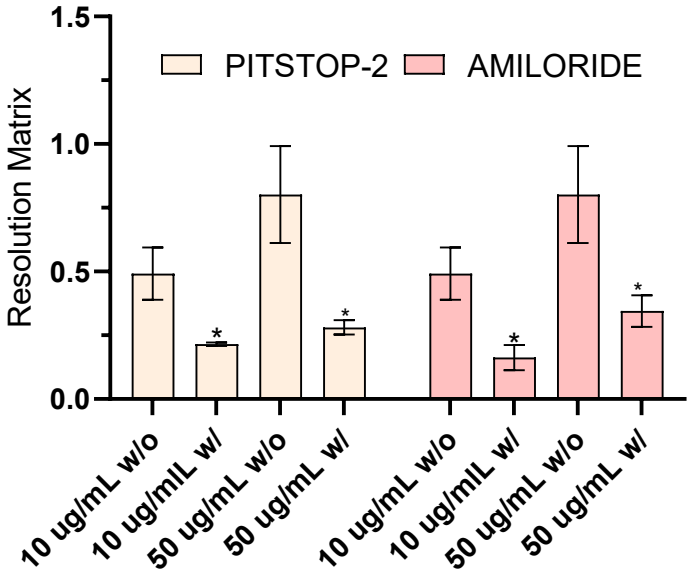

Figure 28. Effect of endocytic pathway inhibitors on LGIP NP internalization in DU145 cells. Cells were treated with Pitstop-2 and amiloride at concentrations of 10 and 50 µg/mL of LGIP NPs, by flow cytometry. The graph shows a significant reduction in internalization in the presence of Pitstop-2 at both concentrations, suggesting a predominant role for clathrin-mediated endocytosis. Amiloride also significantly reduced uptake, indicative of the contribution of macropinocytosis, especially at 10 µg/mL. Values are expressed as mean ± SD; the asterisk indicates statistically significant differences compared to the control without the inhibitor ($p < 0.05$).

The inhibitor studies provide valuable insights into the cellular internalization pathways of LGIP nanoparticles, revealing the involvement of multiple endocytic routes. The strong reduction in nanoparticle uptake observed upon Pitstop-2 treatment indicates that CME plays a major role in LGIP internalization across the tested concentration range. The significant contribution of macropinocytosis, as evidenced by the inhibitory effect of amiloride, suggests that LGIP NPs also exploit non-specific, actin-driven uptake mechanisms. This dual uptake behavior is commonly reported for PEI-based systems and reflects their ability to interact strongly with the plasma membrane, inducing membrane ruffling and facilitating macropinosome formation [92] The involvement of macropinocytosis at both 10 and 50 µg/mL indicates that LGIP nanoparticles can trigger this pathway even at moderate concentrations, likely due to the presence of protonable amine groups on PEI that promote membrane perturbation. The coexistence of these pathways therefore suggests that LGIP NPs possess a versatile internalization profile capable of enhancing intracellular

trafficking and cytosolic delivery. Overall, these findings demonstrate that PEI conjugation to PLGA not only improves biocompatibility but also preserves the ability of PEI to exploit multiple endocytic routes. Understanding the relative contribution of these pathways provides important guidance for the rational design and optimization of LGIP nanoparticles, particularly in tailoring surface properties and dosing strategies to maximize gene delivery efficiency while minimizing cytotoxic effects.

4.10 Evaluation of siRNA release from PLGA-ILs and LGIP nanoparticles

The efficacy of siRNA-mediated gene silencing depends not only on cellular internalization but also on the controlled release of siRNA from the nanoparticle carrier. An optimal release profile ensures enough functional siRNA in the cytosol, avoiding premature or extracellular release that could reduce therapeutic efficacy. Therefore, evaluating the release of siRNA from different nanoparticle formulations is crucial for interpreting gene silencing results [48,99]. For PEI-containing LGIP nanoparticles, two polymer/siRNA ratios were tested, designated LGIP-1 (1:1) and LGIP-10 (10:1). Modulating the polymer/siRNA ratio is a well-established strategy in PEI-based systems to regulate particle stability, cellular uptake, endosomal escape, and cytotoxicity. The use of LGIP-10 allowed us to evaluate whether a higher polymer content could favor an increase in siRNA release, while maintaining a biocompatibility profile compatible with the cells under study. This experimental strategy therefore allowed to directly compare two formulations with different polymer/siRNA ratios, providing useful information to optimize the composition of the nanoparticles in relation to the efficacy of gene silencing. The GOLPH3-specific siRNA pool was initially complexed with PLGA-ILs, LGIP-1, and LGIP-10 nanoparticles. The resulting siRNA-loaded formulations were maintained under continuous stirring in aqueous solution at room temperature for 2, 24, and 72 hours to evaluate the time-dependent release profile of siRNA. The release study was preliminarily conducted in water to provide a controlled and simplified environment for assessing intrinsic release. Furthermore, PLGA-based polymer systems are conventionally protected in aqueous media during in vitro release studies as this approach allows for reproducible analysis of diffusion- and degradation-driven release mechanisms before testing them under more physiologically relevant conditions [100]. At each predetermined time point, a 10 μL aliquot was collected to quantify the released siRNA using the PicoGreen fluorescence assay. The analysis was extended up to 72 hours, as significant GOLPH3 gene silencing was observed at this time point in cellular experiments. Accordingly, the release study was concluded at 72 hours to align the in vitro release profile with the onset of the biological effect, thereby facilitating correlation between siRNA release and functional gene silencing outcomes. Therefore, the release study was terminated at 72 hours, corresponding to the time at which the biological effect of the siRNA was detected (**Figure 29**). This approach enabled monitoring of siRNA

release from the different formulations, revealing significant differences among the nanoparticles. The release profiles further highlight the influence of ionic liquid structure on siRNA nanoparticles interactions. Both PLGA–C16 and PLGA–C10 nanoparticles exhibited a biphasic release pattern, characterized by an initial burst within the first 24 h followed by a slower, sustained release up to 72 h. However, notable differences in release were observed between the two formulations. PLGA–C16 nanoparticles showed a more pronounced initial release, which can be attributed to the higher hydrophobicity and longer alkyl chain of the C16 ionic liquid. These structural features are likely to promote stronger interactions with the PLGA surface, while simultaneously facilitating dynamic electrostatic interactions with siRNA at the nanoparticle interface. As a result, a fraction of siRNA associated with the ILs-coated surface may be more readily desorbed upon exposure to the aqueous environment.

In contrast, PLGA–C10 nanoparticles displayed a comparatively more controlled release behavior, suggesting a more balanced interaction between siRNA and the ionic liquid coating. The shorter alkyl chain of C10 likely results in reduced hydrophobic packing at the nanoparticle surface, favoring more stable electrostatic complexation of siRNA and limiting premature desorption. This interpretation is consistent with the slower cellular uptake observed for PLGA–C10 nanoparticles and supports the notion that alkyl chain length plays a key role in modulating both membrane interaction and cargo release.

Overall, these findings indicate that while both formulations are capable of effectively complexing and releasing siRNA, PLGA–C10 nanoparticles may offer a more controlled and sustained release profile, whereas PLGA–C16 nanoparticles favor faster release and cellular interaction. This tunability underscores the relevance of ionic liquid structural design in optimizing nanoparticle-based siRNA delivery systems, allowing a balance between release, cellular uptake, and biocompatibility to be achieved [30].

In contrast, LGIP-1 nanoparticles exhibited a qualitatively similar release profile but with a lower overall amount of siRNA released over time. This behavior can be attributed to the stronger electrostatic interactions between PEI and siRNA, which promote efficient nucleic acid condensation and increase complex stability, thereby delaying siRNA dissociation. The high charge density of PEI results in tight polyplex formation, reducing the fraction of siRNA readily available for diffusion from the carrier. An even more pronounced retention effect was observed for LGIP-10 complexes, characterized by a high polymer-to-siRNA ratio. These formulations released minimal amounts of siRNA over the 72 h period, indicating the formation of highly compact and dense structures. The excess PEI enhances electrostatic binding with siRNA, stabilizing the complexes and significantly limiting both the diffusion and mobility of the nucleic acid within the polymer matrix. As a

consequence, siRNA release is substantially delayed. This behavior is consistent with previous reports on PEI-based delivery systems, in which increasing the polymer-to-siRNA ratio improves complex stability and protection of the cargo but compromises release.

When compared with PLGA–ILs-based nanoparticles, which exhibited a more balanced and tunable release profile driven by reversible electrostatic interactions between siRNA and the ionic liquid coating, PEI-rich LGIP formulations appear to favor complex stability at the expense of timely siRNA release. This comparison highlights the advantage of PLGA–ILs systems in achieving a compromise between sufficient siRNA retention and controlled release, a feature that is critical for effective intracellular gene silencing [55].

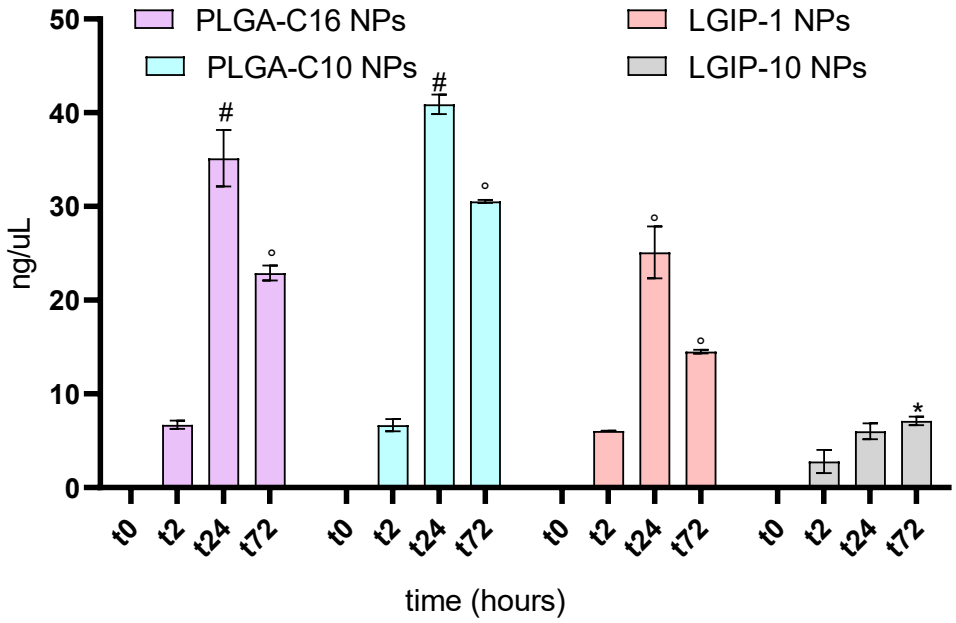

Figure 29. siRNA release from different PLGA nanoparticles over time. Release profiles of siRNA from PLGA-C16 NPs, PLGA-C10 NPs, LGIP-1 NPs, and LGIP-10 NPs were measured at 0, 2, 24, and 72 hours and expressed as ng/µL. PLGA-C16 NPs shows a rapid initial release, reaching a plateau at 24–72 h, whereas PLGA-C10 NPs exhibits a delayed release, peaking at 24–72 h. LGIP-1 and LGIP-10 NPs display intermediate release. Data are presented as mean ± SD. Statistical significance is indicated as follows: (#, °, *) corresponding to p-values reported in the main text.

4.11 PLGA-ILs and LGIP nanoparticles-mediated GOLPH3 silencing

Polymeric nanoparticles functionalized with ionic liquids or cationic polymers have shown potential to enhance siRNA delivery through tailored surface properties and optimized internalization

pathways. For example, siRNA-mediated silencing of GOLPH3 using lipid-based nanoparticles, polymeric nanocarriers, and PEI-based delivery systems have been shown to inhibit cancer cell proliferation, impair Golgi function, and reduce tumor growth in prostate and other solid tumor models, highlighting the therapeutic potential of nanoparticle-assisted GOLPH3 knockdown [11]. Here, the gene silencing efficacy of different formulations of PLGA-ILs and LGIP NPs loaded with anti-GOLPH3 siRNA was evaluated in DU145 cells by quantitative (RT-PCR) and qualitative (fluorescence microscopy) molecular analyses (**Figure 30**). Cells were treated with PLGA-C16, PLGA-C10, LGIP-1 and LGIP-10 nanoparticles for 48 and 72 hours, including Lipofectamine/siRNA complex (positive) and untreated cells (CTRL DU145, negative) as controls. The LGIP-10 NPs, characterized by a higher PEI content compared to LGIP-1, was designed to evaluate whether an increase in polymer content could improve nanoparticle condensation and stability, protecting the siRNA from extracellular degradation and promoting its internalization into target cells. However, in similar systems, excessive PEI can generate excessively strong electrostatic interactions between the polymer and siRNA, slowing their intracellular release and reducing the effectiveness of gene silencing [27]. RT-PCR analysis showed a significant reduction in GOLPH3 mRNA levels in cells treated with PLGA-C16, LGIP-1, and Lipofectamine/siRNA at both 48 and 72 hours, indicating effective silencing. In comparison, PLGA-C10 NPs caused a moderate decrease in gene expression, while LGIP-10 induced no appreciable changes compared to controls (**Figure 30A**). Fluorescence microscopy performed after 72 h confirmed these findings at the protein level and closely reflected the differences observed in siRNA uptake and release profiles. PLGA–C16 nanoparticles, LGIP-1 nanoparticles, and Lipofectamine/siRNA complexes showed a marked reduction in GOLPH3-associated fluorescence, consistent with their rapid cellular internalization and/or efficient intracellular siRNA release. PLGA–C10 nanoparticles induced a more modest decrease in fluorescence, in agreement with their slower uptake and more controlled siRNA release profile. In contrast, LGIP-10 nanoparticles exhibited fluorescence levels comparable to untreated controls, reflecting the limited siRNA release and delayed intracellular availability observed for this formulation. (**Figure 30 B,C,D**).

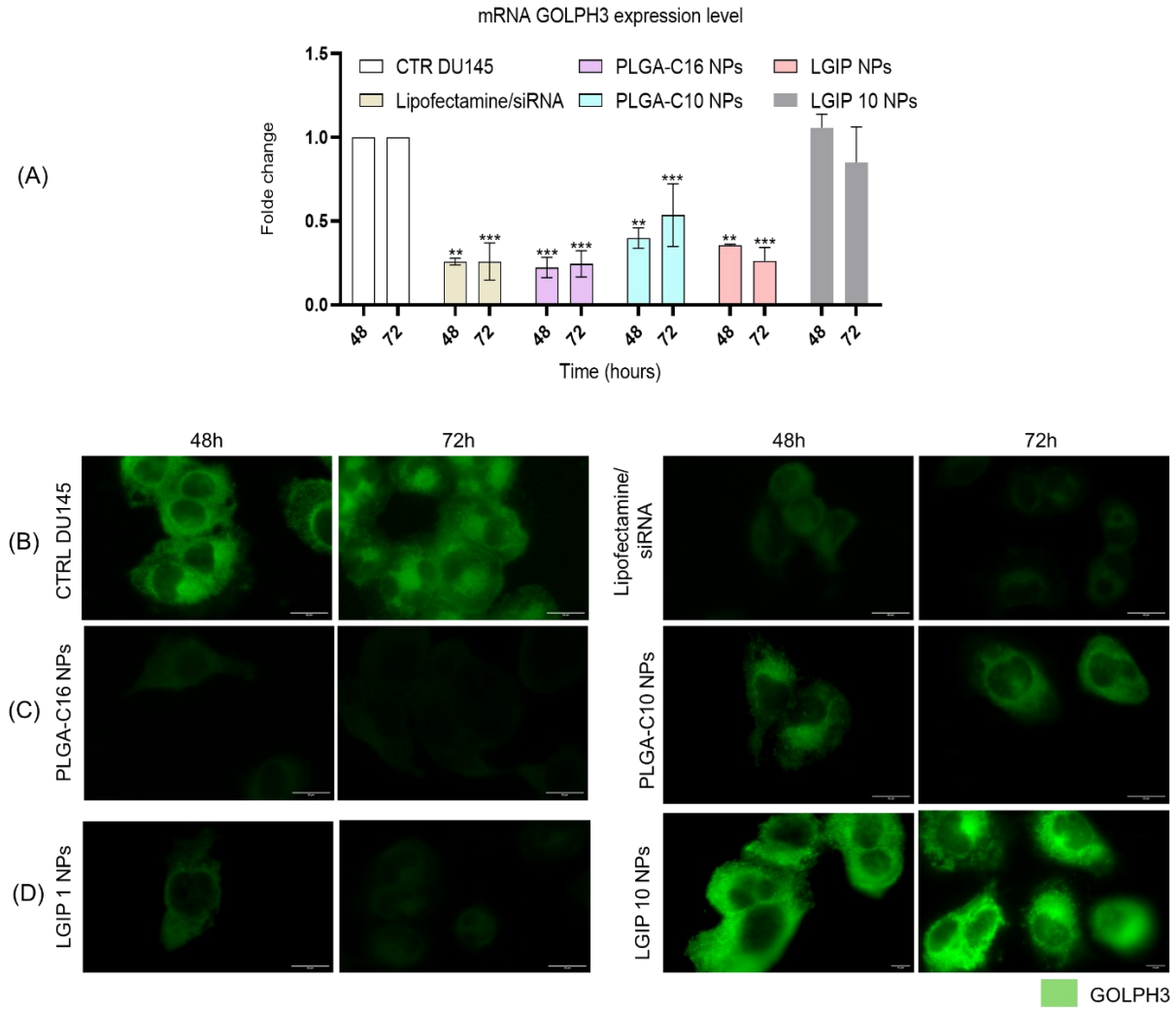

Figure 30. GOLPH3 silencing by qPCR and fluorescence microscopy. A) Quantification of GOLPH3 expression by qPCR after 48 and 72 hours of treatment with nanoparticles loaded with anti-GOLPH3 siRNA. Treatments included PLGA C16, PLGA C10, LGIP 1, LGIP 10, and Lipofectamine/siRNA complex. A significant reduction in GOLPH3 expression was observed with PLGA C16, LGIP-1 and Lipofectamine/siRNA, while PLGA C10 NPs and LGIP-10 NPs did not show a significant decrease. **B-C-D)** Fluorescence microscopy analysis after 48 and 72 hours of treatment. Cells were fixed and stained with an anti-GOLPH3 antibody (green). Scale Bar: 10 µm. Images were acquired using a 100× oil immersion objective. A marked reduction in GOLPH3 signal was observed in cells treated with PLGA C16, LGIP-1, PEI 1, and Lipofectamine/siRNA, while PLGA-C10 NPs showed only a minimal decrease and LGIP 10 NPs showed no appreciable effect. Data are normalized to the untreated CTRL and expressed as mean ± SD. Statistical significance was assessed by two-way ANOVA. Significance levels are indicated as follows: () $0.05 < p \leq 0.1$; () $0.01 < p \leq 0.05$; () $0.001 < p \leq 0.01$; (****) $p \leq 0.001$. Experiments were performed in independent triplicates (n = 3).

The gene silencing results clearly demonstrate that nanoparticle composition and surface engineering play a critical role in determining siRNA delivery efficiency. Among the tested formulations, PLGA-C16 NPs achieved robust GOLPH3 knockdown at both the mRNA and protein levels, comparable to

the performance of Lipofectamine, widely considered a reference transfection agent. This result is particularly significant given Lipofectamine's known limitations in clinical translation, including toxicity and lack of stability in physiological environments [42].

The superior performance of PLGA-C16 NPs can be directly linked to the presence of the longer-alkyl-chain imidazole-based ionic liquid, which enhances nanoparticle-membrane interactions and promotes efficient cellular uptake via clathrin-mediated endocytosis. This internalization pathway, combined with the cationic surface properties of the nanoparticles, likely facilitates endosomal destabilization and cytoplasmic release of siRNA, allowing for effective RISC engagement. Conversely, the moderate silencing effect observed with PLGA-C10 nanoparticles further highlights the importance of the ionic liquid structure in controlling biological performance. The shorter alkyl chain may result in weaker membrane interactions and slower uptake kinetics, as previously observed in internalization studies, ultimately reducing the amount of siRNA reaching the cytoplasm in an active form.

These results are consistent with what was observed in *in vitro* release experiments: formulations that showed more controlled and sustained siRNA release, such as PLGA-C16 and LGIP-1, corresponded to more effective GOLPH3 knockdown, while formulations with slower or limited release, such as PLGA-C10 and LGIP-10 NPs, showed reduced gene silencing. This confirms that siRNA release kinetics directly influences the amount of functional molecules available in the cytoplasm for activation of the RISC machinery [13,101].

Furthermore, the silencing efficacy observed for LGIP-1 nanoparticles suggests that an optimal degree of PEI functionalization is critical to balance siRNA complexation, cellular uptake, and intracellular release. A moderate PEI content may provide sufficient proton buffering capacity to promote endosomal evacuation via the proton sponge effect, while avoiding excessive cytotoxicity or intracellular trapping [25].Conversely, the lack of silencing activity observed for LGIP-10 nanoparticles may indicate excessive PEI content, leading to excessively strong siRNA binding, reduced release into the cytoplasm, or altered intracellular trafficking that limits access to the RNAi machinery [35].

Overall, these results highlight that the efficacy of gene silencing does not depend solely on cellular uptake, but rather on a finely tuned interplay between nanoparticle composition, internalization pathway, endosomal clearance, and siRNA release. The demonstrated ability of some PLGA-ILs and LGIP formulations to inhibit GOLPH3 expression underscores their potential as adaptable and efficient siRNA delivery platforms. These findings provide a solid basis for further optimization and in vivo evaluation of these nanosystems for targeted prostate cancer therapy and RNA-based therapeutic applications.

4.12 Effect of GOLPH3 silencing mediated by PLGA-ILs and LGIP nanoparticles

Cell migration is a critical process in cancer progression and metastasis, enabling tumor cells to invade surrounding tissues and disseminate to distant organs. Targeting molecular regulators of migratory behavior therefore represents an important therapeutic strategy in oncology. GOLPH3 has been implicated in the control of cancer cell migration through its role in Golgi organization, vesicular trafficking, and signaling pathways involved in cytoskeletal dynamics [102]. Functional assays that directly assess migratory capacity are essential to validate whether effective gene silencing translates into meaningful phenotypic changes. Here, a scratch assay was employed to investigate the impact of nanoparticle-mediated GOLPH3 silencing on the migratory behavior of DU145 prostate cancer cells (**Figure 31**).

DU145 cells were treated with PLGA-C16, PLGA-C10, and LGIP-1 nanoparticles loaded with anti-GOLPH3 siRNA, with Lipofectamine/siRNA complexes included as a reference transfection system. After 72 hours of treatment, a wound was generated, and wound closure was monitored after 2, 4, 8, and 24 hours (**Figure 31A**). As expected, control DU145 cells showed progressive migratory behavior, with a continuous reduction in the scratched area over time, reaching approximately 60–70% wound closure after 24 hours. In contrast, cells treated with PLGA-C16 nanoparticles showed a marked inhibition of cell migration. Minimal wound closure was observed at the earliest time points, and after 24 hours, the wound area remained largely open, with approximately 20% closure. This pronounced inhibition of cell migration closely mirrors the high GOLPH3 silencing efficiency previously observed for PLGA–C16 nanoparticles, indicating a direct functional consequence of effective gene knockdown. In contrast, PLGA-C10 NPs did not significantly affect cell migration, as treated cells exhibited wound closure kinetics comparable to those of the control group, reaching approximately 60% closure at 24 hours. This finding is consistent with the limited GOLPH3 silencing achieved with this formulation and suggests that partial or insufficient gene knockdown is not sufficient to impair migratory capacity. On the other hand, treatment with LGIP-1 NPs resulted in moderate but significant inhibition of cell migration, with wound closure reaching approximately 45–50% after 24 hours, suggesting partial suppression of migratory behavior (**Figure 31B**). The intermediate effect observed with LGIP NPs correlates with their moderate silencing efficiency and supports a dose- and formulation-dependent relationship between GOLPH3 expression levels and migratory behavior.

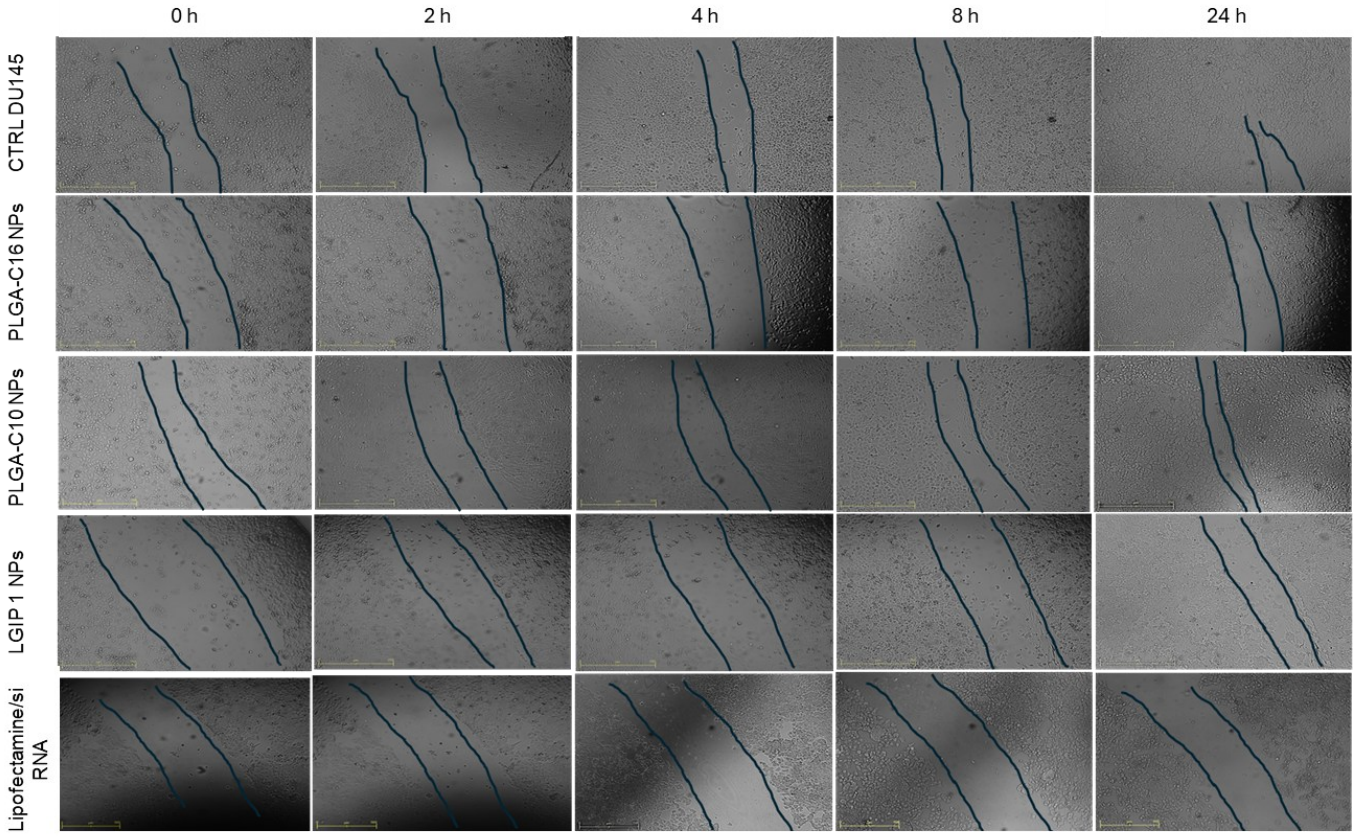

Figure 31. Evaluation of the effect of PLGA-ILs and LGIP nanoparticles on DU145 cell migration. A) Bright-field images of the scratch assay performed on DU145 cells after 72 hours of treatment with PLGA-C16, PLGA-C10, LGIP NPs, and Lipofectamine/siRNA complex containing anti-GOLPH3 siRNA. **B)** % of scratch area measured following the different treatments. PLGA-C16 strongly inhibited cell migration compared to the control, with only ~20% wound closure at 24 hours, while LGIP NPs showed moderate inhibition (~50% closure). Cells treated with PLGA-C10 migrated similarly to the control (~60% closure at 24 hours). Data are normalized to the control and expressed as mean M ± SD. Statistical analysis was performed by two-way ANOVA. Significance levels are indicated as follows: () $0.05 < p \leq 0.1$;

() 0.01 < p ≤ 0.05; () 0.001 < p ≤ 0.01; (****) p ≤ 0.001. Experiments were performed in independent triplicates (n = 3). Scale bar 200 μm.

The wound-healing assay results provide compelling functional validation of the gene silencing data, demonstrating that effective knockdown of GOLPH3 leads to a pronounced impairment of prostate cancer cell migration. Among the tested formulations, PLGA-C16 nanoparticles induced the strongest inhibitory effect, which aligns with their superior performance in cellular uptake and GOLPH3 silencing assays. This concordance underscores the importance of achieving sufficient intracellular siRNA delivery to elicit downstream phenotypic responses. The lack of an effect observed with PLGA-C10 nanoparticles further reinforces the notion that modest or incomplete gene silencing is insufficient to disrupt complex cellular processes such as migration. Cell motility is regulated by tightly coordinated signaling and trafficking events, and residual GOLPH3 expression may be adequate to maintain these functions. In contrast, the partial inhibition of migration observed with LGIP nanoparticles suggests that intermediate levels of gene knockdown can produce measurable, albeit incomplete, functional outcomes. GOLPH3 plays a central role in Golgi architecture and anterograde trafficking, processes that are essential for polarized secretion and the dynamic remodeling of the plasma membrane during migration. Reduced GOLPH3 expression likely compromises the transport of integrins, growth factor receptors, and other membrane-associated proteins required for focal adhesion turnover and cytoskeletal reorganization [103]. Additionally, GOLPH3 is linked to mTOR signaling, which regulates actin dynamics and cell motility, providing further mechanistic support for the observed migration defects. Importantly, these findings demonstrate that nanoparticle-mediated siRNA delivery can extend beyond molecular knockdown to produce meaningful functional effects relevant to cancer progression. The strong anti-migratory effect achieved with PLGA-C16 NPs highlights their potential not only as gene delivery vehicles but also as tools to modulate aggressive tumor phenotypes. Overall, this functional evidence strengthens the case for PLGA-C16 NPs and optimized LGIP-1 NPs as promising platforms for RNA-based therapeutic strategies aimed at limiting prostate cancer invasiveness and metastasis [14]

4.13 Effect of ILs on DU145 cancer spheroids

Understanding the interactions between tumor cells and the surrounding microenvironment is essential to elucidate tumor progression and develop effective therapeutic strategies. Traditionally, two-dimensional (2D) cell culture models have been widely used to assess cytotoxicity, proliferation, and drug response, as they allow rapid quantitative analyses, are cost-effective, and easily standardized for high-throughput screening. However, despite these advantages, 2D cultures have intrinsic limitations that significantly reduce their biological relevance compared to *in vivo* tissues. Cells grown on rigid, uniform substrates lose the three-dimensional polarity typical of native tissues and are exposed to homogeneous distributions of nutrients, oxygen, and growth factors. Consequently, these models fail to reproduce the structural and functional complexity of solid tumors, which are characterized by metabolic gradients, cellular heterogeneity, and dynamic interactions with the extracellular matrix and surrounding stromal cells [104]. The lack of such physiological gradients and interactions can lead to an overestimation of drug efficacy, contributing to discrepancies between 2D *in vitro* results and in vivo tumor responses [61]. To overcome these limitations, three-dimensional (3D) culture systems based on multicellular aggregates, commonly known as tumor spheroids, have been developed. These self-assembled models more closely mimic key characteristics of solid tumors, including oxygen and nutrient gradients, cell-cell and cell-extracellular matrix interactions, extracellular matrix deposition, and intratumoral cellular heterogeneity. Spheroids allow observation of physiologically relevant phenomena such as central hypoxia, peripheral necrosis, and differential responses between distinct cell subpopulations, providing a more realistic representation of tumor growth and cohesion dynamics. Consequently, 3D models have proven more predictive than 2D systems for studying drug response, cell migration and invasion, and paracrine communication within the tumor microenvironment [61].

In this context, although 2D cell culture models remain useful for preliminary assessments of cytotoxicity and selectivity, this study employed three-dimensional prostate cancer spheroid models to further evaluate the biological activity of selected ionic salts under more physiologically relevant conditions. Based on the results obtained from 2D viability assays, which demonstrated high biocompatibility in PNT-2 cells and selective cytotoxicity toward tumor cells C10MImCl, C16MImCl, and C16BnImCl were selected for evaluation in DU145 spheroids (**Figure 32**). When tested at 1 µg/mL, all three compounds induced visible morphological alterations after 72 h of treatment, including loss of spheroid compactness and the appearance of radial protrusions (“sprouting”). Such features are commonly associated with cytoskeletal stress, weakened cell–cell junctions, and disruption of spheroid architecture, and have been reported as characteristic responses to cytotoxic or membrane-active agents. Among the tested salts, C16BnImCl induced the most

pronounced structural disruption, in agreement with its strong antiproliferative activity previously observed in 2D cultures (**Figure 32A**). Quantitative assessment using the Alamar Blue assay confirmed a significant reduction in metabolic activity for all three formulations (**Figure 32B**), despite the intrinsic resistance of spheroid models to drug treatment due to limited compound penetration, extracellular matrix barriers, and activation of microenvironment-dependent survival pathways. The marked activity of C_{16}BnImCl in the 3D setting underscores its potent biological effect; however, this pronounced cytotoxicity also highlights potential limitations for its use in delivery-oriented applications, where excessive membrane disruption and lack of control over biological responses may compromise safety.

In contrast, the ability of C_{10}MImCl and C_{16}MImCl to induce measurable structural and metabolic effects in spheroids, while exhibiting a more moderate and controlled activity profile, supports their suitability as functional components in nanoparticle-based siRNA delivery systems.

Taken together, these results demonstrate that while all selected ionic salts retain biological activity in a 3D tumor context, their profiles differ substantially in terms of intensity and controllability. The strong cytotoxic behavior of C_{16}BnImCl confirms its efficacy as a free compound, whereas the more balanced activity of C_{10}MImCl and C_{16}MImCl aligns with the requirements for PLGA nanoparticle functionalization, where biocompatibility, tunability, and controlled intracellular delivery are essential for effective gene silencing.

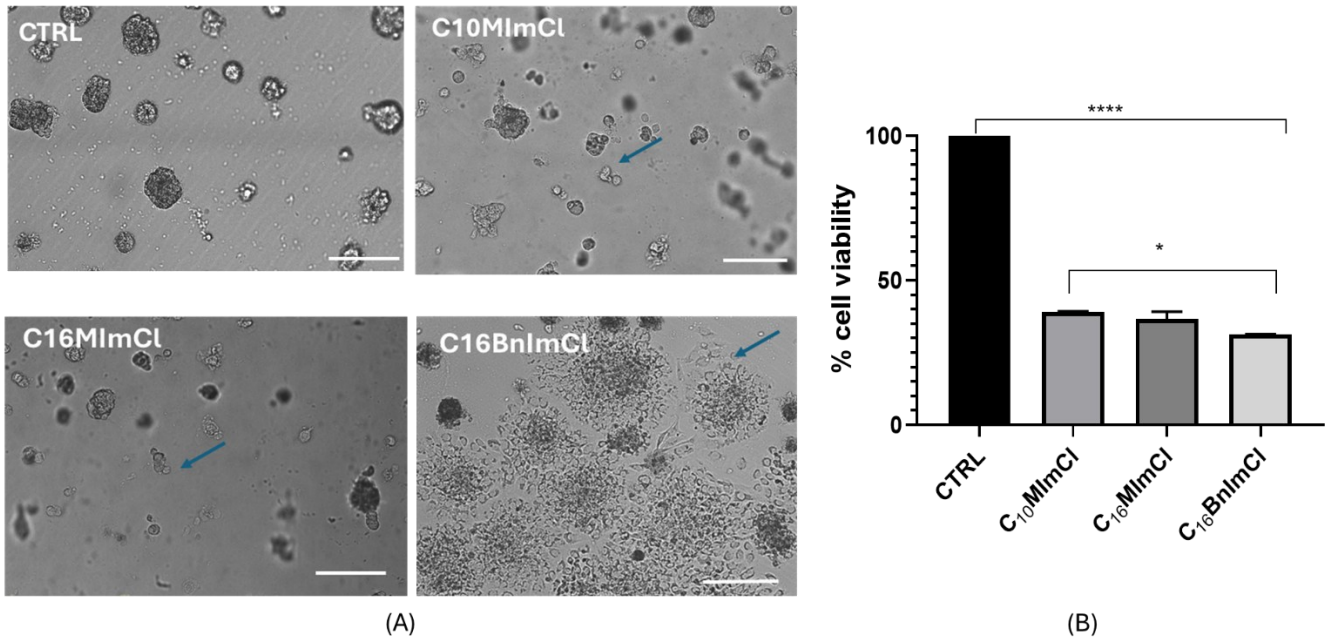

Figure 32. ILs-mediated effect on DU145 cancer spheroids. A) Representative bright-field images showing morphological alterations in DU145 prostate cancer spheroids after 72 h of treatment with imidazolium salts (C_{10}MImCl, C_{16}MImCl, and C_{16}BnImCl; 1 µg/mL). Compared with untreated controls, all treatments induced spheroid destabilization characterized by sprouting, loss of compact architecture, and reduced structural integrity. Scale bar = 250 µm. **B)** Cell

viability of DU145 spheroids after 72 h of exposure to the same compounds, quantified using the Alamar Blue assay. Data are presented as mean ± SD. Untreated 3D spheroids served as controls. Statistical significance: (*) $0.05 < p \leq 0.10$; (**) $0.01 < p \leq 0.05$(***); $0.001 < p \leq 0.01$; (****) $p \leq 0.001$.

4.14 Effect of PLGA-ILs NPs on spheroids formation in DU145-HUVEC co-cultures

This work was conducted at the School of Applied Sciences and Centre for Regenerative Medicine and Devices, University of Brighton, under the supervision of Professor Matteo Santin.

Three-dimensional co-culture models represent a critical tool for investigating tumor behavior under conditions that more closely resemble the *in vivo* microenvironment. In particular, heterotypic spheroids composed of prostate cancer cells and endothelial cells allow the study of tumor–vascular interactions, multicellular organization, and paracrine signaling, all of which play a central role in tumor progression and therapeutic response. Compared to conventional two-dimensional cultures, these systems better recapitulate the spatial architecture, cell–cell communication, and functional heterogeneity characteristic of solid tumors. In this context, the present study aimed to evaluate the impact of PLGA nanoparticles functionalized with imidazolium-based ionic liquids on spheroid formation and three-dimensional organization in DU145–HUVEC co-cultures. The Phenodrive biomimetic platform was employed to generate uniform and reproducible spheroids under mechanically and spatially relevant conditions, enabling real-time assessment of aggregation dynamics and multicellular architecture, as described in the publications by Santin et al.[105]. This approach provided a suitable framework to investigate whether PLGA–ILs nanoparticles modulate spheroid formation through functional interference with cell–cell interactions rather than through direct cytotoxicity. Based on previous results demonstrating favorable biocompatibility, controlled cellular uptake, and effective siRNA delivery, PLGA–C10 and PLGA–C16 nanoparticles were selected for this analysis. These systems differ in alkyl chain length, a parameter known to influence surface hydrophobicity, membrane adsorption, and internalization kinetics, thereby potentially affecting cell–cell interactions and microenvironmental organization in three-dimensional models [106]. DU145–HUVEC co-cultures were treated with PLGA–ILs nanoparticles at concentrations of 150 and 500 ng/mL for 24 h. (**Figure 33).** While untreated co-cultures formed compact and well-organized spheroids, treatment with PLGA–C10 and PLGA–C16 nanoparticles resulted in a clear reduction in the formation of three-dimensional aggregates. This effect was concentration-dependent and more pronounced for PLGA–C10 nanoparticles. The observed phenotype was characterized by

reduced spheroid cohesion and altered aggregate morphology, suggesting interference with mechanisms governing cell aggregation, adhesion, and structural organization—processes that are fundamental for spheroid integrity and tumor microenvironment modeling[11].Importantly, cytotoxicity analysis using LDH release confirmed that these alterations were not associated with cell death, indicating that the reduction in spheroid formation arises from functional modulation of cell–cell interactions rather than from nonspecific toxicity. Similar effects have been reported in three-dimensional models exposed to nanoparticles or surface-functionalized materials that influence aggregation and paracrine communication without compromising cell viability (**Figure 33A**). These findings are particularly relevant when interpreted alongside the effective silencing of GOLPH3 achieved with PLGA–ILs nanoparticles. GOLPH3 plays a key role in Golgi function, vesicular trafficking, and cytoskeletal organization, and its downregulation has been associated with impaired cell polarity, altered adhesion dynamics, and reduced migratory behavior. In a heterotypic DU145–HUVEC system, modulation of tumor cell signaling through GOLPH3 silencing is likely to affect not only cancer cell behavior but also tumor–endothelial interactions, thereby impacting multicellular assembly and spheroid organization. (**Figure 33B**).

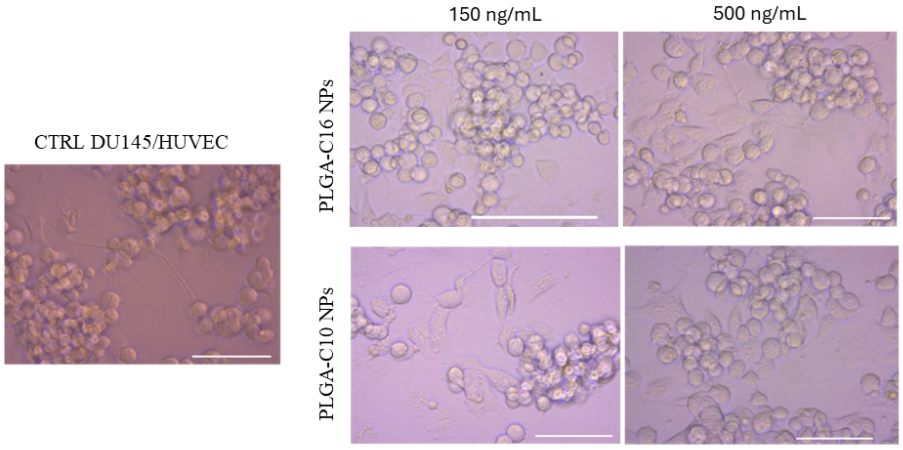

(A)

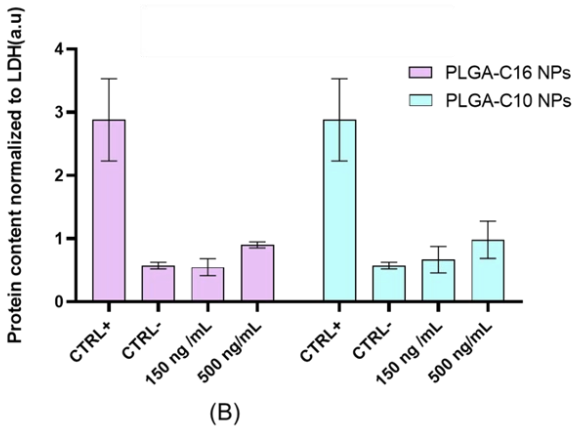

(B)

Figure 33. Impact of PLGA-ILs treatment on spheroid formation in DU145-HUVEC cocultures. A) Bright-field images of DU145-Huvec spheroids treated with PLGA-C16 and PLGA-C10 NPs acquired after 24 hours of exposure to concentrations of 150 and 500 ng/mL (40× objective, scale bar 100 μm). **B)** LDH release analysis, conducted to assess cell membrane integrity, indicated the absence of significant cytotoxicity at the doses tested.

Eosin/hematoxylin staining further confirmed these observations, showing more dispersed cells and less compact aggregates in the treated samples, with a more pronounced effect for PLGA-C10 than for PLGA-C16 NPs (**Figure 34**). These differences can be interpreted in light of the internalization data. PLGA-C10, although showing significant uptake only at 72 hours, was already able to alter spheroid formation at 24 hours, suggesting that surface interactions between particles and the cell membrane are sufficient to modulate cell adhesion and cohesion. In contrast, PLGA-C16 NPs, internalized more rapidly and efficiently, showed a lesser effect on spheroid structure in the first 24 hours, consistent with a predominant role of surface interactions in determining the initial self-assembly of aggregates [107](**Figure 34A,B**).

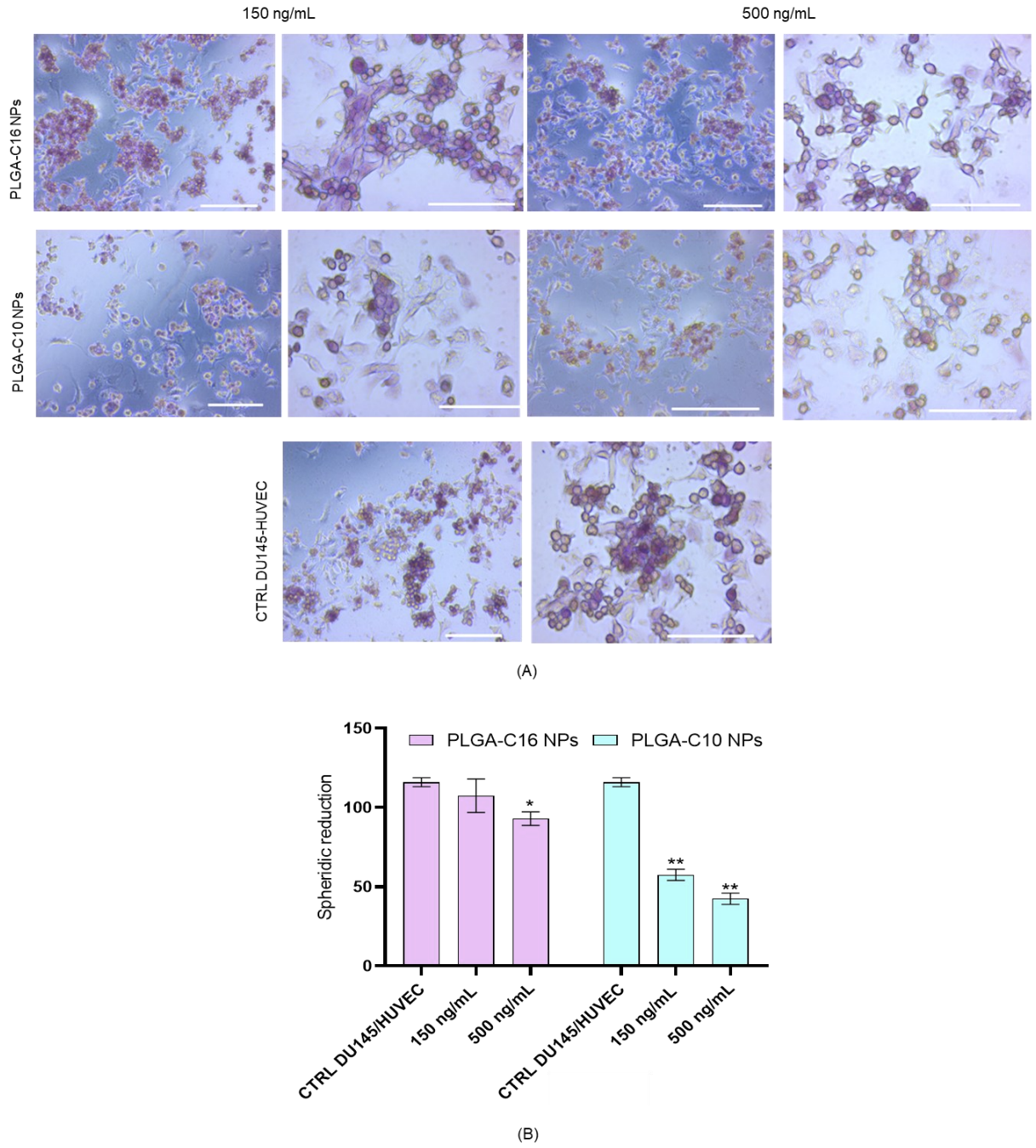

Figure 34. Impact of PLGA-ILs treatment on spheroid formation in DU145/HUVEC co-cultures by Eosin/Hematoxylin staining. A) Characterization by Hematoxylin and Eosin staining highlights a reduction in three-dimensional aggregation capacity proportional to the nanoparticle concentration used after 24 hours. (10x and 40× objective, scale bar 100 µm). A transition from compact spheroids (control) to progressively more dispersed and less organized cellular phenotypes is observed following treatment, particularly with PLGA-C10 NPs at 500 ng/mL. **B)** Quantification of spheroid reduction confirms that the inhibitory effect is significantly more marked for PLGA-C10 nanoparticles than for PLGA-C10 NPs, at the dose of 500 ng/mL. Data represent mean ± SD; significance compared to control is indicated as (*) $p \leq 0.05$ and (**) $p \leq 0.01$.

These results are consistent with evidence reported in the literature that the physicochemical properties of nanoparticles, such as hydrophobicity, surface charge, and size, influence not only internalization but also membrane adsorption and the modulation of paracrine signals, which in turn regulate cohesion and the formation of three-dimensional aggregates [108]. In this context, the biomimetic substrate Phenodrive provides physiologically relevant support for studying self-assembly dynamics by simulating the architecture and mechanics of the tumor microenvironment, as highlighted by Santin et al., allowing for the evaluation of the effects of nanocarriers on structural and functional parameters unobservable in 2D models [105]. In summary, these findings demonstrate that PLGA–ILs nanoparticles are able to modulate the cohesion and three-dimensional organization of DU145–HUVEC co-cultures without inducing direct cytotoxicity. This effect appears to be primarily driven by nanoparticle surface interactions and the consequent modulation of cell–cell and paracrine signaling, rather than by rapid intracellular accumulation. When interpreted in light of the effective GOLPH3 silencing achieved with PLGA–ILs nanoparticles, the observed alterations in spheroid organization likely reflect functional changes in tumor cell signaling that propagate to the endothelial compartment, ultimately impacting multicellular assembly and microenvironmental architecture. These results underscore the value of biomimetic three-dimensional platforms such as Phenodrive for capturing subtle but biologically relevant effects of nanocarriers on the tumor microenvironment. Moreover, they provide a strong rationale for the further development of PLGA–ILs-based systems as carriers for siRNA delivery, with the potential to modulate tumor progression through targeted gene regulation rather than nonspecific cytotoxicity.

5. Conclusions

This thesis demonstrates that rationally engineered polymeric nanoparticles represent a powerful and clinically relevant strategy for siRNA-based gene therapy in prostate cancer. By employing PLGA a biodegradable, biocompatible, and clinically established polymer, as the nanocarrier backbone, and by fine-tuning its surface chemistry through functionalization with imidazolium-based ionic liquids, this work establishes a versatile platform capable of addressing key biological and technological barriers that have historically limited the translation of non-viral gene delivery systems.

A central finding of this study is that PLGA–C16 nanoparticles achieve highly efficient intracellular delivery of siRNA targeting the oncogene GOLPH3 in DU145 prostate cancer cells, resulting in robust gene silencing and pronounced functional effects. Notably, PLGA–C16 nanoparticles matched or outperformed Lipofectamine, a widely used gold-standard transfection reagent, in terms of silencing efficiency and downstream biological outcomes, including inhibition of cell migration and disruption of three-dimensional tumor organization. Importantly, these effects were achieved without the cytotoxicity and nonspecific membrane damage commonly associated with cationic lipid-based formulations, highlighting a major advantage of polymeric nanocarriers for therapeutic applications.

The superior performance of PLGA–C16 nanoparticles can be directly attributed to the rational modulation of surface properties, particularly the presence of a longer alkyl chain that enhances membrane affinity and promotes controlled, predominantly clathrin-mediated internalization at therapeutically relevant concentrations. In contrast, PLGA–C10 nanoparticles, characterized by shorter alkyl chains, exhibited slower uptake kinetics and limited functional silencing, underscoring how subtle differences in surface chemistry translate into substantial differences in intracellular fate and therapeutic efficacy. These findings emphasize that effective gene therapy requires not only cellular internalization, but also optimal intracellular trafficking and timely siRNA release to ensure cytosolic availability.

Beyond two-dimensional models, the translational relevance of PLGA–ILs nanoparticles was further validated using advanced three-dimensional tumor systems, including DU145 spheroids and DU145–HUVEC co-cultures on the Phenodrive biomimetic platform. In these models, PLGA–ILs nanoparticles modulated spheroid formation, cell cohesion, and multicellular organization without inducing direct cytotoxicity, revealing their ability to influence tumor architecture and tumor–endothelial interactions through functional, non-lethal mechanisms. Such effects are particularly significant in prostate cancer, where tumor microenvironment dynamics, angiogenic signaling, and cell–cell communication play critical roles in disease progression and therapeutic resistance.

Targeting GOLPH3 is of specific clinical relevance, as its overexpression in prostate cancer has been associated with increased tumor aggressiveness, enhanced migratory capacity, and poor prognosis. The effective silencing of GOLPH3 achieved with PLGA–C16 nanoparticles translated into meaningful suppression of cancer-associated phenotypes, providing direct evidence that molecular knockdown can be converted into functional therapeutic benefit when delivered through an appropriately designed nanocarrier. This ability to bridge molecular intervention and phenotypic outcome represents a key requirement for the successful clinical translation of gene therapy strategies. Overall, this work positions PLGA–C16 nanoparticles as a robust, tunable, and clinically promising alternative to conventional lipid-based transfection systems for siRNA delivery in prostate cancer. More broadly, the design principles established in this thesis demonstrate how controlled modulation of polymeric nanoparticle surface chemistry can be leveraged to harmonize biocompatibility, uptake mechanism, intracellular release, and functional efficacy. These insights provide a solid foundation for the development of next-generation, non-viral gene therapies targeting GOLPH3 and other oncogenic drivers, supporting the future integration of polymeric nanomedicine platforms into precision oncology and personalized therapeutic strategies.

6. Future Perspectives

The results obtained in this work demonstrate the potential of PLGA-ILs and LGIP NPs nanosystems as an innovative platform for the treatment of prostate cancer. The observed selective activity against tumor cells, the ability to modulate key processes such as proliferation, migration, and oxidative stress, as well as the confirmation of efficacy in more physiologically relevant three-dimensional models, provide a solid scientific basis for the further development of this strategy. For PLGA-ILs, the integrated approach adopted, which includes physicochemical characterization, functional studies, and 3D validation, provides a solid and coherent basis for moving to subsequent research phases. In this context, the natural evolutionary step for the project concerns *in vivo* validation. Preclinical studies in animal models will be essential to systematically evaluate therapeutic efficacy in a complex organism, biodistribution, pharmacokinetics, systemic stability, and tumor accumulation efficiency. These analyses will also provide insights into clearance mechanisms, potential interactions with the immune system, and the presence of potential off-target effects. Another area of investigation concerns the system's medium- and long-term safety profile and biodegradation processes, particularly considering the integration of imidazole-based ionic liquids, whose systemic biological interactions merit extensive characterization under dynamic physiological conditions.

Although the three-dimensional models and co-cultures employed represent a significant advance over traditional two-dimensional systems, they do not fully reproduce the complexity of the in vivo tumor microenvironment, which includes functional vasculature, immune infiltration, stromal components, and dynamic systemic influences. Therefore, future research activities will be directed toward comprehensive preclinical validation, structured toxicology analysis, and optimization of dosing regimens, with the aim of consolidating the platform's translational potential and assessing its applicability in precision therapeutic strategies.

Acknowledgment

This study was funded by National Center for Gene Therapy and Drugs Based on RNA Technology, funded in the framework of the National Recovery and Resilience Plan (NRRP), Mission 4 "Education and Research", Component 2 "From Research to Business", Investment 1.4 "Strengthening research structures for supporting the creation of National Centres, national R&D leaders on some Key Enabling Technologies", funded by the European Union - Next Generation EU, Project CN00000041, CUP: B83C22002860006

7. References

[1] Hanahan D. Hallmarks of Cancer: New Dimensions. Cancer Discov 2022;12:31–46. https://doi.org/10.1158/2159-8290.CD-21-1059.

[2] Sibai M, Cervilla S, Grases D, Musulen E, Lazcano R, Mo CK, et al. The spatial landscape of cancer hallmarks reveals patterns of tumor ecological dynamics and drug sensitivity. Cell Rep 2025;44. https://doi.org/10.1016/j.celrep.2024.115229.

[3] Smith RA, Andrews KS, Brooks D, Fedewa SA, Manassaram-Baptiste D, Saslow D, et al. Cancer screening in the United States, 2019: A review of current American Cancer Society guidelines and current issues in cancer screening. CA Cancer J Clin 2019;69:184–210. https://doi.org/10.3322/caac.21557.

[4] Dakal TC, Dhabhai B, Pant A, Moar K, Chaudhary K, Yadav V, et al. Oncogenes and tumor suppressor genes: functions and roles in cancers. MedComm (Beijing) 2024;5. https://doi.org/10.1002/mco2.582.

[5] Sekhoacha M, Riet K, Motloung P, Gumenku L, Adegoke A, Mashele S. Prostate Cancer Review: Genetics, Diagnosis, Treatment Options, and Alternative Approaches. Molecules 2022;27. https://doi.org/10.3390/molecules27175730.

[6] Kaleem M, Dalhat MH, Azmi L, Asar TO, Ahmad W, Alghanmi M, et al. An Insight into Molecular Targets of Breast Cancer Brain Metastasis. Int J Mol Sci 2022;23. https://doi.org/10.3390/ijms231911687.

[7] Lovly CM, Salama AKS, Salgia R. Tumor Heterogeneity and Therapeutic Resistance. American Society of Clinical Oncology Educational Book 2016:e585–93. https://doi.org/10.1200/edbk_158808.

[8] Fu YC, Liang SB, Luo M, Wang XP. Intratumoral heterogeneity and drug resistance in cancer. Cancer Cell International 2025;25. https://doi.org/10.1186/s12935-025-03734-w.

[9] Kara G, Calin GA, Ozpolat B. RNAi-based therapeutics and tumor targeted delivery in cancer. Adv Drug Deliv Rev 2022;182. https://doi.org/10.1016/j.addr.2022.114113.

[10] Kuna RS, Field SJ. GOLPH3: A Golgi phosphatidylinositol(4)phosphate effector that directs vesicle trafficking and drives cancer. J Lipid Res 2019;60:269–75. https://doi.org/10.1194/jlr.R088328.

[11] Sechi S, Frappaolo A, Karimpour-Ghahnavieh A, Piergentili R, Giansanti MG. Oncogenic roles of GOLPH3 in the physiopathology of cancer. Int J Mol Sci 2020;21. https://doi.org/10.3390/ijms21030933.

[12] Bajaj R, Warner AN, Fradette JF, Gibbons DL. Dance of The Golgi: Understanding Golgi Dynamics in Cancer Metastasis. Cells 2022;11. https://doi.org/10.3390/cells11091484.

[13] Wang J, Tang W, Yang M, Yin Y, Li H, Hu F, et al. Inflammatory tumor microenvironment responsive neutrophil exosomes-based drug delivery system for targeted glioma therapy. Biomaterials 2021;273. https://doi.org/10.1016/j.biomaterials.2021.120784.

[14] Siegel DJ, Anderson GI, Paul LM, Seibert PJ, Hillesheim PC, Sheng Y, et al. Design Principles of Lipid-like Ionic Liquids for Gene Delivery. ACS Appl Bio Mater 2021;4:4737–43. https://doi.org/10.1021/acsabm.1c00252.

[15] Glick BS, Nakano A. Membrane traffic within the Golgi apparatus. Annu Rev Cell Dev Biol 2009;25:113–32. https://doi.org/10.1146/annurev.cellbio.24.110707.175421.

[16] Generation of target cells. 2001.

[17] Scott KL, Kabbarah O, Liang MC, Ivanova E, Anagnostou V, Wu J, et al. G0LPH3 modulates mTOR signalling and rapamydn sensitivity in cancer. Nature 2009;459:1085–90. https://doi.org/10.1038/nature08109.

[18] Dippold HC, Ng MM, Farber-Katz SE, Lee SK, Kerr ML, Peterman MC, et al. GOLPH3 Bridges Phosphatidylinositol-4- Phosphate and Actomyosin to Stretch and Shape the Golgi to Promote Budding. Cell 2009;139:337–51. https://doi.org/10.1016/j.cell.2009.07.052.

[19] Wu CC, Taylor RS, Lane DR, Ladinsky MS, Weisz JA, Howell KE. GMx33: A Novel Family of trans -Golgi Proteins Identified by Proteomics . Traffic 2000;1:963–75. https://doi.org/10.1111/j.1600-0854.2000.11206.x.
[20] Farber-Katz SE, Dippold HC, Buschman MD, Peterman MC, Xing M, Noakes CJ, et al. DNA damage triggers golgi dispersal via DNA-PK and GOLPH3. Cell 2014;156:413–27. https://doi.org/10.1016/j.cell.2013.12.023.
[21] Eckert ESP, Reckmann I, Hellwig A, Röhling S, El-Battari A, Wieland FT, et al. Golgi phosphoprotein 3 triggers signal-mediated incorporation of glycosyltransferases into coatomer-coated (COPI) vesicles. Journal of Biological Chemistry 2014;289:31319–29. https://doi.org/10.1074/jbc.M114.608182.
[22] Maccioni HJF. Glycosylation of glycolipids in the Golgi complex. J Neurochem 2007;103 Suppl 1:81–90. https://doi.org/10.1111/j.1471-4159.2007.04717.x.
[23] Rizzo R, Russo D, Kurokawa K, Sahu P, Lombardi B, Supino D, et al. Golgi maturation-dependent glycoenzyme recycling controls glycosphingolipid biosynthesis and cell growth via GOLPH3. EMBO J 2021;40. https://doi.org/10.15252/embj.2020107238.
[24] Szwed A, Kim E, Jacinto E. REGULATION AND METABOLIC FUNCTIONS OF mTORC1 AND mTORC2. Physiol Rev 2021;101:1371–426. https://doi.org/10.1152/physrev.00026.2020.
[25] Zafar A, Khatoon S, Khan MJ, Abu J, Naeem A. Advancements and limitations in traditional anti-cancer therapies: a comprehensive review of surgery, chemotherapy, radiation therapy, and hormonal therapy. Discover Oncology 2025;16. https://doi.org/10.1007/s12672-025-02198-8.
[26] Seror O. Ablative therapies: Advantages and disadvantages of radiofrequency, cryotherapy, microwave and electroporation methods, or how to choose the right method for an individual patient? Diagn Interv Imaging 2015;96:617–24. https://doi.org/10.1016/j.diii.2015.04.007.
[27] Davidson BL, McCray PB. Current prospects for RNA interference-based therapies. Nat Rev Genet 2011;12:329–40. https://doi.org/10.1038/nrg2968.
[28] Gavrilov K, Saltzman WM. Therapeutic siRna: Principles, challenges, and strategies. vol. 85. 2012.
[29] Kumar R, Kulkarni A, Nabulsi J, Nagesha DK, Cormack R, Makrigiorgos MG, et al. Facile synthesis of PEGylated PLGA nanoparticles encapsulating doxorubicin and its in vitro evaluation as potent drug delivery vehicle. Drug Deliv Transl Res 2013;3:299–308. https://doi.org/10.1007/s13346-012-0124-9.
[30] Kanasty R, Dorkin JR, Vegas A, Anderson D. Delivery materials for siRNA therapeutics. Nat Mater 2013;12:967–77. https://doi.org/10.1038/nmat3765.
[31] Guo H, Zhou C, Zheng M, Zhang J, Wu H, He Q, et al. Insights into the role of derailed endocytic trafficking pathway in cancer: From the perspective of cancer hallmarks. Pharmacol Res 2024;201. https://doi.org/10.1016/j.phrs.2024.107084.
[32] Abdellatef E, Kamal NM, Tsujimoto H. Tuning beforehand: A foresight on rna interference (rnai) and in vitro-derived dsrnas to enhance crop resilience to biotic and abiotic stresses. Int J Mol Sci 2021;22. https://doi.org/10.3390/ijms22147687.
[33] Dana H, Mahmoodi Chalbatani G, Mahmoodzadeh H, Karimloo R, Rezaiean O, Moradzadeh A, et al. Molecular Mechanisms and Biological Functions of siRNA. vol. 13. 2017.
[34] Whitehead KA, Langer R, Anderson DG. Knocking down barriers: Advances in siRNA delivery. Nat Rev Drug Discov 2009;8:129–38. https://doi.org/10.1038/nrd2742.
[35] Rehman U, Parveen N, Sheikh A, Abourehab MAS, Sahebkar A, Kesharwani P. Polymeric nanoparticles-siRNA as an emerging nano-polyplexes against ovarian cancer. Colloids Surf B Biointerfaces 2022;218. https://doi.org/10.1016/j.colsurfb.2022.112766.
[36] Guo X, Huang L. Recent advances in nonviral vectors for gene delivery. Acc Chem Res 2012;45:971–9. https://doi.org/10.1021/ar200151m.

[37] Blanco E, Shen H, Ferrari M. Principles of nanoparticle design for overcoming biological barriers to drug delivery. Nat Biotechnol 2015;33:941–51. https://doi.org/10.1038/nbt.3330.
[38] Wahajuddin, Arora S. Superparamagnetic iron oxide nanoparticles: Magnetic nanoplatforms as drug carriers. Int J Nanomedicine 2012;7:3445–71. https://doi.org/10.2147/IJN.S30320.
[39] Sabit H, Abdel-Hakeem M, Shoala T, Abdel-Ghany S, Abdel-Latif MM, Almulhim J, et al. Nanocarriers: A Reliable Tool for the Delivery of Anticancer Drugs. Pharmaceutics 2022;14. https://doi.org/10.3390/pharmaceutics14081566.
[40] Tarn D, Ashley CE, Xue M, Carnes EC, Zink JI, Brinker CJ. Mesoporous silica nanoparticle nanocarriers: Biofunctionality and biocompatibility. Acc Chem Res 2013;46:792–801. https://doi.org/10.1021/ar3000986.
[41] Dymek M, Sikora E. Liposomes as biocompatible and smart delivery systems – the current state. Adv Colloid Interface Sci 2022;309. https://doi.org/10.1016/j.cis.2022.102757.
[42] Wu SY, McMillan NAJ. Lipidic systems for in vivo siRNA delivery. AAPS Journal 2009;11:639–52. https://doi.org/10.1208/s12248-009-9140-1.
[43] Zielinska A, Carreiró F, Oliveira AM, Neves A, Pires B, Nagasamy Venkatesh D, et al. Polymeric Nanoparticles: Production, Characterization, Toxicology and Ecotoxicology. Molecules 2020;25. https://doi.org/10.3390/molecules25163731.
[44] Elsabahy M, Wooley KL. Design of polymeric nanoparticles for biomedical delivery applications. Chem Soc Rev 2012;41:2545–61. https://doi.org/10.1039/c2cs15327k.
[45] Elmowafy M, Shalaby K, Elkomy MH, Alsaidan OA, Gomaa HAM, Abdelgawad MA, et al. Polymeric Nanoparticles for Delivery of Natural Bioactive Agents: Recent Advances and Challenges. Polymers (Basel) 2023;15. https://doi.org/10.3390/polym15051123.
[46] Nguyen L, Nguyen TT, Kim JY, Jeong JH. Advanced siRNA delivery in combating hepatitis B virus: mechanistic insights and recent updates. Journal of Nanobiotechnology 2024;22. https://doi.org/10.1186/s12951-024-03004-3.
[47] Brooks EA, Galarza S, Gencoglu MF, Chase Cornelison R, Munson JM, Peyton SR. Applicability of drug response metrics for cancer studies using biomaterials. Philosophical Transactions of the Royal Society B: Biological Sciences 2019;374. https://doi.org/10.1098/rstb.2018.0226.
[48] Zhang Y, Chen X, Lan J, You J, Chen L. Synthesis and biological applications of imidazolium-based polymerized ionic liquid as a gene delivery vector. Chem Biol Drug Des 2009;74:282–8. https://doi.org/10.1111/j.1747-0285.2009.00858.x.
[49] Curreri AM, Mitragotri S, Tanner EEL. Recent Advances in Ionic Liquids in Biomedicine. Advanced Science 2021;8. https://doi.org/10.1002/advs.202004819.
[50] Galluzzi M, Marfori L, Asperti S, De Vita A, Giannangeli M, Caselli A, et al. Interaction of imidazolium-based ionic liquids with supported phospholipid bilayers as model biomembranes. Physical Chemistry Chemical Physics 2022;1. https://doi.org/10.1039/d2cp02866b.
[51] Zhao D, Liao Y, Zhang ZD. Toxicity of ionic liquids. Clean (Weinh) 2007;35:42–8. https://doi.org/10.1002/clen.200600015.
[52] Khare P, Edgecomb SX, Hamadani CM, Conway JF, Tanner EEL, S Manickam D. Ionic liquid-coated lipid nanoparticles increase siRNA uptake into CNS targets. Nanoscale Adv 2023. https://doi.org/10.1039/d3na00699a.
[53] Egorova KS, Posvyatenko A V., Larin SS, Ananikov VP. Ionic liquids: Prospects for nucleic acid handling and delivery. Nucleic Acids Res 2021;49:1201–34. https://doi.org/10.1093/nar/gkaa1280.
[54] Zhuo Y, Cheng HL, Zhao YG, Cui HR. Ionic Liquids in Pharmaceutical and Biomedical Applications: A Review. Pharmaceutics 2024;16. https://doi.org/10.3390/pharmaceutics16010151.
[55] Zhao C, Zhou B. Polyethyleneimine-Based Drug Delivery Systems for Cancer Theranostics. J Funct Biomater 2023;14. https://doi.org/10.3390/jfb14010012.

[56] Vader P, Van Der Aa LJ, Engbersen JFJ, Storm G, Schiffelers RM. Physicochemical and biological evaluation of siRNA polyplexes based on PEGylated poly(amido amine)s. Pharm Res 2012;29:352–61. https://doi.org/10.1007/s11095-011-0545-z.
[57] Mainini F, Eccles MR. Lipid and polymer-based nanoparticle siRNA delivery systems for cancer therapy. Molecules 2020;25. https://doi.org/10.3390/molecules25112692.
[58] Akinc A, Thomas M, Klibanov AM, Langer R. Exploring polyethylenimine-mediated DNA transfection and the proton sponge hypothesis. Journal of Gene Medicine 2005;7:657–63. https://doi.org/10.1002/jgm.696.
[59] Kim IY, Kwak M, Kim J, Lee TG, Heo MB. Comparative Study on Nanotoxicity in Human Primary and Cancer Cells. Nanomaterials 2022;12. https://doi.org/10.3390/nano12060993.
[60] Ismail A, Chou SF. Polyethylenimine Carriers for Drug and Gene Delivery. Polymers (Basel) 2025;17. https://doi.org/10.3390/polym17152150.
[61] Tosca EM, Ronchi D, Facciolo D, Magni P. Replacement, Reduction, and Refinement of Animal Experiments in Anticancer Drug Development: The Contribution of 3D In Vitro Cancer Models in the Drug Efficacy Assessment. Biomedicines 2023;11. https://doi.org/10.3390/biomedicines11041058.
[62] Le DT, Tong BT, Nguyen TKT, Cao TN, Nguyen HQ, Tran MC, et al. Polarization-insensitive dual-band terahertz metamaterial absorber based on asymmetric arrangement of two rectangular-shaped resonators. Optik (Stuttg) 2021;245. https://doi.org/10.1016/j.ijleo.2021.167669.
[63] Thomas E, Thomas D, Bhuvaneswari S, Vijayalakshmi KP, George BK. 1-Hexadecyl-3-methylimidazolium chloride: Structure, thermal stability and decomposition mechanism. J Mol Liq 2018;249:404–11. https://doi.org/10.1016/j.molliq.2017.11.029.
[64] Li Z, Guan P, Hu X, Ding S, Tian Y, Xu Y, et al. Preparation of molecularly imprinted mesoporous materials for highly enhancing adsorption performance of Cytochrome C. Polymers (Basel) 2018;10. https://doi.org/10.3390/polym10030298.
[65] Toppino A, Bova ME, Crich SG, Alberti D, Diana E, Barge A, et al. A carborane-derivative "click" reaction under heterogeneous conditions for the synthesis of a promising lipophilic MRI/GdBNCT agent. Chemistry - A European Journal 2013;19:721–8. https://doi.org/10.1002/chem.201201634.
[66] Boyd DA, Lin WH, Hsu CC, Teague ML, Chen CC, Lo YY, et al. Single-step deposition of high-mobility graphene at reduced temperatures. Nat Commun 2015;6. https://doi.org/10.1038/ncomms7620.
[67] Rhimi B, Liu Z, Liu Z, Zhou M, Shi W, Jiang Z. Emerging trends in metal organic framework based materials for enhanced photocatalytic CO2 reduction. Coord Chem Rev 2025;537. https://doi.org/10.1016/j.ccr.2025.216706.
[68] Colonna M, Berti C, Binassi E, Fiorini M, Sullalti S, Acquasanta F, et al. Imidazolium poly(butylene terephthalate) ionomers with long-term antimicrobial activity. Polymer (Guildf) 2012;53:1823–30. https://doi.org/10.1016/j.polymer.2012.03.003.
[69] Casal-Dujat L, Rodrigues M, Yagüe A, Calpena AC, Amabilino DB, Gonzaílez-Linares J, et al. Gemini imidazolium amphiphiles for the synthesis, stabilization, and drug delivery from gold nanoparticles. Langmuir 2012;28:2368–81. https://doi.org/10.1021/la203601n.
[70] Barres AR, Wimmer MR, Mecozzi S. Multicompartment Theranostic Nanoemulsions Stabilized by a Triphilic Semifluorinated Block Copolymer. Mol Pharm 2017;14:3916–26. https://doi.org/10.1021/acs.molpharmaceut.7b00624.
[71] Wang H, Huang J, Uddin MA, Liu B, Chen P, Shi S, et al. Cyano-Substituted Head-to-Head Polythiophenes: Enabling High-Performance n-Type Organic Thin-Film Transistors. ACS Appl Mater Interfaces 2019;11:10089–98. https://doi.org/10.1021/acsami.8b22457.
[72] Cun D, Jensen DK, Maltesen MJ, Bunker M, Whiteside P, Scurr D, et al. High loading efficiency and sustained release of siRNA encapsulated in PLGA nanoparticles: Quality by

design optimization and characterization. European Journal of Pharmaceutics and Biopharmaceutics 2011;77:26–35. https://doi.org/10.1016/j.ejpb.2010.11.008.
[73] Correia DM, Fernandes LC, Fernandes MM, Hermenegildo B, Meira RM, Ribeiro C, et al. Ionic liquid-based materials for biomedical applications. Nanomaterials 2021;11. https://doi.org/10.3390/nano11092401.
[74] Siegel DJ, Anderson GI, Paul LM, Seibert PJ, Hillesheim PC, Sheng Y, et al. Design Principles of Lipid-like Ionic Liquids for Gene Delivery. ACS Appl Bio Mater 2021;4:4737–43. https://doi.org/10.1021/acsabm.1c00252.
[75] Fernandes MM, Carvalho EO, Correia DM, Esperança JMSS, Padrão J, Ivanova K, et al. Ionic Liquids as Biocompatible Antibacterial Agents: A Case Study on Structure-Related Bioactivity on Escherichia coli. ACS Appl Bio Mater 2022;5:5181–9. https://doi.org/10.1021/acsabm.2c00615.
[76] Boussif O, Lezoualc'ht F, Zanta MA, Mergnyt D, Schermant D, Demeneixt B, et al. A versatile vector for gene and oligonucleotide transfer into cells in culture and in vivo: Polyethylenimine. vol. 92. 1995.
[77] Welton T. Room-Temperature Ionic Liquids. Solvents for Synthesis and Catalysis. Chem Rev 1999;99:2071–83. https://doi.org/10.1021/cr980032t.
[78] Kumar S, Scheidt HA, Kaur N, Kang TS, Gahlay GK, Huster D, et al. Effect of the Alkyl Chain Length of Amphiphilic Ionic Liquids on the Structure and Dynamics of Model Lipid Membranes. Langmuir 2019;35:12215–23. https://doi.org/10.1021/acs.langmuir.9b02128.
[79] Gruber S, Nickel A. Toxic or not toxic? The specifications of the standard ISO 10993-5 are not explicit enough to yield comparable results in the cytotoxicity assessment of an identical medical device. Front Med Technol 2023;5. https://doi.org/10.3389/fmedt.2023.1195529.
[80] Mlostoń G, Kowalczyk M, Celeda M, Gach-Janczak K, Janecka A, Jasiński M. Synthesis and Cytotoxic Activity of Lepidilines A–D: Comparison with Some 4,5-Diphenyl Analogues and Related Imidazole-2-thiones. J Nat Prod 2021;84:3071–9. https://doi.org/10.1021/acs.jnatprod.1c00797.
[81] Hagel JM, Facchini PJ. Benzylisoquinoline alkaloid metabolism: A century of discovery and a brave new world. Plant Cell Physiol 2013;54:647–72. https://doi.org/10.1093/pcp/pct020.
[82] Alsaab HO, Alharbi FD, Alhibs AS, Alanazi NB, Alshehri BY, Saleh MA, et al. PLGA-Based Nanomedicine: History of Advancement and Development in Clinical Applications of Multiple Diseases. Pharmaceutics 2022;14. https://doi.org/10.3390/pharmaceutics14122728.
[83] Danhier F, Ansorena E, Silva JM, Coco R, Le Breton A, Préat V. PLGA-based nanoparticles: An overview of biomedical applications. Journal of Controlled Release 2012;161:505–22. https://doi.org/10.1016/j.jconrel.2012.01.043.
[84] Chiu HI, Samad NA, Fang L, Lim V. Cytotoxicity of targeted PLGA nanoparticles: a systematic review. RSC Adv 2021;11:9433–49. https://doi.org/10.1039/d1ra00074h.
[85] Berton P, Shamshina JL. Ionic Liquids as Tools to Incorporate Pharmaceutical Ingredients into Biopolymer-Based Drug Delivery Systems. Pharmaceuticals 2023;16. https://doi.org/10.3390/ph16020272.
[86] Arifka M, Wilar G, Elamin KM, Wathoni N. Polymeric Hydrogels as Mesenchymal Stem Cell Secretome Delivery System in Biomedical Applications. Polymers (Basel) 2022;14. https://doi.org/10.3390/polym14061218.
[87] Dong B, Li N, Zheng L, Yu L, Inoue T. Surface adsorption and micelle formation of surface active ionic liquids in aqueous solution. Langmuir 2007;23:4178–82. https://doi.org/10.1021/la0633029.
[88] Zerrillo L, Gigliobianco MR, D'atri D, Garcia JP, Baldazzi F, Ridwan Y, et al. PLGA Nanoparticles Grafted with Hyaluronic Acid to Improve Site-Specificity and Drug Dose Delivery in Osteoarthritis Nanotherapy. Nanomaterials 2022;12. https://doi.org/10.3390/nano12132248.

[89] Risnayanti C, Jang YS, Lee J, Ahn HJ. PLGA nanoparticles co-delivering MDR1 and BCL2 siRNA for overcoming resistance of paclitaxel and cisplatin in recurrent or advanced ovarian cancer. Sci Rep 2018;8. https://doi.org/10.1038/s41598-018-25930-7.
[90] Cai X, Dou R, Guo C, Tang J, Li X, Chen J, et al. Cationic Polymers as Transfection Reagents for Nucleic Acid Delivery. Pharmaceutics 2023;15. https://doi.org/10.3390/pharmaceutics15051502.
[91] Patil Y, Panyam J. Polymeric nanoparticles for siRNA delivery and gene silencing. Int J Pharm 2009;367:195–203. https://doi.org/10.1016/j.ijpharm.2008.09.039.
[92] Fröhlich E. The role of surface charge in cellular uptake and cytotoxicity of medical nanoparticles. Int J Nanomedicine 2012;7:5577–91. https://doi.org/10.2147/IJN.S36111.
[93] Sanità G, Carrese B, Lamberti A. Nanoparticle Surface Functionalization: How to Improve Biocompatibility and Cellular Internalization. Front Mol Biosci 2020;7. https://doi.org/10.3389/fmolb.2020.587012.
[94] Rejman J, Oberle V, Zuhorn IS, Hoekstra D. Size-dependent internalization of particles via the pathways of clathrin-and caveolae-mediated endocytosis. vol. 377. 2004.
[95] Verma A, Stellacci F. Effect of surface properties on nanoparticle-cell interactions. Small 2010;6:12–21. https://doi.org/10.1002/smll.200901158.
[96] Sahay G, Alakhova DY, Kabanov A V. Endocytosis of nanomedicines. Journal of Controlled Release 2010;145:182–95. https://doi.org/10.1016/j.jconrel.2010.01.036.
[97] Kerr MC, Teasdale RD. Defining macropinocytosis. Traffic 2009;10:364–71. https://doi.org/10.1111/j.1600-0854.2009.00878.x.
[98] Boussif O, Lezoualc'ht F, Zanta MA, Mergnyt D, Schermant D, Demeneixt B, et al. A versatile vector for gene and oligonucleotide transfer into cells in culture and in vivo: Polyethylenimine. vol. 92. 1995.
[99] Farra R, Musiani F, Perrone F, Čemažar M, Kamenšek U, Tonon F, et al. Polymer-mediated delivery of siRNAs to hepatocellular carcinoma: Variables affecting specificity and effectiveness. Molecules 2018;23. https://doi.org/10.3390/molecules23040777.
[100] Hasan W, Chu K, Gullapalli A, Dunn SS, Enlow EM, Luft JC, et al. Delivery of multiple siRNAs using lipid-coated PLGA nanoparticles for treatment of prostate cancer. Nano Lett 2012;12:287–92. https://doi.org/10.1021/nl2035354.
[101] Chen X, Mangala LS, Rodriguez-Aguayo C, Kong X, Lopez-Berestein G, Sood AK. RNA interference-based therapy and its delivery systems. Cancer and Metastasis Reviews 2018;37:107–24. https://doi.org/10.1007/s10555-017-9717-6.
[102] Ko SH, Hur KY, Rhee SY, Kim NH, Moon MK, Park SO, et al. Antihyperglycemic agent therapy for adult patients with type 2 diabetes mellitus 2017: a position statement of the Korean Diabetes Association. Korean J Intern Med 2017;32:947–58. https://doi.org/10.3904/kjim.2017.298.
[103] Song JW, Zhu J, Wu XX, Tu T, Huang JQ, Chen GZ, et al. GOLPH3/CKAP4 promotes metastasis and tumorigenicity by enhancing the secretion of exosomal WNT3A in non-small-cell lung cancer. Cell Death Dis 2021;12. https://doi.org/10.1038/s41419-021-04265-8.
[104] Barbosa MAG, Xavier CPR, Pereira RF, Petrikaitė V, Vasconcelos MH. 3D Cell Culture Models as Recapitulators of the Tumor Microenvironment for the Screening of Anti-Cancer Drugs. Cancers (Basel) 2022;14. https://doi.org/10.3390/cancers14010190.
[105] Perugini V, Santin M. A Substrate-Mimicking Basement Membrane Drives the Organization of Human Mesenchymal Stromal Cells and Endothelial Cells Into Perivascular Niche-Like Structures. Front Cell Dev Biol 2021;9. https://doi.org/10.3389/fcell.2021.701842.
[106] Zhu M, Nie G, Meng H, Xia T, Nel A, Zhao Y. Physicochemical properties determine nanomaterial cellular uptake, transport, and fate. Acc Chem Res 2013;46:622–31. https://doi.org/10.1021/ar300031y.
[107] Trofimov M, Bulatov I, Donskaia I, Efremov A, Litau E, Lavrinenko V, et al. Three-Dimensional Tumor Spheroids of Pancreatic and Colorectal Cancer Cell Lines for High-

Throughput Screening of Drug Candidates. ACS Omega 2025. https://doi.org/10.1021/acsomega.5c03607.
[108] Sabourian P, Yazdani G, Ashraf SS, Frounchi M, Mashayekhan S, Kiani S, et al. Effect of physico-chemical properties of nanoparticles on their intracellular uptake. Int J Mol Sci 2020;21:1–20. https://doi.org/10.3390/ijms21218019.